SHAPE-ENGINEERING SUBSTRATE-BASED PLASMONIC NANOMATERIALS

A Dissertation
Submitted to
the Temple University Graduate Board

In Partial Fulfillment
of the Requirements for the Degree
DOCTOR OF PHILOSOPHY

---

by,
Kyle D. Gilroy
July 2015

Examining Committee Members:

Dr. Svetlana Neretina, Advisory Chair, Mechanical Engineering
Dr. Richard Cohen, Mechanical Engineering at Temple University
Dr. Eric Borguet, Chemistry at Temple University
Dr. Won Suh, Bioengineering at Temple University
Dr. Huichun Zhang, External, Civil and Environmental Engineering at Temple University

ABSTRACT

The advancement of next generation technologies is reliant on our ability to engineer matter at the nanoscale. Since the morphological features of nanomaterials dictate their chemical and physical properties, a significant effort has been put forth to develop syntheses aimed at fine tuning their size, shape and composition. This massive effort has resulted in a maturing colloidal chemistry containing an extensive collection of morphologies with compositions nearly spanning the entire transition region of the periodic table. While colloidal nanoparticles have opened the door to promising applications in fields such as cancer theranostics, drug delivery, catalysis and sensing; the synthetic protocols for the placement of nanomaterials on surfaces, a requisite for chip-based devices, are ill-developed.

This dissertation serves to address this limitation by highlighting a series of syntheses related to the design of substrate-based nanoparticles whose size, shape and composition are controllably engineered to a desired endpoint. The experimental methods are based on a template-mediated approach which sees chemical modifications made to prepositioned thermally assembled metal nanostructures which are well bonded to a sapphire substrate. The first series of investigations will highlight synthetic routes utilizing galvanic replacement reactions, where the prepositioned templates are chemically transformed into hollow nanoshells. Detailed studies are provided highlighting discoveries related to (i) hollowing, (ii) defect transfer, (iii) strain induction, (iv) interdiffusion, (v) crystal structure and (vi) the localized surface plasmon resonance (LSPR).

The second series of investigations, based on heterogeneous nucleation, have templates serve as nucleation sites for metal atoms arriving in either the solution- or vapor phase. The solution-phase heterogeneous nucleation of Ag on Au reveals that chemical kinetics (injection rate & precursor concentration) can be used to control the nature of how Ag atoms assemble on the Au template. It was discovered that (i) slow kinetics leads to an anisotropic growth mode (heterodimeric structures), (ii) fast kinetics causes a very uniform deposition (Au-Ag coreshell morphology, or Au@Ag) and (iii) medium kinetics produces structures with an intermediate morphology (truncated octahedron). In the second case, where the nucleation event is carried out at high temperatures, the Ag vapor is sourced from a sublimating foil onto adjacent Au templates. This process drives the composition and morphology from a Au Wulff-shape to a homogeneous Au-Ag nanoprism. By tracking over time the (i) morphological features, (ii) LSPR and (iii) composition; insights into the fundamental atomic scale growth mechanisms are elucidated. Overall, substrate-based template-mediated syntheses have proven to be an effective route for directing growth pathways toward a desired endpoint giving rise to an impressive new group of complex substrate-based nanostructures with asymmetric, core-shell and hollowed morphologies.

While this dissertation is focused heavily on the development of synthetic procedures aimed at generating substrate-based plasmonic nanomaterials, the last chapter will serve to highlight a series of on-going studies aimed at defining these nanomaterials as highly effective heterogeneous catalysts. Several examples are shown including (i) nanoparticle films synthesize via sputter deposition, (ii) mechanically induced nanotexturing of bulk copper foils, (iii) ultra-small AuPd nanoparticles synthesized via pulse laser, (iv) substrate-based AuCu nanoprisms and (v) the Wulff in a Cage Morphology.

To the hardest working people that I know, my Mother and Father, who continue to devote their lives to supporting me, my brothers and the rest of my family and to my Grandfather who made my education possible.

"What I cannot create, I do not understand"

- Feynman

ACKNOWLEDGEMENTS

I am grateful for having selected Temple University's Renewable Energy Laboratory for carrying out my PhD work and acknowledge first and foremost my advisor Svetlana Neretina. The scientific atmosphere maintained in the Neretina Group is ideal for carrying out research at the highest level. I also acknowledge my collaborator Robert Hughes for his insightful discussions and advice.

I would like to thank Mike Rose who introduced me to fundamentals of classical physics early on. It was Rose's classroom where my scientific interests began. As a physics student at The College of New Jersey, the complex nature of matter and energy was described fantastically by Dr. Romulo Ochoa, my undergraduate physics mentor. I am very thankful for your advice, patience and guidance.

I would like to thank my former labmates, Aarthi Sundar and Pouyan Farzinpour, for your kindness and guidance. To my present labmates and collaborators, Spencer Golze, Eric Menumerov, Maryam Hajfathalian, Ali Yaghoubzade and Devika Sil, I wish you all the best of luck in studies, research and life.

I would like also to acknowledge Fred Monson, technical director of the Center for Microanalysis and Imaging (CMIRT) at West Chester University, who introduced me to the transmission electron microscope. I am also grateful for the assistance from Dmitriy Dikin, Temple's CoE NIC Facility Manager. Lastly, I would like to acknowledge especially Dr. Borguet not only for serving on my committee but also for welcoming me into his group meetings and discussions. Opening up a dialogue between disciplines is a great way to do research.

TABLE OF CONTENTS

Page

LIST OF TABLES

LIST OF FIGURES

CHAPTER 1

INTRODUCTION

1.1 Overview and Background

At the onset of the 21st century, the modernization of science and technology is reliant on the ongoing effort to miniaturize material not only to replace the current microscaled technologies but also to exploit the new and exciting properties materials exhibit at the nanoscale.[1] Therefore, a great deal of effort has been put forth to develop syntheses aimed at growing nanomaterials with desired morphological features. The two most common methods utilized to synthesize nanomaterials include (1) wet chemical reduction for the synthesis of colloidal or solution-phase nanoparticles and (2) physical vapor deposition for supported or substrate-based nanoparticles. This dissertation will discuss new routes which encompass both methods to realize a new class of substrate-based nanostructures whose characteristics such as size, shape, composition, structure, porosity and faceting are readily tunable. In particular, the elements in focus are the Group 10 & 11 (rows 1 - 3) transition metals, shown in **Figure 1.1**.

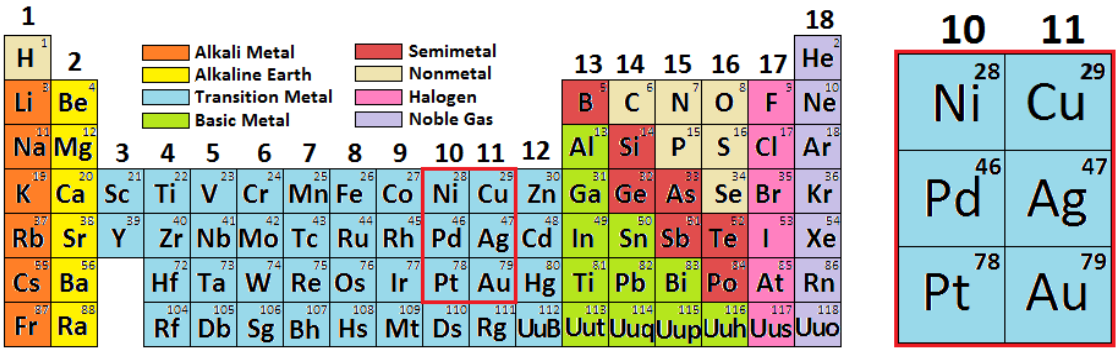

Figure 1.1 A partial representation of the periodic table excluding the Lanthanide and Actinide series. Boxed in red are Groups 10, 11 (Ni, Cu, Pd, Ag, Pt and Au), which include the elements of interest.

1.2 Synthesis of Colloidal Nanoparticles

In 1857, Michael Faraday was the first known scientist to document the synthesis of colloidal Au nanoparticles by reducing gold salts with organic compounds or phosphorous.[2] He was also among the first to correlate the strong red color with the small size of the Au nanoparticles which he attributed to the "finely divided metallic state".[2] It wasn't until 1937 these remarkable assertions could be verified through direct observation provided by a transmission electron microscope (TEM).[3] The TEM, both then and now, provides researchers the ability to systemically relate their synthetic conditions with the morphology of their nanoparticle products, a necessity in the scientific process.

Among the most well-known nanoparticle synthesis routes is that of Turkevich, who, in 1951 showed that narrowly distributed colloidal gold (~ 20 nm in diameter) could be formed by reducing tetrachloroauric acid ($AuCl^{4-}$) with sodium citrate ($Na_3C_6H_5O_7$).[4,5] This processing route, among others, set the stage for what has become roughly six decades of colloidal synthesis aimed at engineering nanoparticle shape, size, composition, porosity and structure (i.e. solid vs. hollow, coreshell, heterostructures and combinations).[6]

Chemical reduction, like the one carried out by Turkevich, is still exists as the most popular methods for the synthesis of colloidal nanoparticles,[7] among many others[8]. A prototypical chemical reduction reaction involves the injection of a reducing agent into a solution containing a metal ions, as shown in **Figure 1.2**. Common reducing agents include sodium borohydride, hydrazine, hydroxylamine, sodium citrate, sugars, alcohols, aldehydes, amides and amines.[8] These reducing agents directly donate electrons to the metal cations resulting in the formation of metal atoms which undergo homogeneous

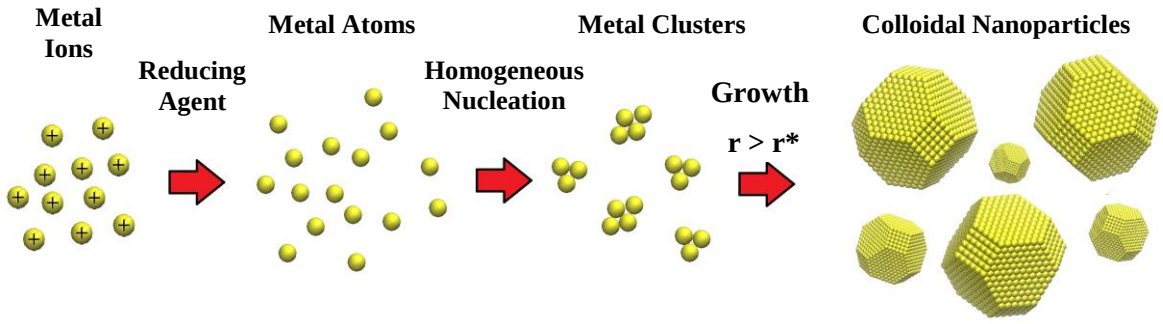

Figure 1.2 The schematic shows the reduction of metal ions with a reducing agent and subsequent homogeneous nucleation and growth into colloidal nanoparticles.

nucleation leading to crystal growth. Continuous growth only occurs if thermal fluctuations produce clusters greater than a critical radius r*, a value defined by both the volume- and surface-free energy terms.[9]

The straightforward reduction of metal ions produces an impressive distribution of colloidal nanoparticles. Should a residual charge (resulting in an electrostatic repulsion) between nanoparticles be insufficient to prevent collision, increasing time will result in flocculation and precipitation (which in most cases is unfavorable). Flocculation is a result from the van der Waals attraction between diffusing nanoparticles. To prevent this phenomenon, a chemical agent can be added (either before or after the synthesis) in the form of ligands, surfactants, ions, capping agents or stabilizers.[10] These agents serve to add an electrostatic repulsion between nanoparticles, effectively inhibiting collisions which lead to flocculation. The theoretical foundations of colloidal stability were first postulated by Derjaguin, Landau, Verwey and Overbeek, (called the DLVO theory); a framework which continues to successfully describe the interplay between electrostatic forces, vdW forces and temperature.[11,12]

The size distribution and expressed morphological features of the resultant colloids can be tuned effectively by (i) choice of capping agents (which modulates surface energy)[13],

(ii) plasmonic excitation[14], (iii) radiation[15] and as discussed by Lim *et al.* (iv) pH, (v) temperature, (vi) precursor concentration, (vii) ionic strength, (viii) reduction potential and (ix) injection rate.[16] Since nanoparticle growth is very sensitive to all of these parameters, the governing mechanisms are often difficult to decipher.

1.3 Synthesis of Substrate-based Nanoparticles

Physical vapor deposition (PVD) is a gas-phase synthesis route which involves the generation of a metal vapor, the impingement of metal vapor on a given substrate and then homogenous or heterogeneous nucleation and growth of a metal film. There are a number of methods utilized to source metal vapor to a substrate including sputter deposition[17], arc discharge[18], laser ablation[19], thermal evaporation[20] and electron beam based methods[21].

Chemical vapor deposition (CVD), another popular gas-phase technique, involves a substrate exposed to a gaseous precursor which reacts and deposits a desired material onto the surface while the gaseous byproducts are constantly exhausted away by a continuous flow of gas.[22] A variation of CVD is known as atomic layer deposition (ALD), a self-limiting reaction which allows for growth of atomically specified thicknesses.[23] ALD processes typically consist of binary reaction sequences involving two surface reactions to form a binary film. The finite number of surface sites constrains the reaction to a finite number of surface reactions and since each of the two surface reactions is self-limiting, the two reactions can proceed sequentially, producing an atomically thin film.[23]

All materials synthesized in this dissertation involve the room temperature sputter deposition of a metal onto an oxide substrate. Under these conditions, the metal adatoms tend to grow/assemble on the surface according to the Volmer-Weber growth mode

(*discussed in section 1.3.1*),[24,25] a mode characterized by strong adatom-adatom interactions resulting in the early stage formation of discrete irregular islands but where continual deposition causes the islands to merge and form a continuous polycrystalline film.

1.3.1 The Growth of a Thin Film via Sputtering

The vapor phase deposition of atoms onto a substrate is inherently a non-equilibrium phenomenon.[26] In other words, during the deposition, the system of adsorbed atoms (adatoms) has not sufficient time nor energy to probe the potential energy field to settle into positions which minimize their overall surface energy (*or* attain thermodynamic equilibrium). During sputter deposition, the process of adatom assembly is largely determined by the ratio of surface diffusion rate, **D**, to the flux of atoms arriving to the surface, **F**,[26] where the final location for a given adatom is governed by a competition between kinetics and thermodynamics. Surface diffusion can be imagined as adatoms hopping from site-to-site with rates defined by Arrhenius law ($k = Ae^{-V/k_BT}$), where A is related to the hopping distance, V is the energy barrier from site-to-site, k_B is Boltzmann constant and T is temperature.[27] Growth processes are typically described in terms of (i) surface energy, (ii) temperature, (iii) incident flux, (iv) adatom-adatom and adatom-

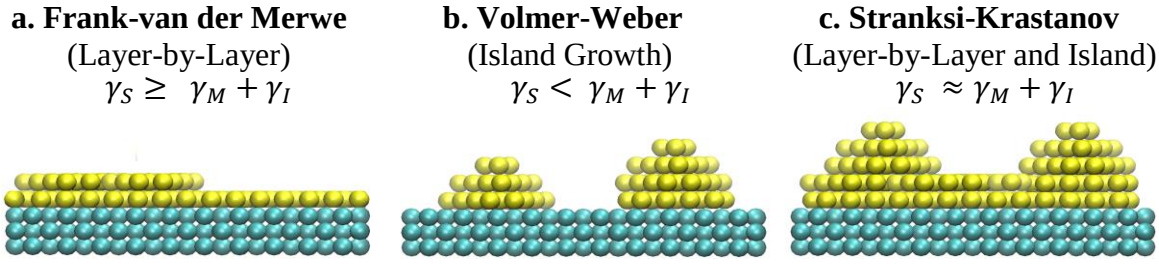

Figure 1.3 Shown schematically are three growth modes: a) Frank-van der Merwe, b) Volmer-Weber and c) Stranksi-Krastanov. Parameters γ_S, γ_M & γ_I are surface-energies for the air-substrate interface, air-metal interface and metal-substrate interface, respectively.

substrate attractive forces and (v) surfactants/impurities.[26,27] Depending on these parameters, there are three observed growth modes including (a) Frank-van der Merwe, (b) Volmer-Weber, and (c) Stranksi-Krastanov (**Figure 1.3**).

Description of the Growth Modes:

An important point to be made prior to discussions about film growth in terms of surface energy is that considerations are defined by thermodynamic equilibrium. This is not necessarily attained should large kinetic barriers hinder the growth process. Despite this, knowing how the system will evolve provides a valuable measure for choosing substrate materials, temperatures, deposition conditions, etc.

Frank-van der Merwe Growth **-** characterized by atoms assembling in a layer-by-layer fashion **Figure 1.3a**. Atoms preferentially assemble at the step edges of a growing film. This mode is typically observed when the attractive force between metal adatoms is much less than the attraction between atoms and the substrate. Consideration of surface-energies points to a *relatively* energy-expensive substrate-air interface where $\gamma_S \geq \gamma_M + \gamma_I$.

Volmer-Weber Growth **–** a growth mode observed throughout this dissertation; the atoms assemble into discrete 3-dimensional islands **(Figure 1.3b)**, typically observed when highly dissimilar materials are interfaced.[26] This growth-mode is shown in **Figure 1.4**; where TEM micrographs capture the morphological features of the sputter deposition of Cu onto SiO_2 (**Figure 1.4 a-e**). Early stage growth is characterized by the formation of a high areal density of Cu islands (**Figure 1.4 a,b**), which, as growth continues (**Figure 1.4**

b), eventually merge to form a network of grains. Continued growth (**Figure 1.4 d,e**) results in the formation of a polycrystalline thin film. This mode occurs when the sum of the metal-substrate surface energy and metal-air surface energy are greater than substrate surface energy. ($\gamma_S < \gamma_M + \gamma_I$) Since the formation of a metal-air surface and metal-substrate interface relatively are more expensive, the areas expressed by these surfaces are minimized by shaping the metal into a sphere (a minimum surface to volume ratio) and decreasing the effective contact area between the metal and substrate.

Stranksi - Krastanov Growth **–** characterized by a layer-by-layer growth mode which, upon reaching a critical thickness, grows according to an island growth mode. The governing factors responsible for this growth mode are still under investigation.[28] However, this type of growth mode is typically observed when the sum of the metal-substrate surface energy and metal-air surface energy are roughly equal to the substrate surface energy. ($\gamma_S \approx \gamma_M + \gamma_I$)

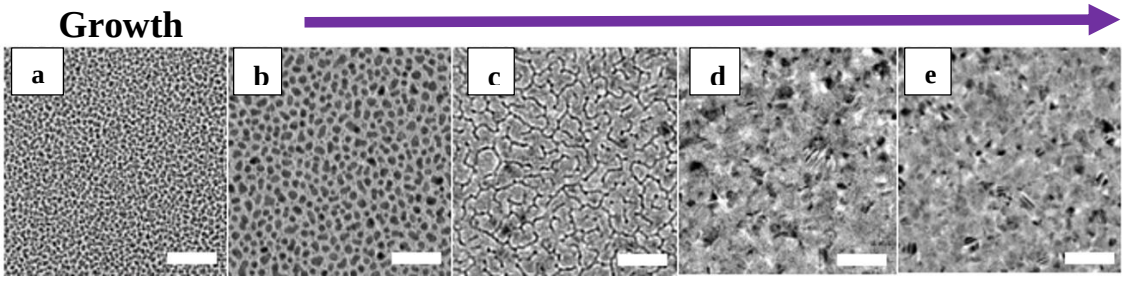

Figure 1.4 TEM characterization of the Volmer-Weber growth mode for the sputter deposition of Cu on SiO_2 at 1, 3, 5, 10 and 40 nm. Scale bar is 50 nm.

1.3.2 Thermal Dewetting

As previously discussed, the vapor phase deposition of a high surface energy material (i.e. a metal) on a low surface energy substrate (i.e. an oxide) results in the formation a

metastable metal thin film where atoms are locked into their position due to kinetic barriers (**Figure 1.4**). If however, directly after deposition, the sample is heated such that the atoms gain enough energy to overcome these remaining kinetic barriers, the system will continue to evolve toward equilibrium. This assembly process is known as thermal dewetting and is one of the most straightforward routes for synthesizing substrate-based metal nanoparticles. **Figure 1.5a** shows this process schematically, where first a metal (i.e. Au) is deposited on an oxide surface (i.e. Al_2O_3 or SiO_2) and then heated. A tilted SEM image of the thermally self-assembled Au NPs on (0001)-sapphire is shown in **Figure 1.5b**. This process, carried out at 1100 °C, results in the formation of single crystal nanostructures firmly chemisorbed to the surface of an oxide substrate with morphologies consistent with that of the Wulff configuration or truncated octahedron (for FCC crystals). (*Details in sections* **2.2** & **2.3**). The resultant sizes, areal densities, shapes and crystal orientations are strongly influenced by the deposition and annealing conditions, film thicknesses, impurities and substrate parameters including surface texture, crystal structure, and orientation.

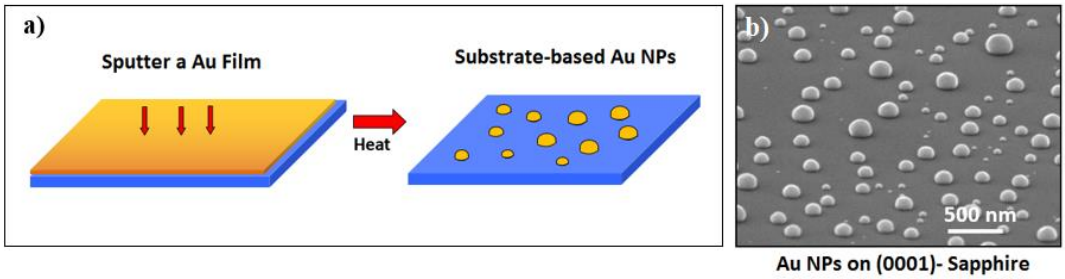

Figure 1.5 The preparation of substrate-based nanoparticles involves a) the sputter deposition of a metal thin film, heating and self-assembly of Au nanoparticles. b) Tilted view SEM micrograph of thermally assembled Au nanoparticles on a sapphire substrate.

1.3.3 Dynamic Templating: A Directed Assembly Process

While thermal dewetting provides a convenient high throughput method for the fabrication of metal nanostructures on surfaces, it suffers from two major disadvantages which include a (1) wide size distribution and (2) lack of control over position. To overcome these disadvantages, a technique called *Dynamic Templating* was invented by our group.[29] This technique is a simple, inexpensive and serves as a versatile route for the templated assembly of metal nanoparticles ordered in periodic arrays on a surface. The schematic in **Figure 1.6** shows this process step-step where (a) first a commercially available shadow mask is placed onto the substrate, (b) antimony and then (c) a metal (i.e. Au, Ag, Ni, Cu, Pt)[29] is sputter deposited through the shadow mask, (d) the mask is removed leaving behind antimony-metal pedestals on the substrate, (e) the sample is heated to temperatures which causes antimony to sublimate (*completely*) and the metal to assemble at the center of the pedestal location, resulting in a periodic array (**Figure 1.6-3**).

The governing assembly mechanisms, shown in **Figure 1.6-2**, involve the following key requirements: (i) the rapid loss of material from the pedestal through sublimation (or evaporation), (ii) the preferential loss of this material from the pedestal sides due to the inhibition of the sublimation process (or evaporation) by material atop the pedestal and (iii) the formation of a liquid at the interface between the pedestal and the agglomerating material. Success of this process is reliant on maintaining a quasi-continuous capping layer which inhibits the sublimation through the pedestal top, and thus, the dissolution of the antimony into the metal is likely a key mechanistic requirement. In summary, the net effect is a highly anisotropic sublimation process which continuously reduces the top surface area of the pedestal until all the material is driven to the center and a single metal nanostructure

is left behind once all antimony sublimates/evaporates. The final product is shown in **Figure 1.6–3**, where a hand holds a sapphire substrate which supports an array of Au nanoparticles made using Dynamic Templating.

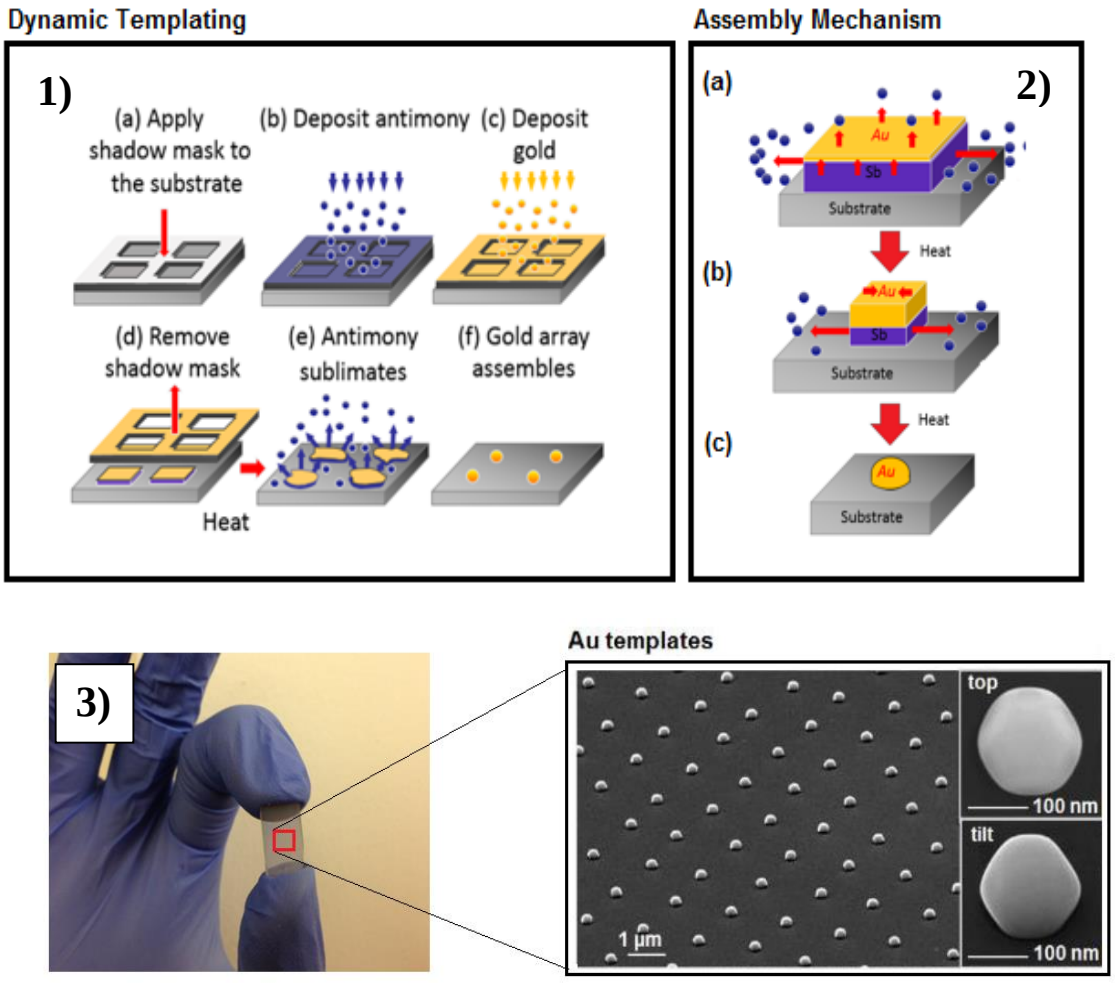

Figure 1.6 In 1) shows a schematic of the processing route involved in dynamic templating. In (1a) shows the placement of a shadow mask a substrate, then the sputter deposition of first (1b) antimony and then (1c) gold. Then the (1d) mask is removed, and the sample is (1e) heated with (1f) the end result being a periodic array of gold nanoparticles. The assembly mechanism is shown in 2a-c. As the pedestal is heated, 2a) antimony beings to sublimate from the sides of the pedestal where continuation leads to 2b) forced inward diffusion of Au and finally 2c) assembly of Au into a single particle and complete removal of antimony. 3) A photograph (left) and SEM image (right) of a periodic array of Au seeds (tilt 45˚) on (0001)-sapphire. Images 1 and 2 were reproduced by permission of The Royal Society of Chemistry.

1.4 The Advantages of Substrate-based Nanomaterials

There are a number of advantages derived from working with substrate-based nanoparticles as compared to colloidal nanoparticles including:

(1) ***Enhanced Stability:*** Thermally assembled nanoparticles are, for the materials and substrates herein discussed, well bonded to the substrate. This immobilization protects nanoparticles, upon exposure to chemicals and/or immersion into the various solvents, against flocculation. Colloidal nanoparticles, on the other hand, are extremely sensitive to chemical additives such as (i) ions[30], (ii) acid or bases[31], (iii) heating[32], (iv) ligand exchange[33], (v) light[34] and (vi) gases[34] which tend to induce flocculation.

(2) ***Nanoparticle Surfaces Devoid of Ligands/Surfactants:*** The thermally assembled structures have the advantage of being free from ligand/surfactants which make these structures fundamentally unique from colloidal nanoparticles which are reliant on ligands for stability. The presence of ligands is known to (i) hinder heterogeneous catalysis by reducing the apparent reaction rates,[35] (ii) alter the surface free energy,[10] (iii) modulate hot-electron lifetimes,[36] (iv) change the local refractive index of the functionalized nanoparticle causing a shift in the plasmon resonance,[7] and lastly (v) add additional ambiguity to processes such as homo/heterogeneous nucleation, galvanic replacement reactions, surface diffusion, or more generally, any process occurring at the surface. It's also important to note that self-assembled nanoparticles can themselves be functionalized with ligands, making this platform ideal for establishing systematic comparisons between ligand and ligand-free states.

(3) ***Epitaxial Alignment:*** The crystallographic orientation of the substrate can be used to dictate the crystal direction of the assembled nanoparticle. A nice example, and one which

is used repeatedly, is the thermal assembly of Au on (0001)-sapphire. The hexagonal packing of the atoms in the (0001)-sapphire provides the atomic geometry ideal for the formation of [111]-oriented Au structures. These facts can be established qualitatively with SEM (top view reveals 6-sided hexagonal structures) or quantitatively with X-ray diffraction data (***discussed in section 3.5***) which shows two dominant crystallographic orientation relationships of $(111)[-211]_{Au}\|(0001)[11\text{-}20]_{sapphire}$ and $(111)[2\text{-}1\text{-}1]_{Au}\|(0001)[11\text{-}2\ 0]_{sapphire}$.

(4) ***Substrate Synergism:*** It has been proven extensively that the substrate can play an active role in chemical reactions.[37] For example, metal nanoparticles supported on semiconductor supports have shown to be more catalytically active as compared to substrates comprised of dielectric materials.[38] Arguably the best example of this is provided by Widmann and Behm where CO reduction rate (CO_2 formation) is shown to be dependent on the substrate material where the rates order such that $Au/TiO_2 > Au/ZrO_2 > Au/ZnO > Au/Al_2O_3$; concluding, in this case, that the use of a reducible substrate material (i.e. TiO_2) leads to active catalysis but where nonreducible materials (i.e. Al_2O_3) are inactive. This is one example of the important role the substrate *can* play in chemical reactions occurring on supported materials.

(5) ***Access to a Variety of Materials:*** The vapor phase deposition of transition metals onto a surface is a very quick and inexpensive process. More important is the fact that your choice of metal is virtually unrestricted, so long as the metal target is available. This may not be so true when working with nanomaterials in the colloidal form, where, applications utilizing colloidal nanoparticles are typically developed once mature synthetic protocols

have already been established. Therefore, nanomaterial syntheses carried out in the vapor phase provide rapid access to a variety of materials ideal for systematic comparisons.

(6) ***Same Particle Characterization by use of Surface Alignment Markers:*** One of the greatest advantages of working with nanoparticles on surfaces is the fact that the *same* nanoparticle can be characterized before, during and/or after a given reaction.

(7) ***Ideal Platform for Dip-Catalysis:*** The utility of colloidal nanoparticles as heterogeneous catalysts is drastically hindered from the fact that these nanoparticles need to be recovered from the reaction vessel once a given reaction is complete. Recovery can take the form of filtering, centrifugation, or use of magnetism.[39] To address this shortcoming, the dip-catalyst modality can be employed which involves the attachment of nanoparticles to a support (glass[40], filter paper[41]) and cycled from one reaction to the next. *(Several dip-catalyst platforms are discussed in* ***Chapter 9****)*

(8) ***Tuning the Plasmon Resonance:*** The placement of nanoparticles onto an oxide substrate, from either air or water, causes the plasmon resonance to red shift.[42] This is observed when metal nanoparticles are either encapsulated or in contact with materials with higher refractive index including the commonly used substrates: sodalime glass (SLG), silica glass (SiO_2), sapphire (Al_2O_3), indium tin oxide (ITO), magnesium oxide (MgO) which all have $n > 1.4$. Lastly, it's important to note that the placement of metal nanoparticles on conducting substrates (i.e. ITO, FTO), can serve as a means apply an electric potential to carry out electrochemistry on single metal nanoparticles.[43]

1.5 The Applications of Plasmonic Nanoparticles

The applications which utilize metal nanostructures span many fields and can be summarized by the web below (**Figure 1.7**). Of particular relevance to this dissertation include applications such as photochemistry[44], catalysis[45,46], energy harvesting[47], ultra-high contrast biological imaging[48], cancer therapy[49], surface enhanced Raman spectroscopy[50], plasmon mediated nanostructure growth[51] and solid state hot-electron based solar cells[52]. These applications can be generally grouped into five broad categories which include catalysis, sensing, electronics, biomedical and energy applications.

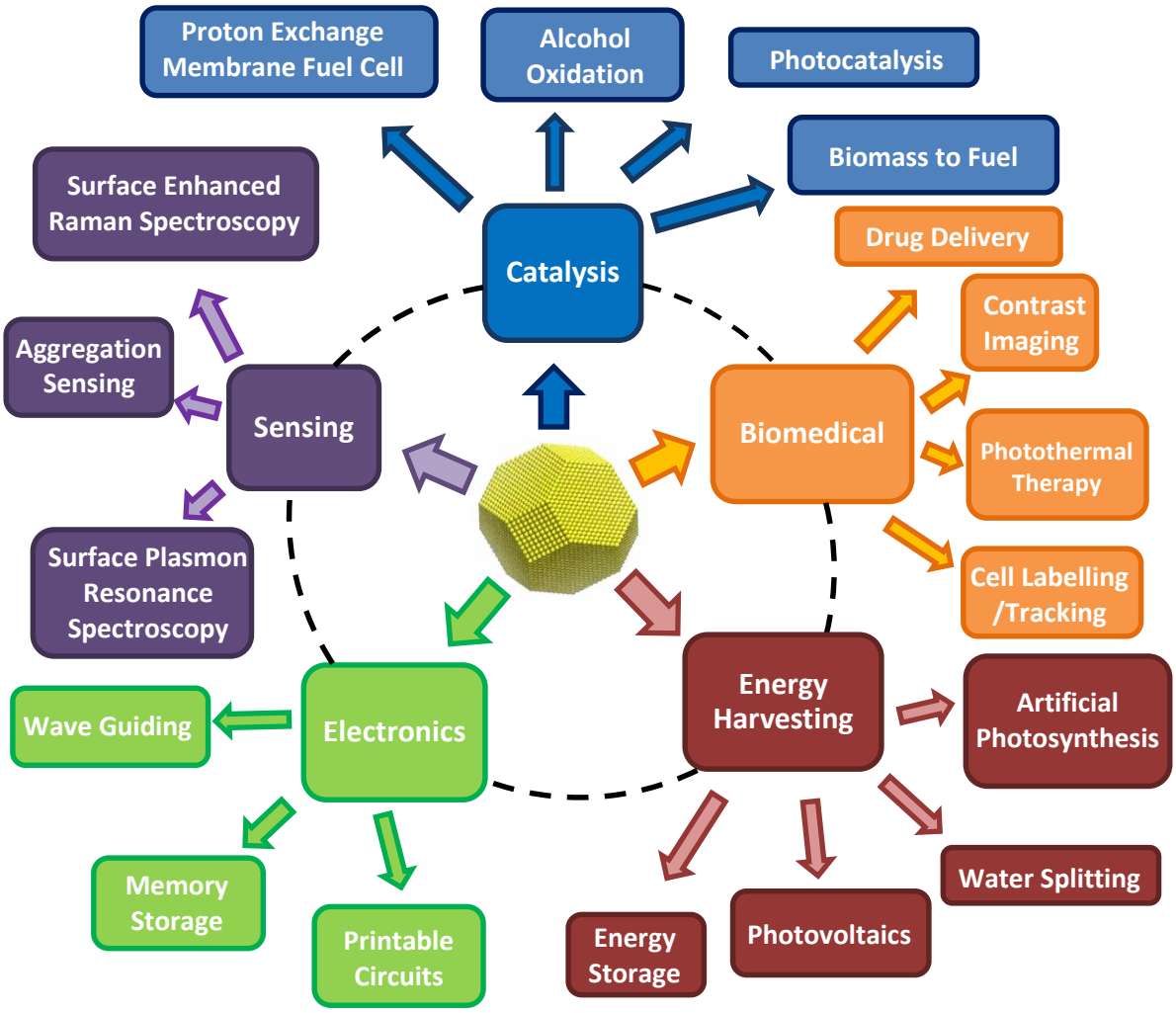

Figure 1.7 A web representing the many applications of metallic nanoparticles.

CHAPTER 2

CONCEPTS AND MATHEMATICAL FOUNDATIONS

2.1 The Tunable Properties of Metal Nanoparticles

The hallmark of nanotechnology is the ability to tune the chemical and physical properties of nanomaterials through adjustments made to size, shape (i.e. faceting), composition (bi-, tri- and multimetallic platforms) and morphology (solid, hollow, porous, etc.). Before discussing the fundamental changes to properties, its good practice to realize the increases to surface area when the bulk is reduced to nanosizes. Take for example a gold cube with a mass of 1 mg reduced to mono-dispersed nanoparticles with diameters of 5 nm (**Figure 2.1**); a process which increases the surface area by a factor 7.5×10^4.

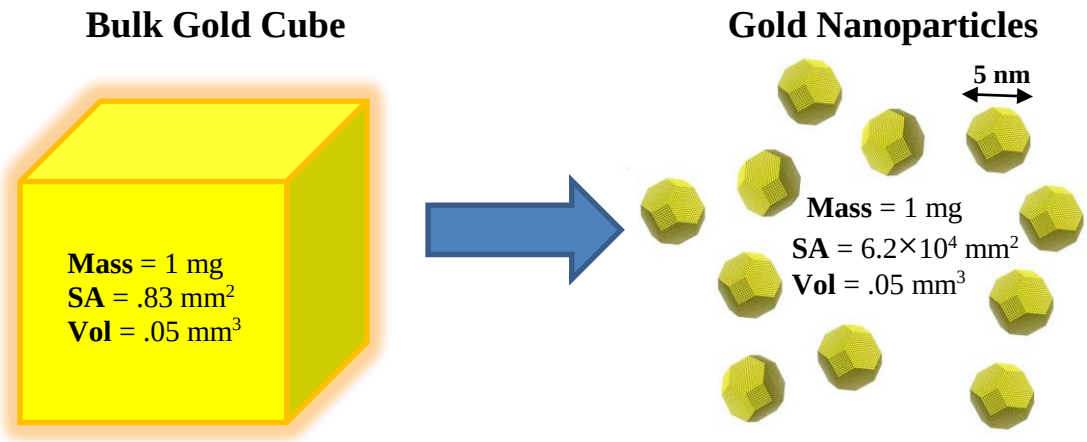

Figure 2.1 A simple demonstration of the increase to SA upon reducing the size of material to the nanoscale.

2.1.1 Size Dependent Properties

Apart from the high surface area to volume ratios attainable, nanoscaled particles exhibit properties unique from the bulk. As stated by Roduner, the exhibition of these unique properties can be attributed generally to (1) surface effects and (2) quantum effects.[53]

(1) **Surface effects**: As a material becomes reduced down to smaller and smaller dimensions, there are a relatively larger number of atoms at the surface.[53] Intrinsic to surfaces are atoms exhibiting a fewer number of nearest neighbors as compared to atoms in the bulk, giving rise to a drastically higher density of edge and corner sites which have an even lower coordination capable of binding foreign molecules more tightly.

(2) **Quantum Effects**: Solutions to the Schrödinger equation provide the wave function for a given system of particles (*i.e. electrons*) in a known spatial confinement and given potential. Since the wave function of the conduction electrons are delocalized over the entire particle, the electrons can be treated as 'particles in a box'.[53] The wave function and possible energies of a given system of particles are dependent on the confinement conditions (i.e. the size of the box), therefore, their energies can be tuned accordingly.[53] Therefore, the ability to form bonds, propensity to take part in redox reactions or simply interact with other systems can all be tuned through size modifications.

2.1.2 Shape Dependent Properties

The expressed faceting of a given nanoparticle dictates the overall shape. For example, an FCC nanoparticle expressing all (111) – facets takes the shape of an octahedron, or for all (100) – facets, the shape of a cube. Since each facet contains a different packing symmetry and planar density of in-plane atoms (or coordination), the stability/reactivity for each facet is different. Applications such as catalysis is dependent on making and breaking bonds with molecules. Therefore, the reactivity which depends on faceting, is paramount in determining catalytic efficacy. An excellent example for the shape dependent catalytic activity was demonstrated by the Xia group, where the electrooxidation of formic acid was measured against nanoparticles expressing completely (111) – facets,

nanoparticles with completely (100) – facets, and nanoparticles exhibiting mixed combinations of both (111) and (100) facets (**Figure 2.2**).[54] An increase in catalytic rate is observed when gradually changing shape from octahedron to cube.

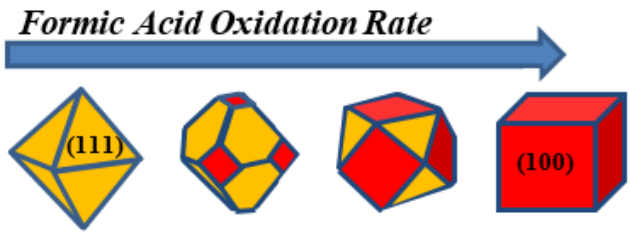

Figure 2.2 Shown schematically is the evolution of octahedron to the cube morphology. The rate of electrooxidation of formic acid is shown to increase as the shape tend toward a cube, or (100)-facets.[54] This process provides an excellent means for determining the role of facet type in catalysis.

2.1.3 Composition Dependent Properties

Multimetal nanoparticle catalysts have attracted considerable attention over that of the monometallic platform due to (i) reduction in precious metal used and (ii) improvements to quality and properties of catalysts.[55] Multimetal nanoparticles are known to display intermediate properties consistent with each constituent element.[56,57] One example of the utility in multimetal nanoparticles can be realized when considering Au. Since Au is one of the most ubiquitous materials in use, alloying with other materials will not only reduce the usage of Au, but also provide additional property tunability.[58] This rationale is the same for Pt, a material which is and will continue to be heavily used in polymeric electrolyte fuel cells (PEFC). According to Sealy, assuming each fuel cell vehicle requires 15 g Pt, approximately 5 billion can be manufactured, enough to meet the demand.[59] Therefore, the search for a multimetal catalysts comprised of inexpensive and available materials will not only reduce the demand for Pt but also potentially enhance the efficacy of the catalyst, making PEFC's economically feasible.

2.2 The FCC Crystal Structure

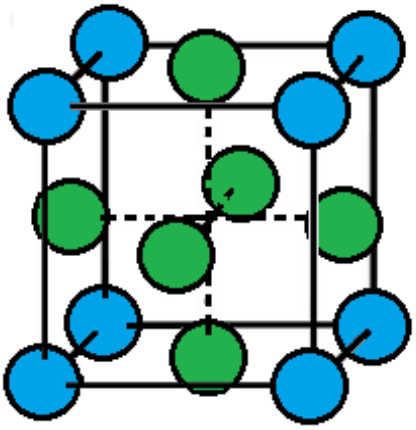

Figure 2.3 The FCC lattice.

The physical and chemical properties of materials depend critically on how atoms assemble into 3D lattices. The elements in Group 10 & 11 (the first three rows) form a Face Centered Cubic (FCC) crystal lattice as depicted into **Figure 2.3**, having an atom at each corner (blue) and one at the center of each face (green) of the cubic cell, giving an atom embedded in the bulk a total of 12 nearest neighbors. While the bulk ordering of atoms has a large effect on physical properties (elasticity, electrical and thermal conductivity, etc.), the chemical interactions between nanoparticles and the external environment are largely dictated by the arrangement of atoms at the surface. For FCC nanoparticles, facet expression is typically characterized by a combination of the three low index facets; the (111), (100) and (110). The most stable (or lowest energy facet) is the (111) facet, where atoms have a hexagonal packing (**Figure 2.4a**). Each atom in (111)-plane has a coordination number of 9, the highest possible among facets. While in-plane atoms are well bonded, atoms which rest directly on the (111)-plane only have a coordination of only 3, a feature conducive to (i) high atomic diffusion and (ii) lower reactivity (*with respect to reactions later discussed in Chapters 4 – 9).* The (100)-facet is the second most stable facet, hosting atoms with an in-plane and on-plane coordination of 8 and 4, respectively (**Figure 2.4b**). Lastly, the (110) facet is the most energetically expensive to create (among low index facets), having an in-plane and on-plane coordination of 7 and 5, respectively (**Figure 2.4c**).

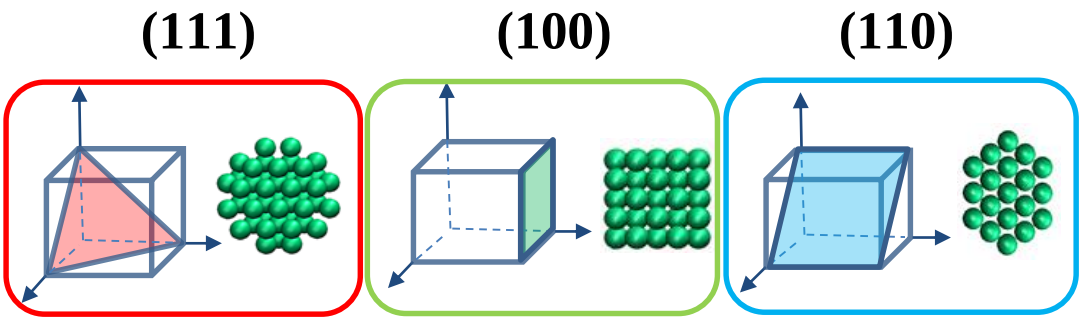

Figure 2.4 The low index facets for an FCC crystal consisting of a) (111) b) (100) and c) (110). The respective planes are shown in a cubic cell. Adjacent to each cubic cell is the manner in which atoms pack into the respective plane.

2.3 Surface Energy

The term surface energy (γ), or surface *free* energy, is used to quantify the disruption of intermolecular bonding of a surface. In other words, it is the amount of energy required to create a given surface from the bulk. This concept is best understood if imagined as a perfect crystal which is separated into two halves along a plane defined by one of the low index facets of an FCC crystal (i.e. (111), (100) or (110)). The energy required to create these two new surfaces, divided by the total area, is the surface free energy. The knowledge of surface energy is an invaluable tool when shape engineering nanostructures as it provides the *how* and *why* atoms tend to assemble into observed morphologies. **Table 2.1** provides a list of surface energies for the metals of interest.

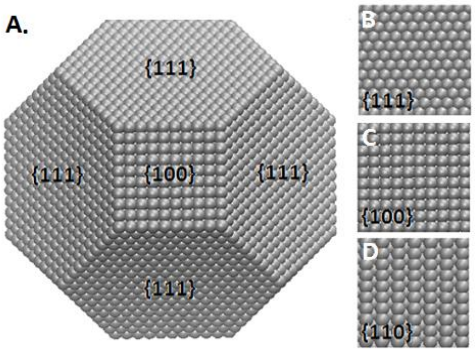

Figure 2.5 A) Shown above from the [100]-axis is the low energy Wulff configuration comprised of both (100)- and (111)-facets. The atomic packing for B) (111), C) (100) and D) (110)-facets are shown.

Differences in surface energy among atomic planes can be realized by considering the atomic packing at the interface. As stated previously, an atom resting in a (111)-facet is bonded to 9 other neighbors whereas the (100)- and (110)-facets have 8 and 7, respectively. Therefore, it is understood that the formation of a high energy facet will require the breaking of more bonds per area, an energetically expensive event.

Table 2.1 Surface Energies

Metal	Surface energy[60], (eV/atom; J/m^2)		
Ni	(111)	0.695	2.011
	(100)	0.969	2.426
	(110)	1.337	2.368
Cu	(111)	0.707	1.952
	(100)	0.906	2.166
	(110)	1.323	2.237
Pd	(111)	0.824	1.920
	(100)	1.152	2.326
	(110)	1.559	2.225
Ag	(111)	0.553	1.172
	(100)	0.653	1.200
	(110)	0.953	1.238
Pt	(111)	1.004	2.299
	(100)	1.378	2.734
	(110)	2.009	2.819
Au	(111)	0.611	1.283
	(100)	0.895	1.627
	(110)	1.321	1.700

In 1878, Gibbs presented a fairly simple mathematical interpretation of these notions.[61] He defined ΔG as the difference in energy between a crystal of finite dimension versus that of the same crystal imbedded in an infinitely large crystal. Proposed was that the equilibrium shape of the nanocrystal will be one such that the ΔG is minimized, where the Gibbs free energy change is given by:

$$\Delta \mathbf{G} = \sum_{\mathbf{k}} \boldsymbol{\gamma}_{\mathbf{k}} \mathbf{A}_{\mathbf{k}} \qquad \textbf{(1)}$$

Where surface energy (γ_k) and area (A_k) is representative of any facet "k". Since the low index facets are more stable than that of the higher index facets, an accurate solution can be attained by only considering that of the (111)-, (100)- and (110)-facets. An example of a prototypical low energy Wulff configuration is provided in **Figure 2.5**, which shows the expression of (111)- and (100)-facets, where area of the (111) is slightly higher than that of the (100) due to that fact that $\gamma_{111} < \gamma_{100}$. The substrate also plays a role, but mostly with respect to contact angle formed between the surface and nanostructure.

Assembled metal nanostructures on low-surface energy substrates give rise to structures with large contact angles. Assembly on high-surface energy substrates result in flat or hemispherical structures.[62]

2.4 Galvanic Replacement Reactions

A galvanic replacement reaction is an electrochemical process involving the oxidation of one metal (i.e. template) by the ions of another metal with a higher reduction potential.[66] This interaction results in the oxidation and dissolution of the template while the ions of the second metal become reduced and plated onto the template. This straightforward reaction is the most popular approach for synthesizing hollow nanomaterials. The mechanistic details of this reaction carried out on thermally assembled templates are discussed in Chapter 4 – 6. In the next section, an introduction to the governing chemical thermodynamics is provided.

2.4.1 The Nernst Equation

In the early 1900's, Walther Nernst, a German Physicist and Nobel Laureate, developed the mathematical constructs for a number topics related to solid state physics, thermodynamics, electrochemistry and physical chemistry.[63] His contributions to electrochemistry, notably the Nernst Equation, are immediately relevant to the galvanic replacement reactions used in the formation hollow metal nanoparticles. The Nernst equation relates the reduction potential of a given half-cell reaction to temperature, reaction quotient and standard cell potential. A galvanic replacement reaction, between a solid and metal ion species, can be represented by n-number of metal ions (A^{m+}), which have a higher reduction potential, that oxidize m-number of neutral species (B^{o}) having a lower

reduction potential. The end result is n-number reduced species (A^o) oxidized by m-number of species (B). The complete redox reaction is given by:

$$\mathbf{nA^{m+} + mB^{o} \leftrightarrows nA^{o} + mB^{n+}} \quad \textbf{(2)}$$

The complete redox reaction can be written as half reactions:

$$\mathbf{nA^{m+} + m\,e^{-} \rightarrow nA^{o}} \quad (\textbf{reduction}) \quad \textbf{(3)}$$

$$\mathbf{mB^{o} \rightarrow mB^{n+} + ne^{-}} \quad (\textbf{oxidation}) \quad \textbf{(4)}$$

Each half reaction has a tabulated reduction potential describing the tendency for the given species to gain electrons or become reduced (*hence reduction potential*). The species with a higher (more positive) reduction potential will take electrons from (or oxidize) a species having a lower potential. If the half reaction A (the species being reduced) has a reduction potential E^{o}_{red} and the half reaction B (the species being oxidized) has a reduction potential E^{o}_{ox}, the measure of the potential difference between each half reaction is known as the cell potential, E^{o}:[64]

$$\mathbf{E^{o} = E^{o}_{red} - E^{o}_{ox}} \quad \textbf{(5)}$$

The values for a given reduction potential are well established are provided with respect to a given standardized electrode known as a standard hydrogen electrode (SHE). The SHE forms the basis for the thermodynamic sale of redox potentials. **Table 2.2** provides the potentials for the group 10 and 11 metals.[65]

Also of relevance to the Nernst formulation is the relative proportion of reactants to products, formally known as the reaction quotient Q, which can be written as:

$$\mathbf{Q = \frac{[A^{o}]^{n}[B^{n+}]^{m}}{[A^{m+}]^{n}[B^{o}]^{m}} = \frac{[B^{n+}]^{m}}{[A^{m+}]^{n}}} \quad \textbf{(6)}$$

If both $\mathbf{E^o}$ and **Q** are known, the potential of a given oxidation-reduction reaction can be given by (The Nernst Equation):

$$\mathbf{E = E^o - \frac{RT}{zF} \ln Q} \qquad \mathbf{(7)}$$

Where 'E^o' is the standard cell potential, 'R' is the universal gas constant, T is the absolute temperature, 'F' is the Faraday constant (coulombs per mole of electrons), 'z' is the number of moles of electrons transferred in the half-reaction and 'Q' is the reaction quotient.

Table 2.2. The standard redox potentials[65]

Element (Ion)	Redox E° (V vs. SHE)
Ni (Ni^{2+})	-0.26
Cu (Cu^{2+},Cu^{+})	0.34, 0.52
Pd (Pd^{2+})	0.95
Ag (Ag^{+})	0.80
Pt (Pt^{2+})	1.18
Au (Au^{3+})	1.49

2.4.2 Galvanic Replacement on Nanoparticles

The classic example in literature is the galvanic replacement of silver (Ag) with gold (Au). Ag nanostructures are, by far, the most commonly used sacrificial templates for galvanic replacement reaction due to: (i) the relatively low electrochemical potential of Ag (0.8 V vs. SHE, i.e. the standard hydrogen electrode) [66] and (ii) a colloidal chemistry that is both rich and well-established.[67-72] The prototypical galvanic replacement reaction is one where silver templates (nanocubes, cuboctohedrons, nanorods or nanowires) are reacted in an aqueous solution of $HAuCl_4$.[73] In this reaction, the reduction of each Au^{3+} ion results in

the oxidation and dissolution of three Ag^+ ions from the template. While the synthetic pathways are relatively straightforward, the underlying mechanisms guiding galvanic replacement reactions are complex. Silver nanocubes exhibiting six {100}-facets are, from a mechanistic standpoint, a simple template material. Galvanic replacement reactions transform nanocubes into hollow nanoboxes composed of an Au-Ag alloy, [74] where the steps include (i) Au plating onto the Ag template, (ii) the formation of a pit to allow silver to leave the core, (iii) Au diffusion processes which result in sealing and (iv) lastly dealloying, as summarized in **Figure 2.6**. If, however, the reaction is allowed to continue after the nanobox has formed, the structure undergoes morphological transformations, first through the formation of square pores on the cube faces (i.e. a nanocage) and then through fragmentation. Coinciding with this deconstruction is a composition which trends toward pure Au. Many aspects of this progression are well understood. The initial stages of the reaction are characterized by the dissolution of Ag^+ from the surface of the cube as Au^{3+} is reduced and heteroepitaxially deposited as Au^o on the remaining Ag template. The 100 °C reaction temperature is required to prevent the precipitation of AgCl, [75] and is sufficient to cause rapid alloying between the deposited Au and the underlying Ag.[66] Template hollowing is postulated to initiate at a single defect site on one of the six faces of the nanocube. As Au continues to plate the cube the exiting Ag^+ first results in the formation of a pit and then hollows out the interior of the structure until the supply of pure Ag is exhausted. The side-

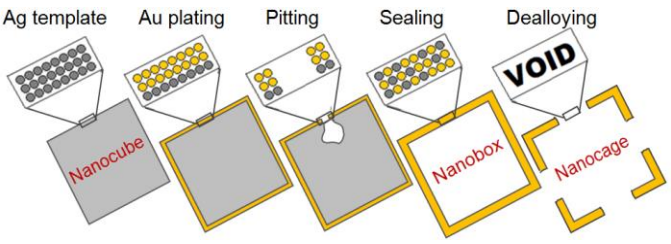

Figure 2.6 Schematic illustrating the various stages of a galvanic replacement reaction carried out on a Ag nanocube template.

opening then seals due to volume diffusion, surface diffusion, dissolution followed by re-deposition or a combination of the aforementioned.[73] At this stage the nanostructure exists as an alloyed Au-Ag nanobox, a structure which preserves the original shape of the template. Longer reaction times lead to a continuation of the galvanic replacement reaction through the slow dealloying of Ag from the walls of the nanobox.[74] Due to the 1:3 Au:Ag replacement ratio, dealloying results in the injection of vacancies and an overall reduction in the number of atoms in the structure. Vacancy coalescence eventually leads to the formation of square pores in the sidewalls of the structure. Continuing the reaction leads to nanostructure fragmentation which results from further dealloying and Ostwald ripening processes.

Structures formed from galvanic replacement reactions on templates with multiple facet types express a greater complexity due to a facet dependent reactivity. For this scenario, the reaction product can achieve a shape which radically differs from that of the original template. Notable examples include templates which are cuboctahedrons,[76] polyhedrons,[77] multiply twinned particles (MTP) [78] and nanowires[79]. The early stages of the reaction are characterized by the preferential deposition of Au on facets having the highest surface energy. With a hierarchy of surface energies of $\gamma\{110\} > \gamma\{100\} > \gamma\{111\}$ for a face centered cubic template, the deposition tends to accentuate the {110}- and {100}-facets at the expense of {111}-facets. With preferential deposition occurring along high surface energy facets, the low surface energy {111}-facets typically become the sites for pitting, hollowing and dealloying-induced void formation.[66]

In addition to the aforementioned studies, there is an emerging importance being placed on the evolving charge distribution within the dissolving template as it undergoes a

galvanic replacement reaction. Such influences result in the unexpected asymmetric hollowing observed in Ag-Au-Ag nanorod structures whereby one end of the structure hollows prior to the onset of hollowing at the opposite end. [80] One research group has shown that palladium nanotube templates form tadpole-like structures instead of the expected nanotube morphology when reduced with Au^{3+}.[79] More recently, [81] these same influences have been used in combination with underpotential deposition[82] on a central nanocrystal to obtain unprecedented control over the nanostructure geometry.

2.5 The Localized Surface Plasmon Resonance

A plasmonic nanostructure, otherwise commonly referred to as a nanoscaled antenna, is capable of absorbing large amounts of light energy. The absorbed light energy manifests itself as large localized electric fields emanating from the nanostructure's surface. These near fields can be as high as $\mathbf{10^2 - 10^3}$ E_{inc} and even $\mathbf{10^4 - 10^5}$ E_{inc} for closely spaced nanoparticles,[83] which have the potential not only enhance technologically relevant chemical and physical processes,[83] but also provide the means to discover new ones.[44]

2.5.1 The Physics of the Light-Matter Interaction

A localized surface plasmon resonance (LSPR) is a coherent oscillation of the conduction electrons in a metal nanoparticle. An incident photon can be used to stimulate the LSPR provided that the frequency of photon matches the resonance frequency of the electrons in the nanoparticle. The resonance frequency for the metals such as Cu, Ag, and Au span the visible region of the electromagnetic spectrum (400 - 800 nm, 1.5 - 3.1 eV), whereas metals such as Al, Cr, Mg, Rh, Ru, Ti, Pt and Pd have resonances in the UV region

(200 - 400 nm, 3.1 - 6.2 eV).[84] Most plasmonics applications deal with Au nanoparticles due to their electromagnetic properties, mature synthetic procedures, resistance to oxidation, biocompatibility, and ease of functionalization.[85]

The parameters which define the spectral position and intensity of the LSPR include electron density, effective mass, particle shape, size, dielectric constant and local environment (i.e. index of refraction, neighboring fields, and temperature).[86] **Figure 2.7** shows the collective oscillation of free electrons induced by a photon resonant with the localized surface plasmon.

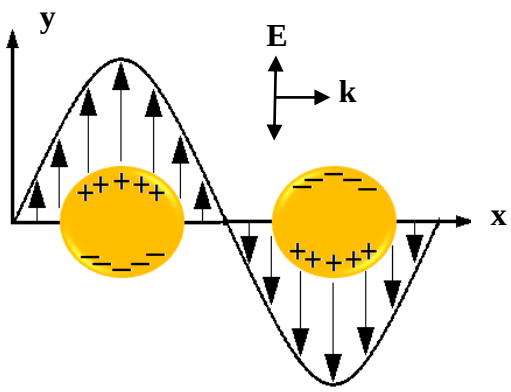

Figure 2.7 The interaction between a metal nanoparticle and a photon resonant with the localized surface plasmon. The conduction electrons couple with the electric-field of the incident photon, causing the electrons to oscillate in phase with the photon. The y-axis is parallel to the incident electric-field where the positive x-axis points in the photon propagation direction, or k-vector.

2.5.2 The Parameters Defining the LSPR

When the diameter of a metal nanoparticle is much less than the wavelength of light, the polarizability '$\boldsymbol{\alpha}$' induced by a photon of angular frequency $\boldsymbol{\omega}$, can be approximated by the Clausius - Mossotti (C-M) relation[87]:

$$\boldsymbol{\alpha = 3V\varepsilon_o \frac{\varepsilon(\omega) - \varepsilon_m}{\varepsilon(\omega) + 2\varepsilon_m}} \qquad \textbf{(8)}$$

Where $\boldsymbol{\varepsilon_o}$ is the permittivity of vacuum, $\boldsymbol{\varepsilon_m}$ is the dielectric constant of the medium, $\boldsymbol{\varepsilon(\omega)}$ and $\mathbf{V}$ are the frequency dependent dielectric constant and volume of the metal nanoparticle, respectively. The dielectric constant is defined by two components, a real

and imaginary part where $\boldsymbol{\varepsilon(\omega) = \varepsilon_r(\omega) + i\varepsilon_i(\omega)}$. One can immediately see that the resonance conditions are met when $\boldsymbol{\varepsilon_r(\omega) = -2\varepsilon_m}$ where $\boldsymbol{\varepsilon_i}$ is assumed to be both small and only weakly dependent on $\boldsymbol{\omega}$.[88] The dielectric constant $\boldsymbol{\varepsilon_r(\omega)}$, is comprised of material properties including electron density, electron mass, interband transitions and electron charge. Upon evaluating the C-M relation, (finding where experimetally derived $\boldsymbol{\varepsilon_r(\omega)}$ – values equate to $\boldsymbol{-2\varepsilon_m}$) approximate theoretical resonances can be tabulated. **Table 2.3** shows these theoretical values for the LSPR of Cu, Ag and Au in air (n = 1.00) and in water (n = 1.33). The right-most column provides a rough range of experimentally observed resonances for colloidal Ag, Au and Cu nanoparticles. Deviations from theory are not surprising since experimentally observed nanoparticles typically have variety of sizes, capping agents (higher index of refraction), defects and aggregates/dipole-dipole interactions, surface oxide (i.e. Ag and Cu, not Au), all contributers to resonance shifting.

Table 2.3 Resonances Based on Clausius- Mossotti Relation

	$\lambda(\alpha_{max})$, nm **n = 1.00**	$\lambda(\alpha_{max})$, nm **n = 1.33**	**λ(obs.),** nm **n = 1.33**
Cu	341	454	520 – 560 [ref 89]
Ag	362	398	390 [ref 90]
Au	483	518	520 [ref 90]

Note: Wavelength values for where $\boldsymbol{\varepsilon = -2\varepsilon_m}$ are from Rakić [91]

2.5.3 The Role of Shape on the Localized Surface Plasmon

Altering the shape of nanoparticles has a profound effect on the localized surface plasmon resonance. This collective oscillation of conduction electrons moves with respect

to the positive lattice, which constantly serves as a restoring force. Nanoscaled features such as corners, edges and pores dictate the magnitude of this restoring force.[92] These morphological features also have a profound effect on the spectral profile of the localized surface plasmon resonance, to the extent that a plasmonic fingerprint can be established for each nanoparticle morphology. As an example, **Figure 2.8** below shows the normalized absorbance spectrum of a gold sphere (red), nanoprism (blue), nanorod (green) and a nanoshell (purple) simulated with DDA, each exhibiting a unique LSPR.

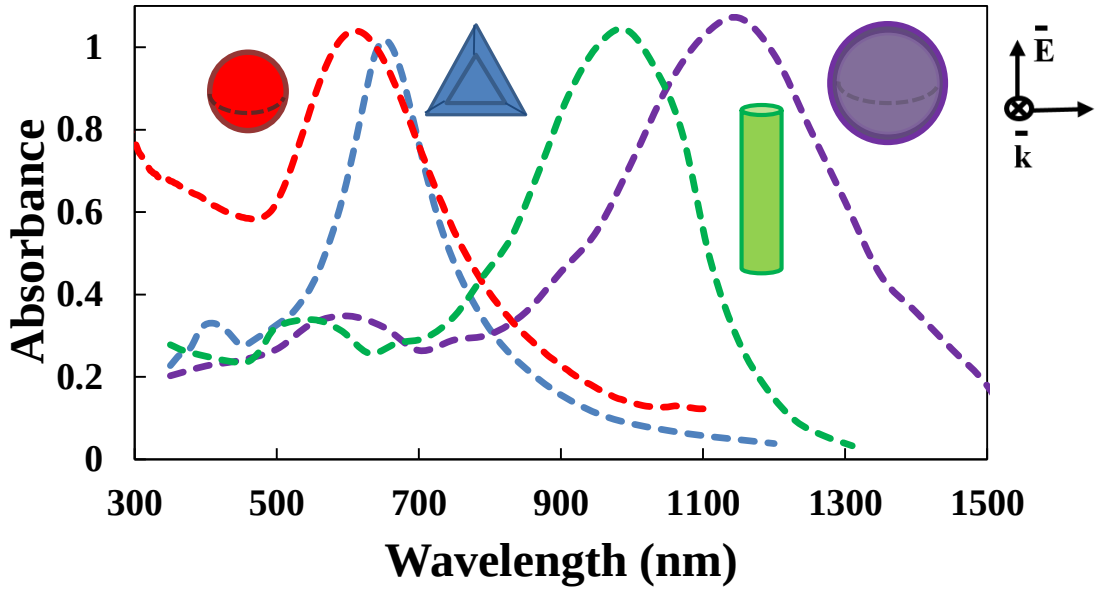

Figure 2.8 The absorbance spectrum is gold sphere (red), nanoprism (blue), nanorod (green) and a nanoshell (purple) simulated with DDA. The sphere has diameter 50 nm, nanoprism edge length and height 50 and 20 respectively, nanorod 50 nm length and 10 nm width and nanoshell 50 nm and 55 nm inner and out diameter respectively.

2.5.4 The LSPR of Supported Nanostructures

The dispersal (or growth) of metal nanoparticles on a surface changes the LSPR spectral position and features.[93] If, for example, nanoparticles are transferred from air (n = 1.00), to water (n = 1.33), the LSPR will red shift. Analogous to this is when nanoparticles are either

encapsulated or in direct contact with materials with higher refractive index including the commonly used substrates: sodalime glass (SLG), silica glass (SiO_2), sapphire (Al_2O_3), indium tin oxide (ITO), magnesium oxide (MgO), where $n_{SLG} = 1.53$, $n_{SiO_2} = 1.46$, $n_{Al_2O_3} = 1.77$, $n_{ITO} = 1.8 – 2.2$, and $n_{MgO} = 1.7$.[91] This is due to the induction of an image charge on the neighboring body which causes not only a red shift in the LSPR but also, in some cases, the expression of new modes.[42] Lastly, it's important to note that if nanostructures are placed too close to one another, dipole-dipole interactions could also drastically red shift the LSPR.[94]

2.5.5 Electromagnetic Simulation Packages

There are a number of software packages available for simulating the interaction between arbitrarily shape metal nanoparticles and incident radiation. Growing in popularity is the user friendly and commercially available Finite-Difference Time-Domain (FDTD) method, offered by Lumerical. The FDTD uses finite differences to approximate the spatial and temporal derivatives in Maxwell's equation. This software is capable of solving for a number of valuable solutions including extinction, scattering, absorbance and the near field.[95]

All simulations carried out in this dissertation were performed using The Discrete Dipole Approximation (DDA). The theoretical inspiration for DDA was sparked in 1909 by Lorentz who realized that the dielectric properties of materials is directly related to the polarizabilities of individual atoms by the Clasius-Mossotti relation (*mentioned previously*).[96] The general idea of DDA was first introduced in 1964 by DeVoe who was investigating the optical properties of molecular aggregates.[97] Later in 1973,

astrophysicists Purcell and Pennypacker used DDA to compute the scattering and absorption of starlight from interstellar dust.[98] The basic idea of DDA involves replacing the particle with a lattice of polarizable points which, upon applying an electric field, acquire a dipole moment. The dipoles respond to both the applied field and also neighboring dipoles. This then is an algebraic problem involving a system of interacting dipoles. DDA is an iterative algorithm capable of approximating the scattering and absorption spectra of arbitrarily shape particles, provided the optical constants are known. In 1994, Draine and Flatau implemented this algorithm in Fortran, calling the code DDSCAT.[99] Summarized below are the key mathematical concepts involved in the algorithm. The simulated particle consists of a 3D-array of polarizable points, which, upon applying an external E-field undergo a dipole polarization $\mathbf{P_i}$ equal to:

$$\mathbf{P_i} = \boldsymbol{\alpha_i} \cdot \mathbf{E_{loc}}(\mathbf{r_i}) \tag{9}$$

Where $\boldsymbol{\alpha_i}$ is a material dependent property known as the polarizability tensor and $\mathbf{E_{loc}(r_i)}$ is the instantaneous local electric field at $\mathbf{r_i}$ given by:

$$\mathbf{E_{loc}}(\mathbf{r_i}) = \mathbf{E_o e^{ik \cdot r_i}} - \sum_{\mathbf{j \neq i}} \mathbf{A_{ij}} \cdot \mathbf{P_j} \tag{10}$$

On the right hand side, the first term represents the electric field induced by the incident wave at the dipole at $\mathbf{r_i}$ and the second term sums the induced field at $\mathbf{r_i}$ by all neighboring dipoles. DDScat computes $\mathbf{P_j}$ which satisfies a system of 3N linear equations given by:

$$\mathbf{A'} \cdot \mathbf{P} = \mathbf{E} \tag{11}$$

For a system with **N** total dipoles, **E** and **P** are 3**N** dimensional vectors, and **A′** is a 3**N** x 3**N** matrix. Solving this set of 3**N** complex linear equations, the polarizations $\mathbf{P_j}$ are determined, and from this can be determined the scattering, absorption and extinction.[100]

CHAPTER 3

NANOMATERIAL CHARACTERIZATION TECHNIQUES

3.1 Introduction

The observations and conclusions derived from data is essential for gaining the full understanding and appreciation of mechanistic insights described in Chapter's **4 - 9**. Therefore, a brief discussion of the working principles will be discussed along with example data and analysis. The techniques discussed include UV-Vis-NIR Spectroscopy, atomic force microscopy (AFM), scanning electron microscopy (SEM), transmission electron microscopy (TEM), X-ray diffraction (XRD), and selected area electron diffraction (SAED).

3.2 UV-Vis-NIR Spectroscopy

The optical properties of the nanomaterials can be used to deduce information about their structure and morphology. Visible spectroscopy provides the easiest way to monitor real time changes over time, an advantage not (*yet*) readily accessible via electron microscopy. Presented on the next page are three steps which summarize how a sample is characterized using UV/Vis spectroscopy. First, nanoparticles are synthesized on a transparent substrate (i.e. SiO_2, Al_2O_3, MgO, etc.). The sample is then mounted into the UV/Vis spectrometer such that the beam penetrates the sample normal to the surface. The spectrometer measures an absorbance spectrum which can be correlated to the physical aspects of the nanoparticles including nanoparticle size, shape, composition, structure (i.e. hollow, porous), substrate (or support), electron density, surface chemistry, dielectric environment, temperature and external fields.

Step 1: Sample Preparation, Electron Microscopy, Analysis

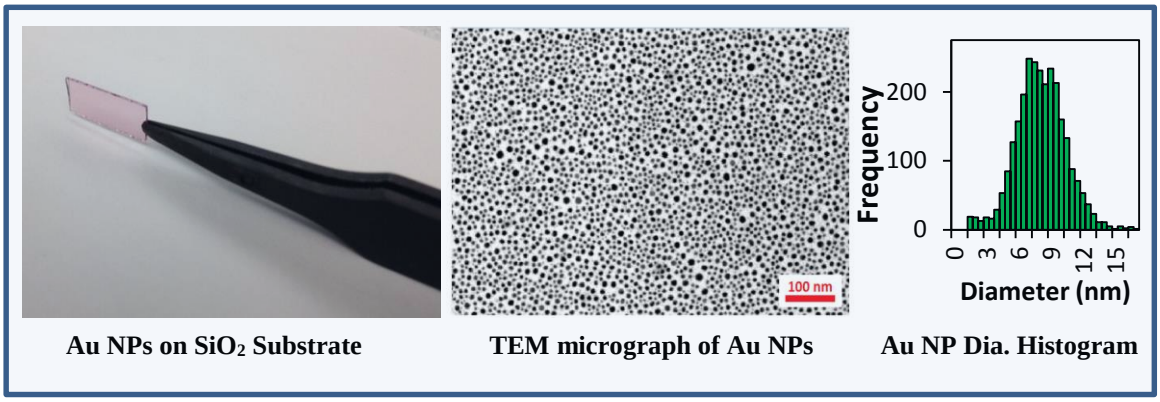

Au NPs on SiO_2 Substrate | TEM micrograph of Au NPs | Au NP Dia. Histogram

Step 2: Optical Characterization: UV/Vis Spectroscopy and Extinction

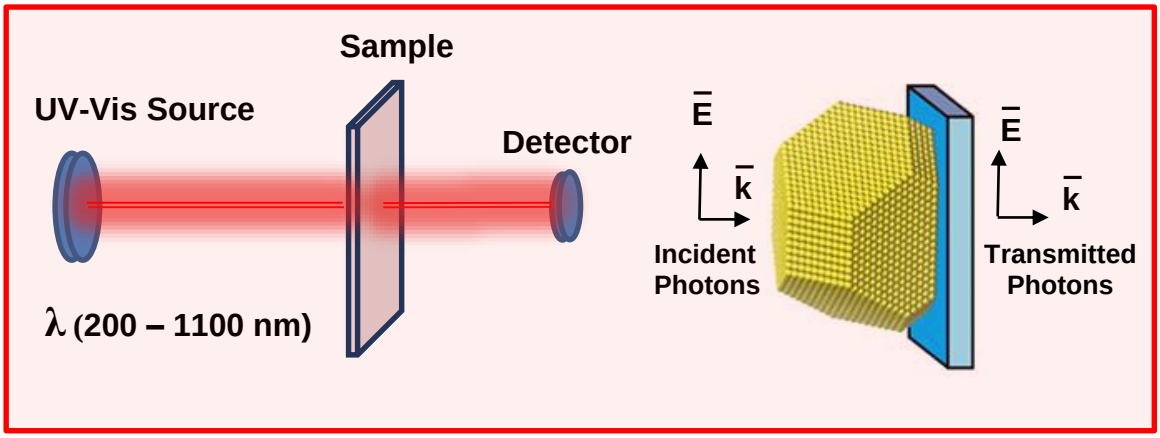

Step 3: Interpretation and Analysis of the Absorbance Spectrum

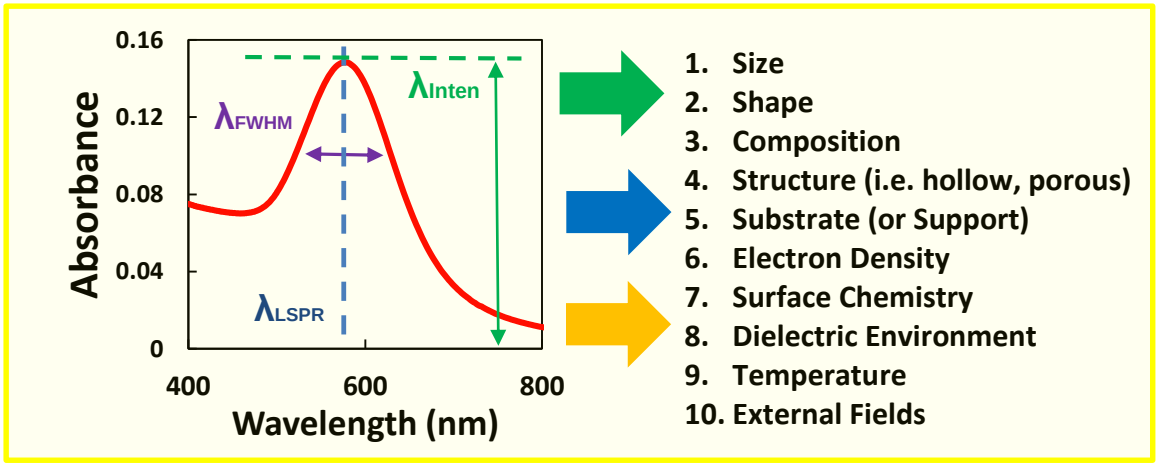

3.3 Atomic Force Microscopy

Atomic force microscopy (AFM) is a technique used to measure the nanoscale topography of surfaces.[101] It involves a sharp tip (with radius typically less than a few nm) attached to the end of a microsized cantilever oscillating at or near resonance. A laser is directed at the back of the cantilever, reflected and then detected by a position sensitivity photodetector (PSPD) **(Figure 3.1a)**. As the probe rasters over a selected area (**Figure 3.1b**), deflections in the cantilever induced by nanoscaled features are detected and interpreted by the software to construct an image. A simple feedback loop is used to keep the height of the tip a safe distance above the sample. It is important to note that the x-direction data (i.e. in-plane distances) are less reliable due to convolutions brought about by the morphology of the tip. A sample 3D-image is shown in **Figure 3.1c** where thermally assembled Au NPs on sapphire are scanned.

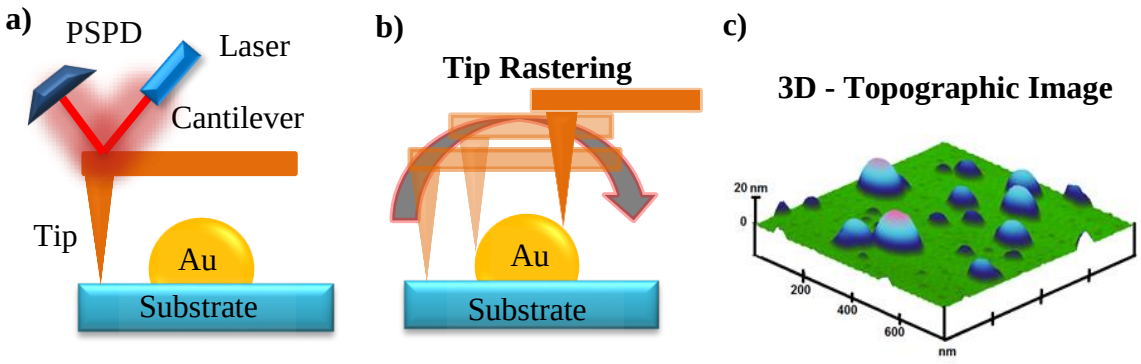

Figure 3.1 a) The laser is directed at the back of the cantilever, reflected and then detected by a photodetector (PSPD). b) As the tip rasters the surface, the deflection of the cantilever is detected by the laser and which is used to construct a height image. c) A 3D-image captured using AFM showing self-assembled Au nanoparticles on Al_2O_3.

3.4 Electron Microscopy

Optical microscopy becomes physically limited when attempting to characterize materials having subwavelength sizes. This limitation is known as the Abbe diffraction limit.[102] In the mid 1800's, Abbe determined that the resolution of an optical microscope is directly proportional to the incident wavelength and inversely proportional to the numerical aperture,[103] where the spatial resolution can be defined by[105]:

$$\mathbf{d} = \frac{\boldsymbol{\lambda}}{\mathbf{2nsin\theta}} \qquad \textbf{(12)}$$

Where λ is the wavelength of the radiation used to image the object, $\mathbf{nsin\theta}$ is a numerical aperture of the lens ($\mathbf{nsin\theta} \approx 1$).[104] Since visible light is in the range of 400 – 800 nm, the best spatial resolution possible is ~150 nm. Since nanomaterials have at least one dimension of their morphology under 100 nm, optical microscopy is ineffective.

The hallmark of electron microscopy is that the wavelength of the incident electrons can be made roughly six orders of magnitude shorter than visible light. The wavelength of an electron can be determined by equating the kinetic and potential energy terms:

$$\frac{\mathbf{1}}{\mathbf{2}}\mathbf{m_o v^2} = \mathbf{eV} \qquad \textbf{(13)}$$

Where $\mathbf{m_o}$ and **v** are the rest mass and velocity of the electron, respectively. On the right hand side, **e** and **V** represent the charge and voltage on the electron. Since the above equation can be rearranged such that momentum can be known, the de Broglie relation (pλ = h) can be used to determine the wavelength of the electron. Taken all together, including relativistic effects, the wavelength of the electron can determined by solving[105]:

$$\boldsymbol{\lambda_e} = \sqrt{\frac{\mathbf{h^2}}{\left[\mathbf{2m_o eV}\left(\mathbf{1} + \frac{\mathbf{eV}}{\mathbf{2m_o c^2}}\right)\right]}} \qquad \textbf{(14)}$$

Where **h** is Planck's constant and **c** is the speed of light. **Table 3.1** provides a series of accelerating voltages with corresponding wavelengths, velocities and resolutions.

Table 3.1 Electron Properties and Resolution as a Function of Accelerating Voltage

Accelerating Voltage (kV)	Relativistic Wavelength (pm)	Velocity (x 10^8) (m/s)	Theoretical Resolution† (nm)
100	3.68	1.64	0.45
200	2.73	2.09	0.33
300	2.23	2.33	0.27
400	1.93	2.48	0.24
1000	1.22	2.82	0.15

† *Resolution values are based on the formula in ref 105 where* $d = 1.22 \lambda_e/\beta$. *Values are obtained without corrections to the various forms of aberrations and for the upper limit value of* $\beta = 10$ *mrads.*

3.4.1 Scanning Electron Microscopy

When the incident beam of electrons interacts with a sample, three varieties of electrons (scattered and/or emitted) including: (i) secondary electrons (inelastically scattered) with energies < 50 eV, (ii) backscattered electrons (elastically scattered), which have energies similar to those of the incident electrons and (iii) Auger electrons, with very low energies, which are emitted by the decay of excited atoms.[105] The secondary electrons, used primarily for topographical imaging, are captured by a detector which is located to the side of the sample chamber (**Figure 3.2**). Backscattered electrons, used for elemental-contrast (*or Z - contrast*), are collected by a detector located directly above the sample.[106]

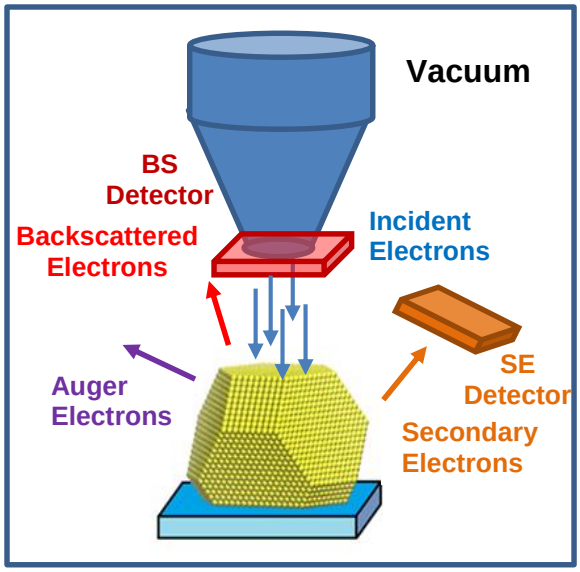

Figure 3.2 A schematic showing the interaction of incident electrons with a nanostructure and the resulting electron types for SEM.

3.4.2 Transmission Electron Microscopy

As discussed previously, SEM captures secondary and backscattered electrons to create an image. It turns out that the resolution of SEM is limited by the 30 kV voltages used. Higher resolution can be attained via transmission electron microscope capable of accelerating voltages of up to 300 kV shortening the electron wavelength a factor of 10^5 - 10^6 compared to visible light[107] with λ_e = 2.51 pm and $v_e = 2.086 \times 10^8$ m/s.[105] The resolution, d, of the TEM is defined by λ_e, the electron wavelength, and β, the semi-angle of collection of the magnifying lens.[105]

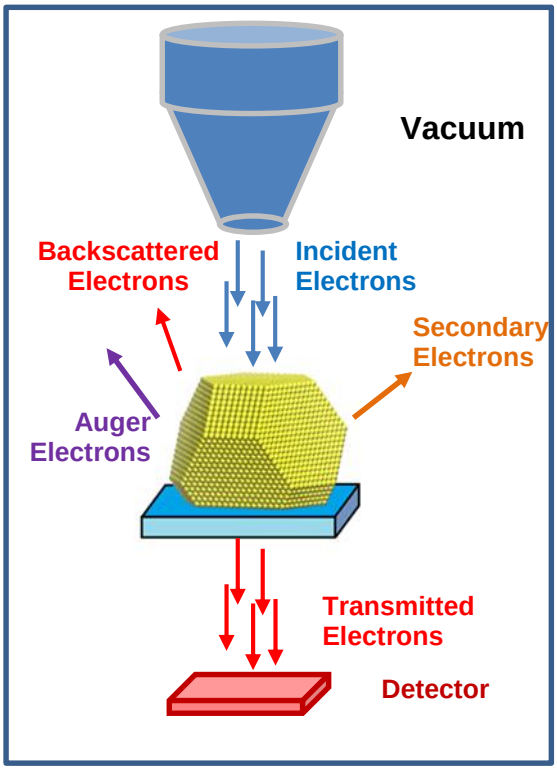

Figure 3.3 Schematic of the working principle. The electrons are sent through the sample and collected by the detector directly beneath the sample area.

$$\mathbf{d} = \frac{\mathbf{1.22}\lambda_e}{\boldsymbol{\beta}} \qquad \textbf{(15)}$$

The semiangle **β**, can be approximated to 10 mrads which is an upper limit for TEM's.[105] As shown in **Figure 3.3**, the detector for the TEM is located directly beneath the sample where transmitted/scattered electrons are collected. Areas of the sample which are thicker or comprised of material with a higher Z appear darker. The primary drawback of TEM stems from the fact that the sample must be extremely thin and dispersed on a TEM grid. The grid, which has windows with thicknesses < 100 nm, can be made of variety of materials, the most popular being carbon, TiO_x and Si_3N_4. Sample preparation for nanomaterials made in solution involves drop casting directly onto the TEM grid.

3.5 X - Ray Diffraction

X-ray diffraction (XRD) is a technique used to measure the distance between planes in crystals. Common to X-ray diffractometers are X-rays sourced by a Cu K-alpha emission having energies of 8.1 keV and wavelengths of 1.54 Å. When coherent monochromatic X-rays interact with the lattice of a given crystal, an Edwald sphere is produced around the sample. This sphere consists of X-rays interfering with one another both constructively and destructively. Constructive interference occurs when Braggs equation is satisfied:

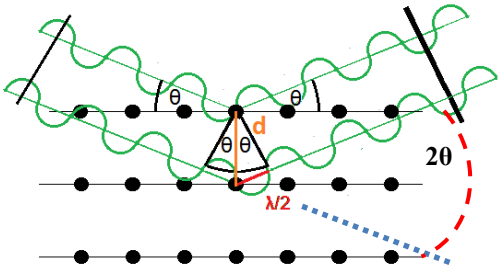

Figure 3.4 The interaction between incident X-rays (green) and a crystal lattice (black dots).

$$\mathbf{n\lambda = 2dsin\theta} \qquad \textbf{(16)}$$

Where **n** is a positive integer, **λ** is the wavelength of incident X-ray, **d** is the spacing between a given plane and **θ** is the Bragg angle. The spacing between atomic planes can be deduced provided several parameters are known including (1) the angle of incidence, (2) the spatial aspects of the diffraction sphere and (3) the wavelength of the X-rays. The technique utilized throughout this dissertation is known as theta-2theta or (θ - 2θ), which detects X-ray intensity (at a known distance from the sample) as a function of 2θ, (**Figure 3.4)**. In order to solve for the d-spacing based on experimentally measured 2θ values, a general expression for d-spacing as a function of 2θ can be solved for. This can be done by inserting expressions for d-spacing into Braggs equation (eq 16).

For a cubic system, the distance between parallel-planes can be represented by (**Figure 3.5**):

$$\frac{1}{d^2} = \frac{h^2 + k^2 + l^2}{a^2} \qquad (17)$$

where the indexes (h k l) represent the Miller indices of the Bragg plane and '**a**' is the lattice constant and d is the distance between planes. By simply isolating d from the above equation and substituting into Braggs equation, one can arrive at the value for 2θ:

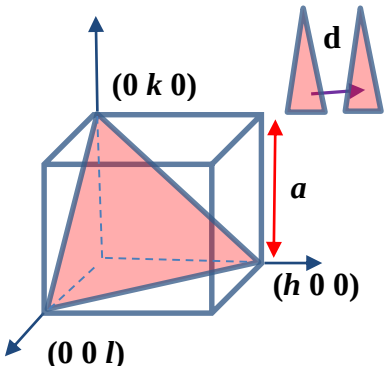

Figure 3.5 The cubic cell with Miller indices (**h k l**), lattice constant '**a**' and distance between planes 'd' identified.

$$2\theta_{(h\,k\,l)} = 2\lambda \sin^{-1}\sqrt{\frac{(h^2 + k^2 + l^2)}{4a^2}} \qquad (18)$$

Since all parameters are known from the above equation, theoretical $2\theta_{(h\,k\,l)}$ values can be evaluated for the materials of interest, as shown in **Figure 3.6**.

Element (lattice constant, Å)[108]	$2\theta_{(111)}$ (°)	$2\theta_{(200)}$ (°)	$2\theta_{(220)}$ (°)	$2\theta_{(311)}$ (°)
Ni (a = 3.499)	44.81	52.23	76.99	93.75
Cu (a = 3.597)	43.53	50.7	74.53	90.47
Pd (a = 3.859)	40.44	47.04	68.72	82.87
Ag (a = 4.079)	38.17	44.36	64.54	77.53
Pt (a = 3.912)	39.87	46.37	67.66	81.51
Au (a = 4.065)	38.31	44.53	64.79	77.84

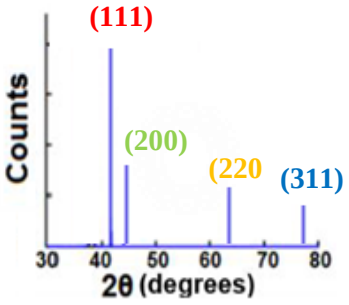

Figure 3.6 A Table containing the theoretical $2\theta_{(h\,k\,l)}$ values for Ni, Cu, Pd, Ag, Pt and Au. The figure to the right shows a typical graph for a θ - 2θ measurement.

Two examples where θ-2θ spectra were collected are presented in **Figure 3.7**. The first example (**Figure 3.7a**) is a θ-2θ spectrum of thermally assembled gold nanoparticles epitaxially aligned on (0001)-sapphire. The epitaxial alignment arranges all gold nanoparticles such that a Au(111)-plane is parallel to the (0001)-sapphire surface. Since

the θ-2θ technique only measures atomic periodicities which are parallel to the surface, only two peaks are expected in the 2θ range 30 - 80°; one from the Au(111) at 2θ = 38.2° and another from the sapphire (0006) at 2θ = 42.8°. In the second example, **Figure 3.7a**, a θ-2θ spectrum of gold assembled on sapphire which does not have epitaxial alignment. Apparent now is the presence of multiple peaks corresponding to orientations other than Au(111). The relative peak intensities can be used to determine the relative distribution of orientations corresponding to Au(111), Au(100) and Au(110).

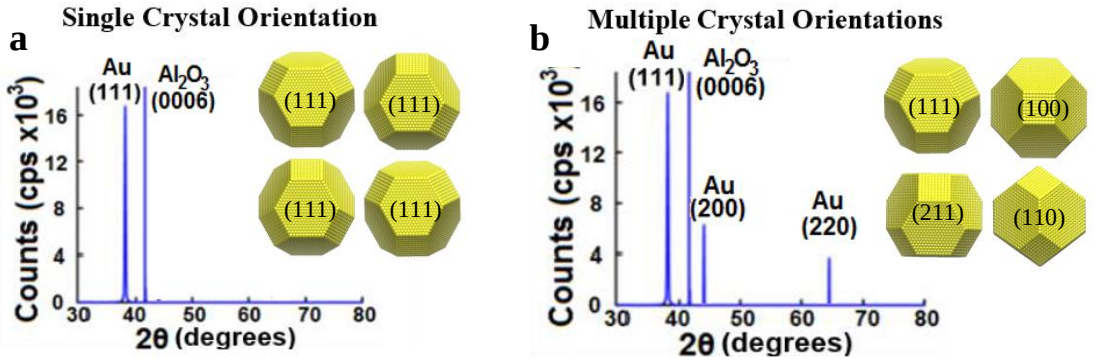

Figure 3.7 a) An XRD spectrum from epitaxially aligned Au on (0001)-sapphire. b) An XRD spectrum from a sample grown on (0001)-sapphire with multiple crystal orientations.

3.6 Selected Area Electron Diffraction

Selected area electron diffraction (SAED) is a measurement technique built directly into the transmission electron microscope. It involves (1) an electron diffraction aperture, (2) a viewing screen (typically placed ~ 20 – 40 cm beneath the sample) and (3) accelerated electrons. In principle, SAED is very similar to X-ray diffraction but where electrons are diffracted instead of X-rays. Physically, the only difference is that the incident wavelength is shorter (1.54 Å for X-rays and 3.35 pm for electrons at 120 kV) which gives rise to different Bragg angles according to eq. 18. The primary advantage of SAED over X-ray diffraction is the ability to obtain diffraction patterns of individual nanostructures. SAED

analysis can reveal whether an individual nanostructure is polycrystalline, single-crystalline or amorphous.

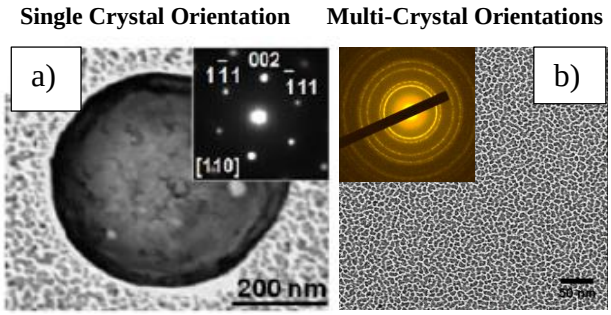

Figure 3.8 a) The TEM micrograph shows a AuAg hollow nanoshell. The inset shows the single crystal SAED pattern obtained for the nanoshell. B) The TEM micrograph shows the morphological features of a 3 nm Cu thin film. The inset shows the diffraction ring pattern generated from SAED.

Two examples are shown in **Figure 3.8**, where a) demonstrates a single crystal pattern and b) shows a polycrystalline sample. In example a), shown is an electron diffraction pattern for a [110]-oriented single crystal AuAg nanoshell. This pattern consists of an array of discrete dots indicating the presence of {111} and {200}–planes. This pattern allows for determining a number of physical properties about the sample including (i) crystal structure, (ii) compressive or tensile strain, (iii) crystal orientation and (iv) identifying the presence of defects such as stacking faults or twinning.

In the second example, **Figure 3.8b**, a diffraction ring pattern is shown for that of a polycrystalline copper thin-film. Since the film consists of crystallites of multiple orientations relative to the electron-beam, a superposition of all orientations (or dot patterns) is observed. This pattern reveals information regarding (i) average crystal structure, (ii) average crystal orientation and (iii) information about tensile or compressive strain. **Figure 3.9** contains a table and example ring pattern for Ni, Cu, Pd, Ag, Pt and Au along with simulated diffraction rings for a polycrystalline FCC sample.

Element (lattice constant, Å)[108]	(111)	(200)	(220)	(311)
Ni (a = 3.499)	2.02	1.75	1.24	1.05
Cu (a = 3.597)	2.08	1.80	1.27	1.08
Pd (a = 3.859)	2.23	1.93	1.36	1.16
Ag (a = 4.079)	2.36	2.04	1.44	1.23
Pt (a = 3.912)	2.26	1.96	1.38	1.18
Au (a = 4.065)	2.35	2.03	1.44	1.23

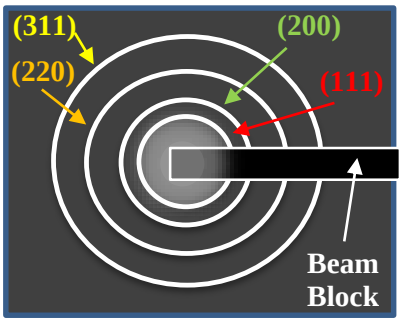

Figure 3.9 A table with tabulated values for the theoretical d-spacings of Ni, Cu, Pd, Ag, Pt. The theoretical ring pattern to the right represents a typical output for a polycrystalline FCC metal.

CHAPTER 4

THE SYNTHESIS AND OPTICAL PROPERTIES OF AuAg NANOHUTS

4.1 Introduction and Motivation

Progress directed toward the application of noble metal nanostructures[109-112] has been reliant on the establishment of facile synthetic protocols[113] able to tailor the plasmonic response to meet the demands of specific applications. Breakthroughs have increasingly relied on synthetic strategies yielding complex geometries with asymmetric, core shell or hollowed morphologies.[114] In this regard, galvanic replacement reactions[115] offer pathways toward the formation of intricate nanostructures using synthetically simple reactions where complex products are derived from preformed templates. These reactions are reliant on solution-based oxidation–reduction reactions which occur when atoms of a solid metal (i.e., the template) spontaneously react with ions of a second metal having a higher electrochemical potential. The ensuing reaction results in the simultaneous heteroepitaxial deposition of the second metal onto the template as the template material is steadily dissolved into the solution. With both deposition and dissolution being highly dependent upon the crystallographic orientation and faceting of the template, complex nanostructures can be engineered through the use of appropriate templates which are reacted to the desired endpoint. Such reactions typically lead to the formation of hollow nanoshells which exhibit highly tunable plasmonic properties due to coupling between plasmons formed on the inner and outer surfaces of the structure. Also of significance is the strong sensitivity of the position of the localized surface plasmon resonance (LSPR) to changes in the index of refraction of the adjacent medium.[116] Together these properties make nanoshells candidate materials for use in biomedical[117], sensor[118] and catalytic applications[119]. Galvanic

replacement reactions have been extensively studied for the case of template structures dispersed in solution. Few investigations, however, have been carried out on substrate-immobilized templates. Notable studies include the use of replacement reactions for: (i) the deposition of nanostructured gold on nickel electrodes for mercury vapor sensing[120], (ii) the preparation of nanoporous copper surfaces on nickel foils for catalytic applications[121], (iii) the formation of chemically stable surface enhanced Raman spectroscopy (SERS) active surfaces on glass substrates though the replacement of vertically aligned silver nanorods with gold[122], (iv) the replacement of electrochemically synthesized iron nanocubes on carbon with gold and palladium[123], and (v) the epitaxial growth of smooth copper films on (111)- oriented single crystals of gold and silver using sacrificial lead films as a template material[124]. While these studies have demonstrated the viability of substrate-based galvanic replacement reactions, they have not fully taken advantage of unique capabilities accessible through the use of nanostructured templates. Specific advantages include the placement of templates at site-specific locations and having them heteroepitaxially aligned with the underlying substrate. Fully exploiting these capabilities could result in the synthesis of substrate-based periodic arrays of aligned crystalline nanostructures with a high degree of complexity, tunability and functionality. Here, we report on the galvanic replacement of heteroepitaxially aligned nanostructured silver templates formed on (0001)-oriented sapphire substrates. Reported is the synthesis and characterization of substrate immobilized Au–Ag nanohut structures formed as both periodic arrays and as structures with randomized size and placement.

4.2 Fabrication of Periodic Arrays of AuAg Nanoshells

Galvanic replacement reactions (**Figure 4.1**) on the silver template structures were carried out using a synthetic protocol similar to that devised by Xia and co-workers.[74] Briefly, a three neck flask was filled with an aqueous $HAuCl_4$ solution (10 mL) and refluxed for 10 min. The concentration for the larger templates (dia. < 250 nm) was varied from 10 to 100 μM for both the arrayed and non-arrayed configurations (**Figure 4.1 c, d**). For smaller templates (dia. < 50 nm), lower concentrations were used (0.5 μM – 2 μM) since five times less silver was deposited on the substrate surface. The substrate was then immersed into the $HAuCl_4$ solution for 10 min (**Figure 4.1 e**), after which it was slowly pulled out and dried in a flow of argon gas. It is noted that the exposure of the silver template structures to air was minimized either by reacting them immediately following assembly or storing them in a $1x10^{-6}$ torr vacuum environment.

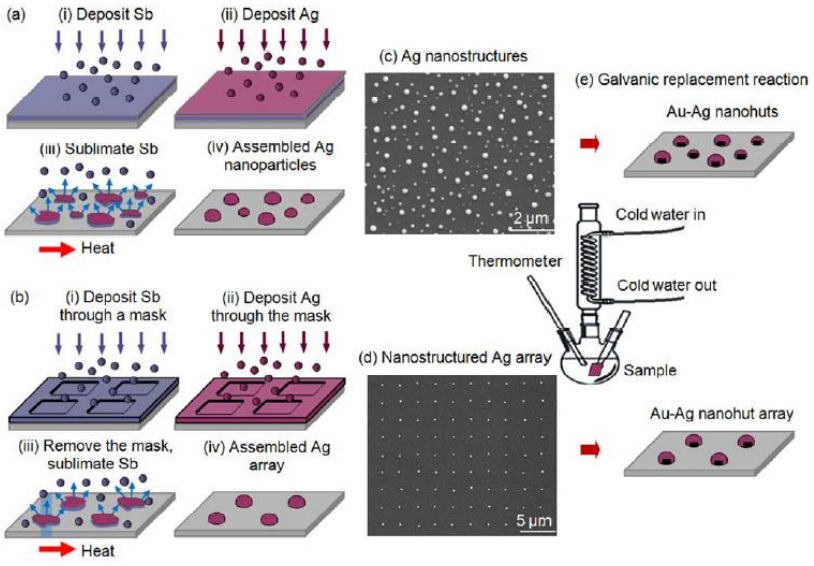

Figure 4.1 Schematics showing the synthetic routes used to assemble (a) non-arrayed and (b) arrayed silver nanostructures. The SEM images show structures with (c) a substantial size distribution situated at random locations and (d) arrayed structures with a narrow size distribution. Both structures were used as templates in (e) galvanic reactions yielding immobilized Au-Ag nanohuts. Figure taken from reference 125 and reproduced by permission of The Royal Society of Chemistry.

4.3 Morphological Characterization

Tilted SEM micrographs of the Ag templates exposed to two different concentrations of $HAuCl_4$, 10 and 100 μM, on random and arrayed Ag templates (**Figure 4.2 a, b**). Throughout the reaction the structures become increasingly hollow and rough. **Figure 4.2 c** shows the hollow structures upside down in a nanobowl configuration, using scotch tape to flip them upside down. Substrate alignment markers makes it possible to measure the height of an individual template structure using an atomic force microscope (AFM), react the template and then return to the identical location to measure the height of the nanohut formed (**Figure 4.2 f**). The composition of the reacted structure was then measured using energy dispersive spectroscopy (EDS). The AFM cross-sections are provided for a structure which has undergone 75% replacement. The height of the structure increased by 17%, a value somewhat larger than the 12.4% value derived for the expected growth mode which sees a hollowing of the template as gold is deposited uniformly on its outer surface in a 3:1 Ag:Au replacement ratio.[73,74]

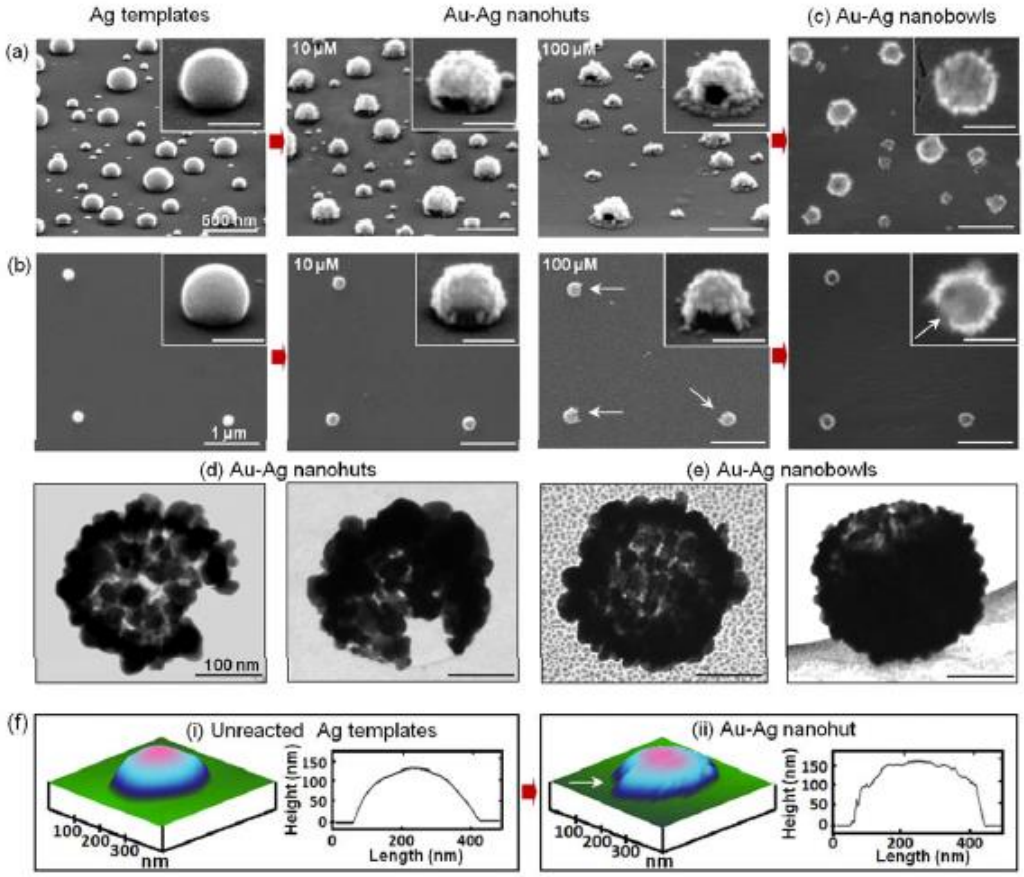

Figure 4.2 SEM images showing the morphology of unreacted templates and nanohuts formed through galvanic replacement reactions using 10 and 100 μM solutions in the (a) non-arrayed and (b) arrayed configurations. (c) Images of non-arrayed and arrayed nanohut structures which have been removed from the sapphire substrate using Scotch tape. The scale bar for all insets is 200 nm and the tilt angle is 65°. (d) Top- and tilted-view TEM images of nanohuts assembled directly on Si3N4 support films. (e) Top- and titled-view TEM images of nanobowls removed from sapphire substrates. (f) AFM image and the associated cross-section for an individual template and the same structure after it has been 75% reacted to form a nanohut. The white arrows on both the SEM and AFM images point toward the single side opening found on each nanohut. Figure taken from reference 125.

4.4 Optical Properties of AuAg Nanohuts

Simulations using the discrete dipole approximation (DDA)[126] were carried out to examine the influence of both the opening and substrate on the nanohut extinction spectra. **Figure 4.3** shows the spectra for free-standing gold structures with and without side openings and those same structures supported by a sapphire substrate. Transverse ***E***-fields

in the absence of a side opening give rise to a polarization independent response yielding a LSPR peak at 586 nm for the freestanding structure (**Figure 4.3a**). The break in symmetry resulting from the introduction of a side opening into this structure results in a strong polarization dependence with ***E***-fields through and parallel to the opening yielding resonances at 573 and 655 nm, respectively (**Figure 4.3c**). It is noted that this behavior is qualitatively similar to the simulated and experimental results obtained for semishells with a perforation which intersects the edge of the shell.[127] The inclusion of a supporting substrate into the simulation (**Figure 4.3b,d**) leads to a strong red-shift in the LSPR peaks and the establishment of a high energy quadrupolar mode. With red-shifts of 52 and 100 nm for ***E***-fields through and parallel to the side opening, the substrate acts to substantially increase the degree of optical anisotropy. Because the fabricated nanohuts used in the current study had side openings in numerous directions, direct comparisons between simulation and experiment remain challenging. However, upon recognizing that the experimental data is an average over all transverse polarizations, the simulations are consistent with the large red-shift and substantial broadening in the LSPR peak observed for the fully reacted structures.

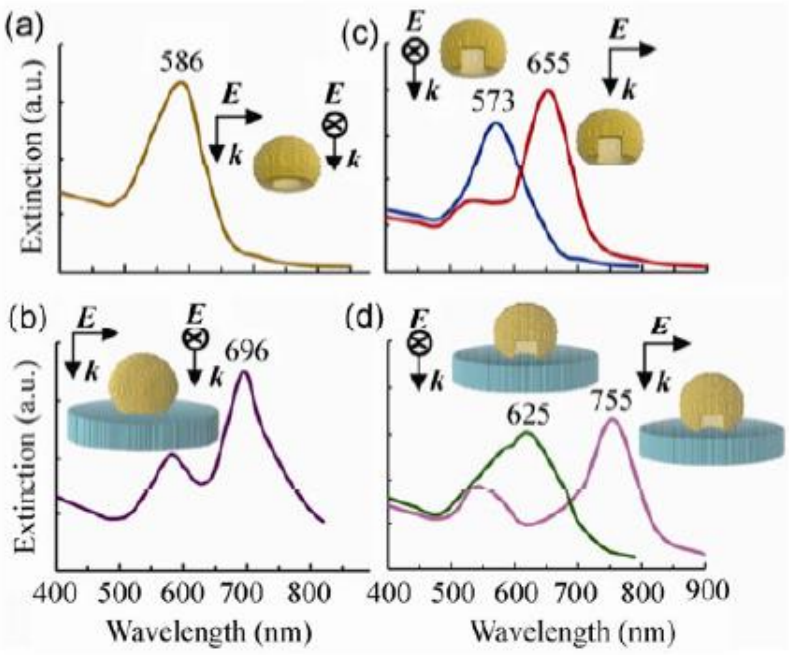

Figure 4.3. Calculated extinction spectra of (a) a hollow gold shell and the same shell (b) resting on a sapphire substrate, (c) with a rectangular side opening and (d) resting on a substrate and having rectangular side opening. The shell is a truncated sphere (diameter = 40 nm, shell thickness = 5 nm) which forms a 130° contact angle with the substrate. The side opening is 10 nm in the vertical direction and 14 nm in the horizontal direction. The substrate has a diameter of 80 nm and thickness of 15 nm. The incident light is transversely polarized (i.e., the ***E***-field is parallel to the substrate). For the nanohut geometry, spectra are calculated using transverse ***E***-fields that are both through and parallel to the side opening. Figure taken from reference 125.

Figure 4.4 shows the extinction spectra for nonarrayed silver templates with an average diameter of 30 nm reacted to varying degrees. The measurements were taken using unpolarized light where the ***E***-field and propagation direction (***k***) are parallel and perpendicular to the substrate surface, respectively. Observed is a substantial broadening of the LSPR peak as it red-shifts from 436 nm for the non-reacted templates to 745 nm for the fully reacted structures. The accompanying color change observed in reflectance is shown in the inset to **Figure 4.4** This ability to tune the plasmonic response over such a large range starting from identical templates is one of the key advantages of galvanic replacement reactions. Of significance is the fact that the nanohut is a highly asymmetric

due to both its hemispherical-like geometry and the presence of the rectangular opening at its base. This places the nanohut in a class of symmetry breaking structures (e.g., semishells, nanobowls, and nanocrescents) which offer polarization dependent plasmon modes with large local field enhancements and a high degree of tunability.

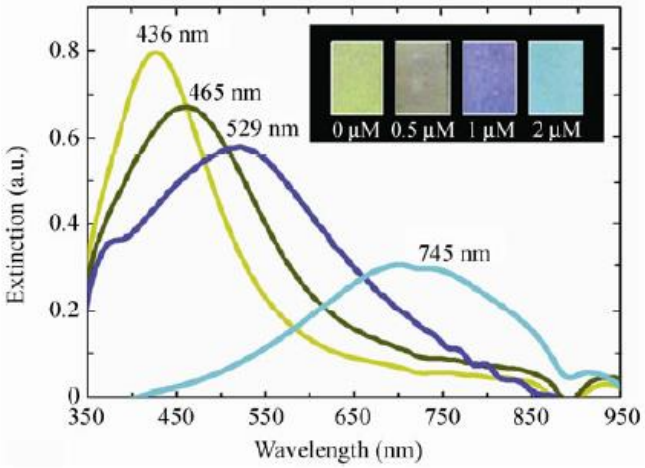

Figure 4.4 The extinction spectra for non-arrayed silver templates with an average particle size of 30 nm exposed to various $HAuCl_4$ concentrations. Concentrations of 0, 0.5, 1 and 2 μM yield LSPR peaks at 436, 465, 529 and 745 nm, respectively. The inset shows optical images of the samples taken in reflectance. Figure taken from reference 125.

4.5 Conclusions

Substrate-based galvanic replacement reactions carried out on heteroepitaxially formed silver templates have yielded hollow Au–Ag nanoshells. The resulting nanohut geometry is characterized by a downward facing shell with a single rectangular opening at its base. The structures are immobilized, can be placed at site-specific locations and have a LSPR peak which can be tuned to a particular frequency by varying the degree of replacement. The work not only demonstrates the fabrication of these unique structures, but also points toward future opportunities in terms of engineering intricately shaped nanostructures using the combined capabilities of heteroepitaxial techniques and galvanic replacement reactions.

CHAPTER 5

MECHANISTIC STUDIES OF GALVANIC REPLACEMENT

5.1 Introduction and Motivation

In the studies carried out in Chapter 4, the roughness of the AuAg shell was attributed to the generation of vacancies and defects during the galvanic replacement reaction. Therefore, in order to verify this claim and to prevent roughening of the surface, an Au passivation layer is used to divert the dissolution of Ag^+ away from the top. This is achieved simply by sputter coating the outer surface of the sacrificial Ag template with a 3 nm layer of Au prior to reaction. In contrast to the porous, rough nanoshells derived from the uncoated template, the Au layer leads to the formation of hollow Au–Ag nanoshells which are smooth, robust and crystalline exhibiting well-defined geometric openings. The drastic difference in morphology can be observed in **Figure 5.1 a-d**, where AuAg nanoshells are shown with and without the use of surface passivation layers. These differences are attributed to the passivation of the highly reactive surface of the Ag template by the Au layer.

In the absence of this passivating layer, the surface topography of the emerging nanoshell is dramatically altered by the highly reactive nature of curved surfaces of the sacrificial template. This gives rise to a nanoshell with a weak structural framework that is unable to withstand the destabilizing influences of dealloying and thermal diffusion processes. Surface passivation prevents these destabilizing influences, allowing for the orderly dissolution of the template from a single pit at its base. Unique to these studies is the observation that the hollowing initiates in a <110> direction and proceeds first through

the rapid dissolution of a single channel across the entire extent of the template followed by the removal of the remaining Ag.

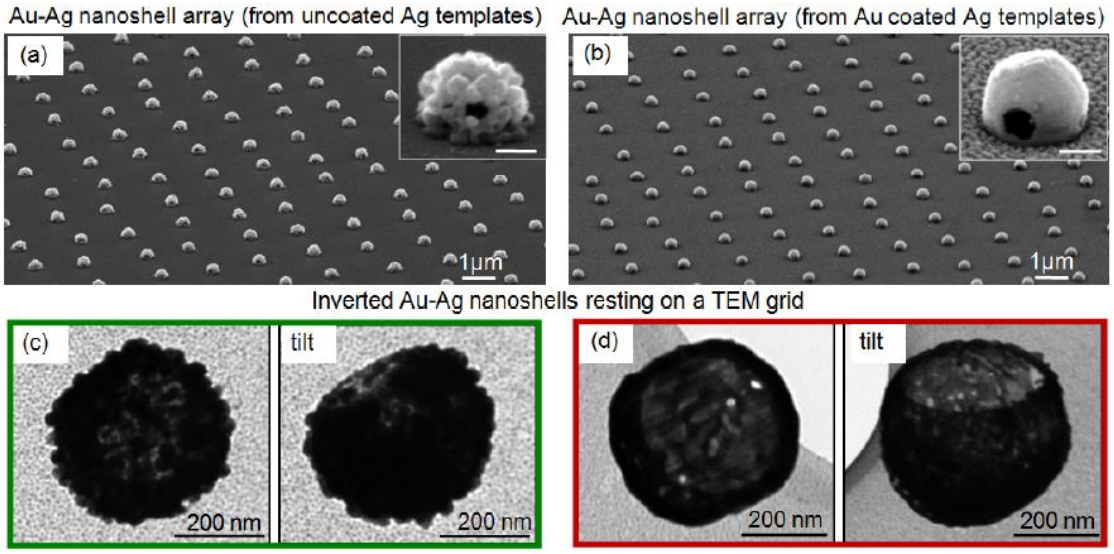

Figure 5.1 A 65° tilted-view SEM images of a nanoshell array produced using galvanic replacement reactions on (a) silver templates and (b) silver templates coated with 3 nm of Au. The insets show a high magnification view of an individual nanoshell. Top- and tilted-view TEM images of inverted nanoshells obtained from silver templates having the (c) uncoated and (d) Au-coated configurations. Figure taken from reference 128.

This observation is attributed to the combined influences of atoms in {110}-surfaces having low coordination, the Au^{3+}-poor environment within the interior of the hollowing shell and a reaction that proceeds through the transfer of electrons from an inner shell anode to an outer shell cathode. The final stages of the reaction lead to the formation of openings in the <111>-directions where each template orientation relative to the underlying substrate yields a unique nanocage geometry.[128]

5.2 Early and Late Stage GR

The early stages of the reaction result in the preferential deposition of Au onto the high curvature surfaces where facets intersect. This in combination with a slower rate of deposition onto the {100} and {111} facets exaggerates the underlying crystallography of the substrate-truncated cuboctahedron (**Figure 5.2**). Noteworthy is the fact that the resulting framework is disconnected at numerous locations. As the reaction proceeds the framework becomes increasingly rough, developing lobes while the facets of the structure remain smooth (**Figure 5.2 a - d**). As the lobes continue to become more pronounced, prominent openings emerge in the structure. While somewhat obscured by the lobes, an examination of a large number of structures makes it apparent that the openings consistently form at the facet positions of the initial Ag template, a behavior consistent with the dealloying process. Reactions allowed to proceed further result in structures where the pattern of openings is further obscured by an increase in the overall porosity and the continued development of lobes. The progression for galvanic replacement reactions carried out on Au-coated silver templates is markedly different. **Figures 5.2 e – h** show this progression for nanoshells derived from [111]-oriented

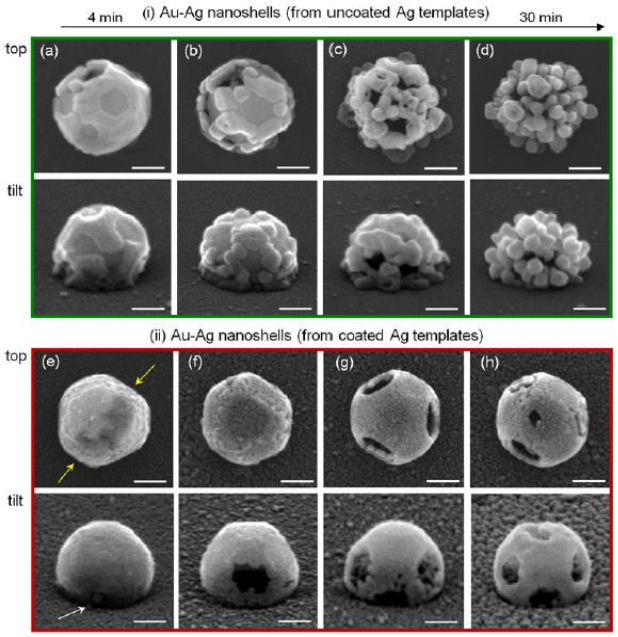

Figure 5.2 Top- and 65° tilted-view SEM images showing the evolution of (i) silver templates and (ii) silver templates coated with 3 nm of Au as they undergo galvanic replacement reactions for time intervals ranging from 4 to 30 min. It should be noted that the darker contrast in the top-view SEM image shown in (e) reveals the existence of a hollow channel within the structure (denoted by yellow arrows). Figure taken from reference 128.

templates. The early stage morphology of the nanoshell derived from the Au coated template is characterized by an exceedingly smooth shell with a small pinhole near the base of the structure (denoted by the white arrow) and a single hollow channel extending from one side of the template to the other (denoted by yellow arrows). Such channels are consistently observed for templates that are not fully reacted. The fact that many of the channels in adjacent structures are parallel to each other suggests a correlation between the channel direction and the underlying crystal structure of the silver template. In striking contrast to the structures derived from uncoated templates, those utilizing Au-coated silver templates do not undergo a rapid deterioration in their morphology for longer reaction times. Instead, the Au deposition occurs in a far more uniform manner over the entire template, showing only a slight preference for deposition on {100} facets and along the curved regions where the facets meet (**Figure 5.2 f**). At this point the structure has also

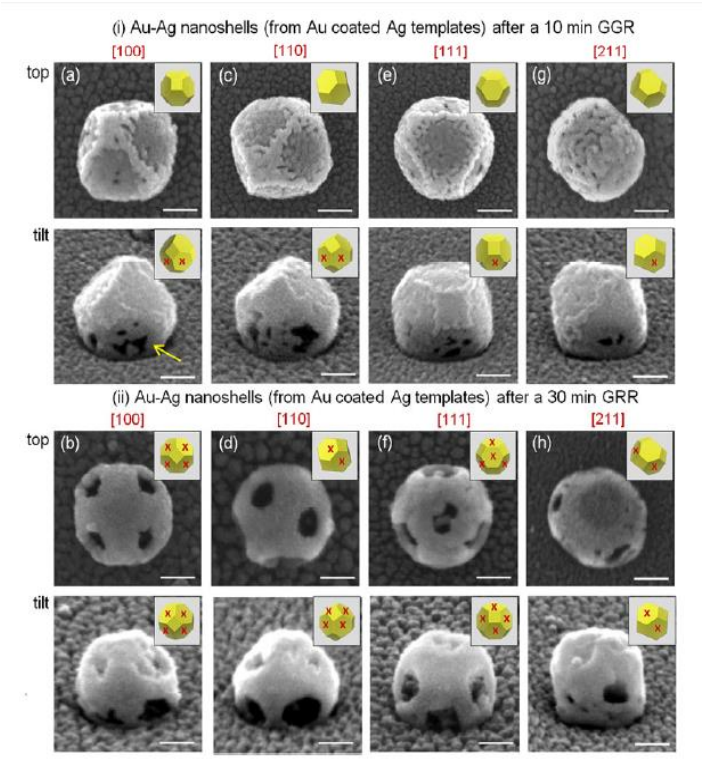

Figure 5.3 Top- and 65° tilted-view SEM images showing the evolution of Au passivated structures from Au–Ag (i) nanoshells to (ii) nanocages. This dealloying process is shown for structures derived from Au coated silver templates having a (a) and (b) [100]-, (c) and (d) [110]-, (e) and (f) [111]-, and (g) and (h) [211]-orientation. Note that each orientation gives rise to a unique nanocage geometry. The insets to the figures show schematics of top- and side-view cuboctahedrons with the same orientation as the nanoshell. The {111} facets denoted by an "x" show a partial or complete opening. Figure taken from reference 128.

developed a single large opening at its base. This is followed by a progression which transforms the structure into a nanocage, [129,130] a designation attributed to hollow structures with a geometric pattern of openings over their surface (**Figure 5.2 g, h**). This late-stage behavior is consistent with the dealloying process.

Further insights into the dealloying process are obtained by comparing SEM images for nanoshells derived from Au passivated templates of various orientations. **Figure 5.3** shows the early and late stages of the dealloying process for [100]-, [110]-, [111]-, and [211]-oriented structures where the structure orientation is assigned based on faceting consistent with a substrate-truncated cuboctahedron. Evident is the early stage edge deposition and late stage dealloying of the {111} facets.

5.3 Crystallinity and the Hollowing Process

A sampling of partially reacted structures with various crystallographic orientations and faceting reveals that the channel formation is characteristic of substrate-based galvanic replacement processes on Au-coated silver templates. **Figure 5.4** shows TEM images and Selected Area Electron Diffraction (SAED) patterns for four sets of structures corresponding to the [211]-, [100]-, [111]-, and [110]-orientations. The images and SAED patterns for all similarly oriented structures have been rotated such that their crystallographic axes are aligned. Adjacent to the structures of each orientation is a stereographic projection (i.e., a Wulff net) showing the crystallographic directions for all low index planes. In this depiction the Miller index at the center corresponds to the crystallographic direction normal to the substrate while those at the outer extent correspond to in-plane directions. Intermediate values represent possibilities between these two extremes. An examination of the structures reveals that the channel consistently lies along

one of the <110>-directions regardless of the faceting or structure orientation. Nanocage structures with the characteristic <111>-oriented pattern of openings were observed for the [100]- and [111]-orientations (denoted by white arrows in (**Figure 5.4 h, l**). Further insights regarding the galvanic replacement process are garnered from an examination of the underlying crystallography of the structures. If the channels, as the data indicates, form preferentially along the in-plane <110>-directions then [211]-oriented templates present only one possible channel direction, i.e., along the in-plane [01-1]-direction (**Figure 5.4 q**).

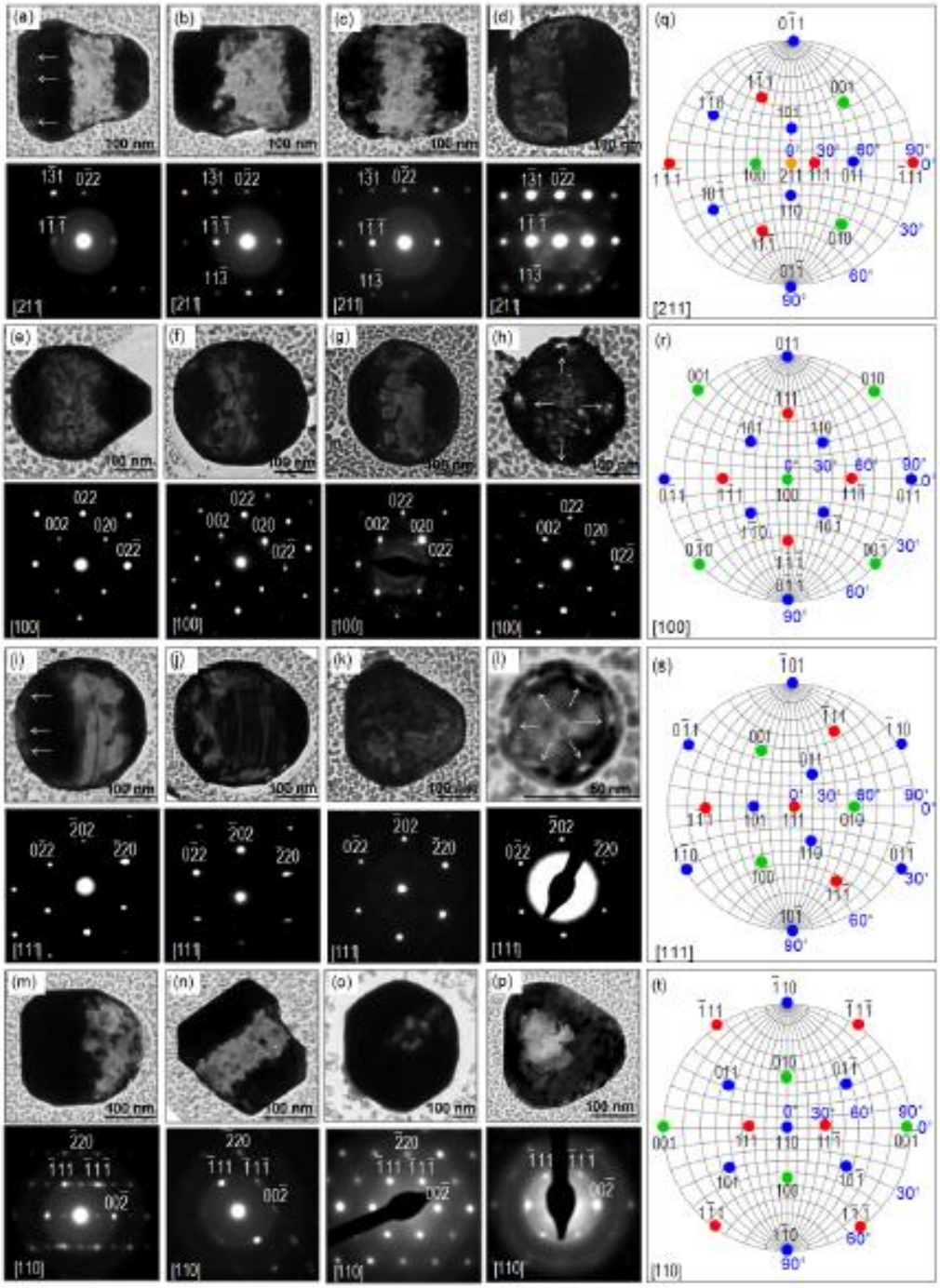

Figure 5.4 TEM images and the corresponding SAED patterns for structures derived from Au-coated silver templates with the (a)-(d) [211]-, (e)–(h) [100]-, (i)–(l) [111]-, and (m)–(p) [110]-orientation normal to the Si_3N_4 surface. To the right of each set of similarly oriented structures is (q)–(t) a stereographic projection showing the crystallographic directions for all the low index planes. It is noted that many of the imaged structures lie on top of the remnants of the thin discontinuous Au film because they have moved on the TEM grid during the drying process which occurs after the galvanic replacement reaction has been terminated. Figure taken from reference 128.

5.4 Defect Transfer

The result also suggests that the galvanic replacement process is amenable to defect transfer between the template and nanoshell. It is noted that the transfer of stacking faults from a Ag seed to a Ge nanowire has recently been demonstrated for a vapor-solid-solid growth mode.[131] Also noteworthy is that nanoscale fcc metals with stacking faults show enhanced mechanical properties due to the inhibition of dislocation motion.[132,133] **Figure 5.5** shows TEM micrographs of AuAg nanoshells of various orientation, where streaking in the electron diffraction patterns along with the micrographs confirm the presence of stacking faults, which are attributed to defect transfer during the shell growth process.

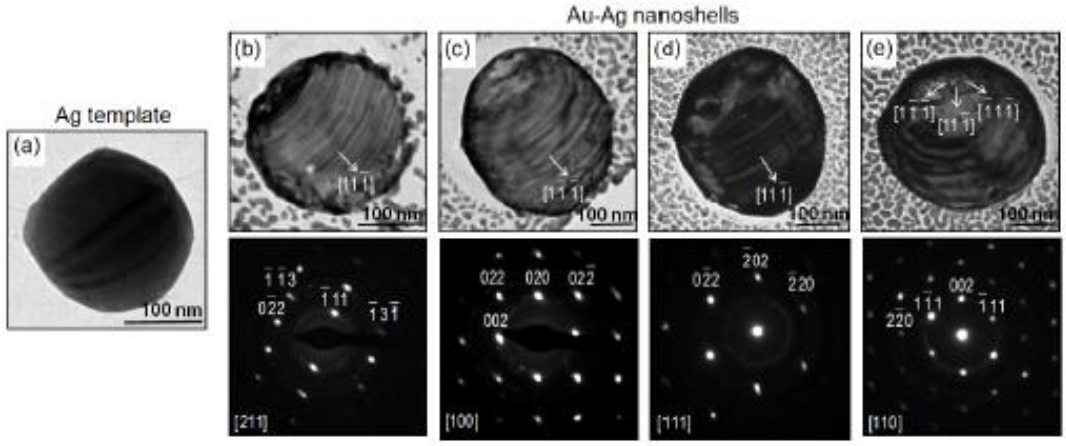

Figure 5.5 TEM images and the corresponding diffraction pattern for (a) a Ag template and for (b) [211]-, (c) [100]-, (d) [111]-, (e) [110]- oriented nanoshells showing prominent stacking faults along a <111>-direction. Figure taken from reference 128.

5.5 Conclusions

Demonstrated is that the early stages of substrate-based galvanic replacement reactions lead to late stage instabilities which give rise to a morphological deconstruction of the nanoshells produced. By merely coating the outer surface of the sacrificial template with a thin layer of Au prior to reaction we inhibit these instabilities, fundamentally altering the

product of the reaction. In contrast to the porous, rough nanoshells derived from the uncoated template, the Au layer leads to the formation of hollow Au–Ag nanoshells which are smooth, robust and crystalline and which exhibit a well-defined pattern of geometric openings. We attribute these differences to the passivation of the highly reactive surface of the silver template by the Au layer. In the absence of this passivating layer, the surface topography of the emerging nanoshell is dramatically altered by the highly reactive nature of curved surfaces of the sacrificial template. This gives rise to a nanoshell with a weak structural framework that is unable to withstand the destabilizing influences of dealloying and thermal diffusion processes. Surface passivation, however, prevents these destabilizing influences, allowing for the orderly dissolution of the template from a single pit at its base. Unique to these studies is the observation that the hollowing initiates in a <110>-direction and proceeds first through the rapid dissolution of a single channel across the entire extent of the template followed by the removal of the remaining Ag. This observation is attributed to the combined influences of atoms in {110}-surfaces having low coordination, the Au^{3+}-poor environment within the interior of the hollowing shell and a reaction that proceeds through the transfer of electrons from an inner shell anode to an outer shell cathode. The final stages of the reaction lead to the formation of openings in the <111>-directions where each template orientation relative to the underlying substrate yields a unique nanocage geometry. Collectively, these synthetic and mechanistic findings demonstrate the critical importance of template engineering in substrate-based galvanic replacement reactions.

CHAPTER 6

TEMPLATE DESIGN CRITERIA FOR PT NANOSHELLS

6.1 Introduction and Motivation

Galvanic replacement reactions yielding platinum nanoshells are of intense interest due to the anticipated enhancements to the catalytic activity derived from high surface area nanostructures with morphologies tailored to optimize specific rates of reaction.[67,134] Sacrificial silver templates with numerous morphologies (nanosphere,[135-137] nanocube,[138-144] nanoplate,[145] nanorod[146] and nanowire[147-152]) have been reacted with various platinum reagents (i.e. H_2PtCl_6 [142] K_2PtCl_4 [150] and Na_2PtCl_4 [140]). The nanoshells produced consistently have a much rougher morphology compared to Au nanoshells derived from identical Ag templates. Possible explanations for the poor morphology include: (i) the 4.1% lattice mismatch between platinum and silver, (ii) the poor miscibility of the Ag-Pt binary system at reaction temperatures and (iii) the reaction by-product chlorine which initiates the growth of AgCl on the template surface.

The substrate-based platform allows each of these possibilities to be addressed individually. Passivating the template surface with a thin layer of gold will inhibit AgCl formation. If the product of this reaction is a smooth platinum nanoshell then lattice mismatch can be ruled out as the source of roughness since the Au-Pt and Ag-Pt combinations have an almost identical lattice mismatch. Miscibility issues will be examined using the numerous template materials accessible through thermal dewetting where the observed morphology and degree of nanoshell alloying will be analyzed in terms of the Hume-Rothery rules and the expected equilibrium behavior derived from binary phase diagrams.

While Ag is the predominant template material, its inadequacies have motivated studies targeting the synthesis of superior nanoshells through the use of alternate template materials and/or chemical modifications to the surface of existing templates. The galvanic replacement of Co[153,154] and Ni [155,156] templates both yield porous shells comprised of many small interconnected lobes. Hollow nanoboxes with a similar surface morphology were derived from Cu_2O nanocube templates.[157] Noteworthy, however, is that the synthesis gave rise to nanostructures comprised of pure Pt which, because they lack surface agents, present clean catalytic surfaces. Cu nanowire templates yield Pt nanotubes with significant Cu alloying,[152,158] but where the surface morphology, while still exhibiting some roughness, is superior to all of the aforementioned template materials. Te nanowire templates, when reacted in ethylene glycol, yielded smooth nanotubes, but where unsatisfactory morphologies are obtained when carrying out the same reaction in water or ethanol.[159] Noteworthy, is that Pt nanoshells with smooth and continuous walls have been achieved through modifications to the template surface prior to the onset of the galvanic replacement reaction. Ag nanowire and nanocube templates with a thin AgCl surface layer give rise to smooth Pt nanotubes[160] and nanoboxes,[161] respectively. Morphological improvements are also observed for Ni nanowire templates when exposed to an H_2SO_4 pretreatment.[162] Also of note is the morphological control asserted for the galvanic replacement of highly faceted Pd templates when exposed to Br^- during the replacement reaction.[143]

Studies performed to date have definitively established the importance of template design in determining the product of galvanic replacement reactions directed toward the formation of Pt nanostructures with hollowed morphologies. The varied nature of the numerous synthetic protocols does, however, make it difficult to separate out the role of

the template's elemental make-up from confounding factors which arise when comparing reactions with dissimilar reagents, concentrations, temperatures and durations carried out on templates with different sizes, shapes, faceting and surface agents. Here, we demonstrate the galvanic replacement of both bare and surface-modified Ag, Pb, Cu, Ni and Co templates with aqueous H_2PtCl_6, where all of the templates are of similar size and shape and exposed to comparable reaction conditions. The product of the reaction, for all bare templates is an alloyed nanoshell with a rough morphology, but where surface modifications to certain templates yield a near-pure product with a smooth and continuous surface. Based on these findings, presented are design criteria for template architectures able to promote the formation of smooth nanoshells with minimal alloying.

6.2 Processing of Diverse Template Materials (Ag, Cu, Ni, Co, Pb)

The electrochemical potential, replacement ratio, crystal structure, lattice constant and anticipated elastic strain imposed on the depositing nanoshell due to lattice mismatch with the template for all of the aforementioned materials is summarized in **Table 6.1**. The templates were then transformed into nanoshells through galvanic replacement in aqueous H_2PtCl_6. Noteworthy, is the fact that all of these reactions were carried out in the absence of capping agents. Such agents prevent the agglomeration of solution dispersed templates, but often complicate reaction pathways [137,161] and/or result in diminished catalytic activity.[163,164]

Table 6.1 Template Material Parameters

Element (Ion)	Redox E° (V vs. SHE)	Replacement Ratio (X:Pt)	Crystal Structure	Lattice Constant (Å)	Induced Force in Platinum Layer
Pb (Pb^{2+})	-0.13	2:1	FCC	4.951	Tension
Ag (Ag^{+})	0.80	4:1	FCC	4.085	Tension
Pt (Pt^{4+})	0.74	N/A	FCC	3.942	N/A
Ni (Ni^{2+})	-0.24	2:1	FCC	3.524	Compression
Cu (Cu^{2+},Cu^{+})	0.34, 0.52	2:1, 4:1	FCC	3.615	Compression
Co (Co^{2+})	-0.28	2:1	HCP	2.507, 4.070	Compression[a]

Table 6.1. Template material parameters of relevance to Pt-based galvanic replacement reactions. [a] Co is based on comparisons of interatomic distances in the close-packed plane. Table Reprinted with permission from ref 165. Copyright 2014 American Chemical Society.

6.3 The Role Crystal Structure and Strain Induction

Using sacrificial templates derived from the solid state dewetting of five different elements we have demonstrated substrate-based galvanic replacement reactions yielding Pt nanoshells. In all cases, we were only able to form smooth continuous nanoshells when a thin passivation layer was applied to the template prior to the initiation of the replacement reaction. The ability to form smooth nanoshells irrespective of the shell composition establishes template surface passivation as the primary mode by which smooth Pt nanoshells are obtained. Such shells exhibited minimal alloying with Cu, Ni and Co templates, but showed a high degree of alloying with Ag and Pb. We assert that nanoshell alloying is a kinetically driven process strongly dependent on heteroepitaxial strains originating from lattice mismatch between the depositing shell and underlying template material, whereby compressive strains inhibit alloying while tensile strains promote it. **Figure 6.1** provides a schematic of the proposed mechanism along with SEM micrographs of the derived platinum nanoshells.

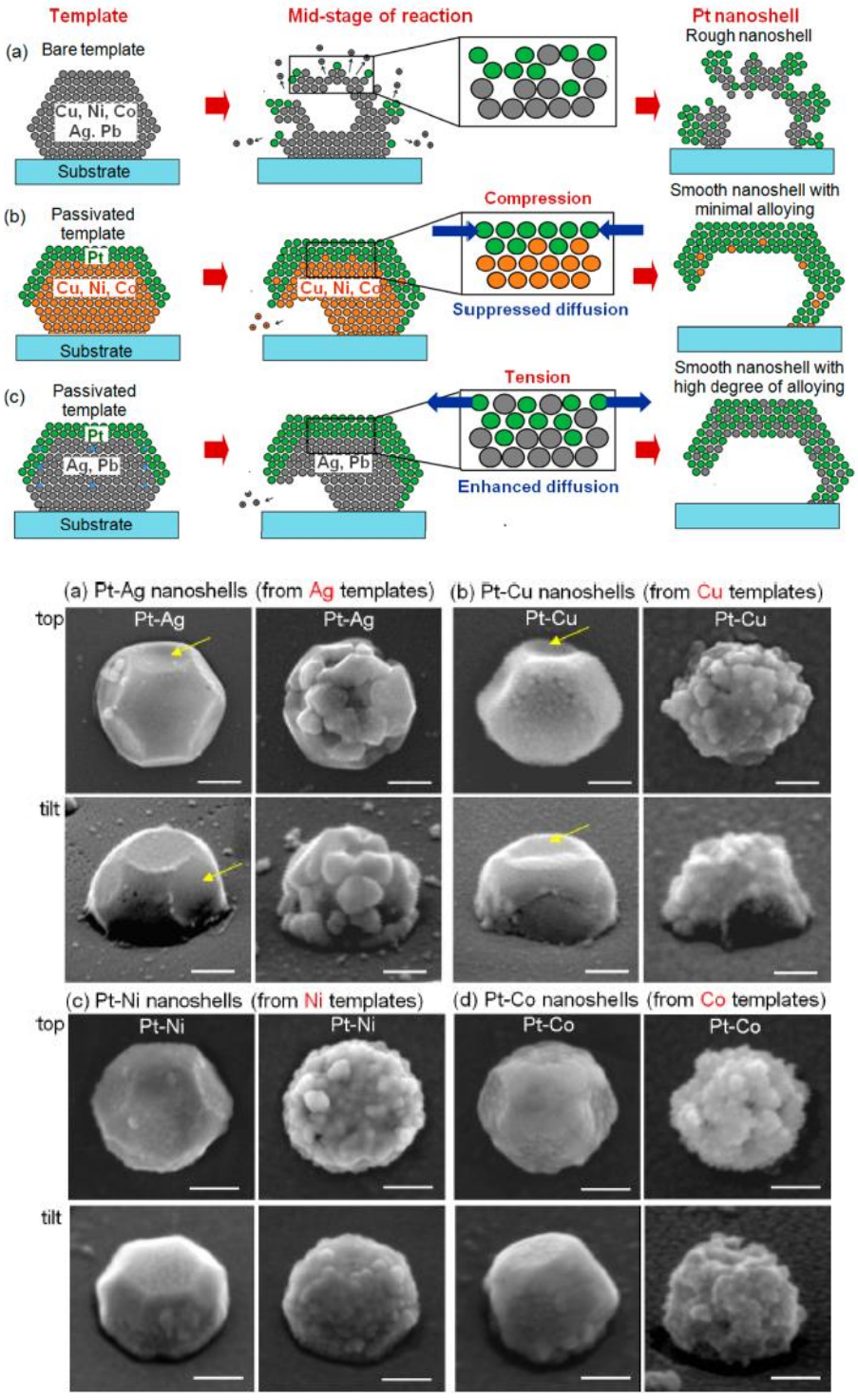

Figure 6.1 The schematic shows how the template nanostructure dictates the degree of alloying between the depositing shell and template. Three cases are shown, (a) zero strain between the shell and template, (b) induced compression in the depositing shell and (c) induced tension in the depositing shell. The SEM micrographs on the right show results nanoshells with and without the use of a passivation layer. Figure taken from ref 165. Copyright 2014 American Chemical Society.

6.4 Design Criteria for Platinum Nanoshells

In order to derive pure Platinum nanoshells, the core should be composed of an element which is readily oxidized and which promotes a heteroepitaxial relationship which places the depositing material under the compressive strains needed to impose a significant barrier to diffusion. The shell should (i) be inert to replacement, (ii) have a composition identical to the element being reduced onto the surface during galvanic replacement or, alternatively, be amenable to removal through selective etching following the reaction, (iii) be thin enough to promote a breach from which the core material can exit the structure as it is oxidized, and (iv) have conductivity sufficient to allow for the electron flow needed to sustain a galvanic replacement reaction between an inner anode and an outer shell cathode. A pure platinum nanoshell is shown in **Figure 6.2**, where Cu, a metal which conforms to the required criteria, is used as the template.

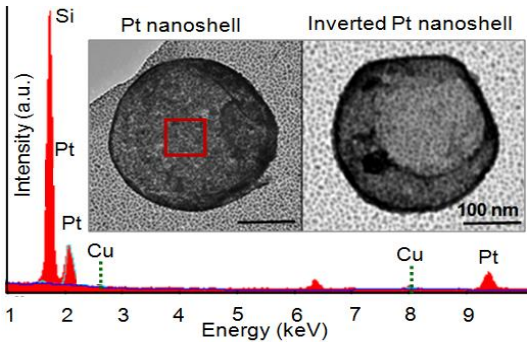

Figure 6.2 TEM image of a smooth Pt nanoshell and an inverted nanoshell resting on a TEM grid. The EDS spectrum shows that the Pt shell is free of Cu. Figure taken from ref 165. Copyright 2014 American Chemical Society.

6.5 Conclusions

Using sacrificial templates derived from the solid-state dewetting of five different elements, we have demonstrated substrate-based galvanic replacement reactions yielding Pt nanoshells. In all cases, we were only able to form smooth continuous nanoshells when a thin passivation layer was applied to the template prior to the initiation of the replacement reaction. The ability to form smooth nanoshells irrespective of the shell composition establishes template surface passivation as the primary mode by which smooth Pt

nanoshells are obtained. Such shells exhibited minimal alloying with Cu, Ni, and Co templates, but showed a high degree of alloying with Ag and Pb. We assert that nanoshell alloying is a kinetically driven process strongly dependent on heteroepitaxial strains originating from lattice mismatch between the depositing shell and underlying template material, whereby compressive strains inhibit alloying while tensile strains promote it. It is, thus, concluded that appropriately designed core−shell templates provide the clearest pathway to the synthesis of smooth continuous nanoshells with minimal alloying.

CHAPTER 7

SOLUTION PHASE NUCLEATION OF Ag ON Au SEEDS

7.1 Introduction and Motivation

The seed-mediated synthesis of metal nanostructures in liquid media has given rise to an extraordinary range of nanomaterials with functionalities resulting from the ability to tailor the size, shape, and composition of the structure.[166] Extending synthetic protocols beyond single-component systems to the realm of bimetallic nanostructures offers the opportunity to create architectures with enhanced functionalities derived from the integration of materials with dissimilar physical and chemical properties into a single nanostructure.[167]

Such structures have already attracted considerable attention due to their potential for application in the areas of catalysis,[168] plasmonics,[169] chemical and biological detection,[170] and magnetism.[171] The full potential of such structures will, however, only be realized if a new set of synthetic challenges associated with heterogeneous nucleation, maintaining heteroepitaxy, and controlling a facet-dependent overgrowth are overcome. With the potential for attaining important catalytic and plasmonic properties, seed-mediated strategies present a compelling route for the synthesis of bimetallic noble metal nanostructures with a core−shell morphology (denoted as core@shell). While a number of early synthetic achievements were reported for the Au@Ag system,[172-174] the protocol of Sanedrin et al.[175] is unique in their demonstration of L-ascorbic acid (AA) as an effective agent capable of uniformly reducing Au^{3+} ions onto Ag seeds. Using the same reducing agent, Habas et al. demonstrated the formation of Pt@Pd structures where Pd deposited conformally on well-faceted Pt seeds.[176] Their attempts to form Pt@Au structures,

however, resulted in anisotropic growth modes, a result which led them to conclude that the poor morphology was associated with the sizable lattice-mismatch occurring at the Au−Pt interface (4.08% compared to 0.7% for Pd−Pt). In a comparative study, Fan et al. used AA to reduce Ag, Pd, and Pt onto Au seeds with an octahedron geometry.[177] While conformal epitaxial overgrowth was observed for the Au@Ag and Au@Pd systems, the Pt overgrowth of the Au seed was both rough and polycrystalline. With the Au@Pd system showing conformal epitaxial growth and the largest lattice-mismatch (i.e., larger than Au@Pt), the work demonstrated that epitaxial heterogeneous nucleation was not simply dependent on having a small lattice-mismatch. On the basis of these results, they proposed three criteria for epitaxial heterogeneous nucleation: (i) the lattice constant of the shell metal should be less than that of the core where the degree of mismatch is less than 5%; (ii) the electronegativity of the shell metal should be less than that of the core metal; and (iii) the bond energies between the core and shell atoms should be larger than those between shell atoms. The motivation behind the criteria was to promote conditions analogous to those used to achieve smooth heteroepitaxial film growth in the vapor phase (i.e., a Frank-van der Merwe growth mode) while preventing the galvanic replacement of the metal seed. It is, however, noted that Qin and co-workers showed that the galvanic replacement of Ag nanocubes could be augmented by an AA-induced co reduction of Au and Ag onto the corners and edges of the cube.[178] Their synthesis yielded hollow Au−Ag nanocubes with sharpened geometrical features and an enhanced Ag content, properties which gave rise to a 33-fold improvement in the surface-enhanced Raman scattering. By increasing the deposition rate through the use of a strong reducing agent, they were also able to completely block the galvanic replacement of Ag and, thus, form Ag@Au nanocubes.[179] An even more

thorough understanding began to emerge with the demonstration of the decisive role that kinetics play in determining the reaction product. Using the Pt@Pd system, Lee et al. demonstrated, through modulations to the reduction rate, that it was possible to transform the growth mode from one where Pd overgrew the {100} facets of a Pt nanocube to one where the Pd growth emanated from multiple corners of the cube.[180] Using the same system, Lim et al. varied the rate of reduction through the use of strong and weak reducing agents (i.e., AA vs citric acid) and conclusively demonstrated that faster kinetics gave rise to conformal deposition while a slower rate of reaction resulted in dimer structures.[16] Yang et al. observed similar behavior and used it to assert kinetic control over the reduction of Ag onto Au seeds in a manner yielding an impressive family of intricate bimetallic nanostructures.[181] Recently, Zhu et al. performed a detailed study on the Pd@Ag system where they explored numerous aspects of the reaction including the concentration of both the shelling and seed material, the molecular weight of the capping layer, the strength of the reductant, the pH, and the reaction temperature.[182] They showed that the conformal overgrowth of a Pd seed with Ag occurred when (i) the capping layer, polyvinylpyrrolidone, had a higher molecular weight and a lower concentration, (ii) the reductant was stronger (i.e., hydrazine vs formaldehyde), and (iii) the reaction was carried out at a higher temperature. While these important findings all point toward the seed-mediated synthesis of bimetallic nanostructures being heavily reliant on reaction kinetics, the exact mechanisms responsible for such phenomena are still under consideration.[183]

Taken together, the aforementioned studies demonstrate that the seed-mediated synthesis of bimetallic nanostructures is sensitive to a wide range of parameters including temperature, pH, the surfactant utilized, the strength of the reducing agent, the precursor

concentration, injection rates, the physical properties of the seed (i.e., size, shape, faceting, composition), and seed−shell interfacial interactions arising from differences in lattice constant, electronegativity, and bond energies. While such sensitivities lead to a high degree of synthetic flexibility, the highly intertwined nature of these parameters makes it difficult to decipher growth pathways and determine if particular parameters are acting synergistically or in discordance. The role of surfactants is particularly convoluted as they can (i) prevent nanoparticle aggregation, (ii) induce anisotropic growth modes through preferential binding to specific facets, (iii) act as effective reducing agents able to generate solution-based nanostructures (i.e., the polyol process), and/or (iv) induce plating of a secondary metal onto a preformed seed. Synthetic routes carried out in a surfactant-free environment are, therefore, compelling from the standpoint of establishing a mechanistic framework as they allow for chemical interactions at the seed−solution interface which are defined purely by the intrinsic surface energy of the expressed seed facets against the chemical potential of the solution. The synthesis of bimetallic core−shell structures using surfactant-free protocols is often impractical when using solution-dispersed seeds because there is a strong tendency for both the seeds and the forming structures to aggregate. This tendency to aggregate can, however, be nullified if the seeds are immobilized on the surface of a substrate. Previously, demonstrated was the utility of immobilized structures in the synthesis of substrate-based hollow metal nanoshells and nanocages using galvanic replacement reactions. In addition to eliminating the surfactant requirement, the substrate-based platform offers a number of other advantages including the ability to (i) form nanostructures in periodic arrays, (ii) easily assemble a wide variety of seed materials using solid-state dewetting and associated techniques, (iii) control the crystallographic

orientation of the seed through its heteroepitaxial relationship with the underlying substrate, and (iv) form faceted seeds which take on a truncated octahedron geometry which exhibits distinct {100} and {111} facets.

Herein, we utilize this platform to investigate the heterogeneous nucleation of Ag on surfactant-free Au seeds. The nucleation event is investigated from start to finish for three kinetic regimes where for each case Au seeds are examined which have their [100], [110], or [111] axis perpendicular to the surface of the substrate. The study demonstrates both a facile synthesis route for the generation of a distinct family of substrate-based core−shell structures while providing insights into the underlying kinetic mechanisms which modulate the seed-mediated synthesis of bimetallic nanostructures in an aqueous medium.[184]

7.2 Bimetallic Structures Synthesized in the Regime of Slow Kinetics

A highly anisotropic growth mode is observed when [111]-oriented Au seeds with a truncated octahedron geometry (**Figure 7.1a**) are exposed to the regime of slow kinetics. **Figure 7.1b** shows an SEM image of a periodic array of reacted seeds. Emerging from each of the truncated octahedrons is a structure which is either three- or six-fold symmetric (**Figure 7.1c**), geometries consistent with the largest facet being [111]-oriented. The overall faceting is consistent with either a hexagonal or truncated bipyramid geometry, structures which require the existence of a single planar twin boundary parallel to the largest [111] facet. The triangle edge length/thickness ratio consistently lies in the range of 2:3. Noteworthy is that in no instance have we observed seeds which nucleate more than one of these structures. Images taken in electron backscattering mode (**Figure 7.1d**), elemental mapping (**Figure 7.1e**), and line scans (**Figure 7.1f**) all confirm the anisotropic

deposition of Ag. The elemental mapping does, however, suggest that some alloying may occur at the Au−Ag interface and that a small amount of Ag is deposited over the entire Au seed. The nucleation site for both the triangular and hexagonal Ag structures is always one of the six {100} Au facets (**Figure 7.1e**). Strong evidence for a heteroepitaxial relationship at the nucleation site is provided by the fact that the [111] Ag facet for both the triangular and hexagonal geometries is always parallel to one of the {111} Au facets on the truncated octahedron.This geometrical relationship is highlighted by the labeled facets in **Figure 7.1e**, which show the (111) Ag facet being parallel to the (111) Au facet.

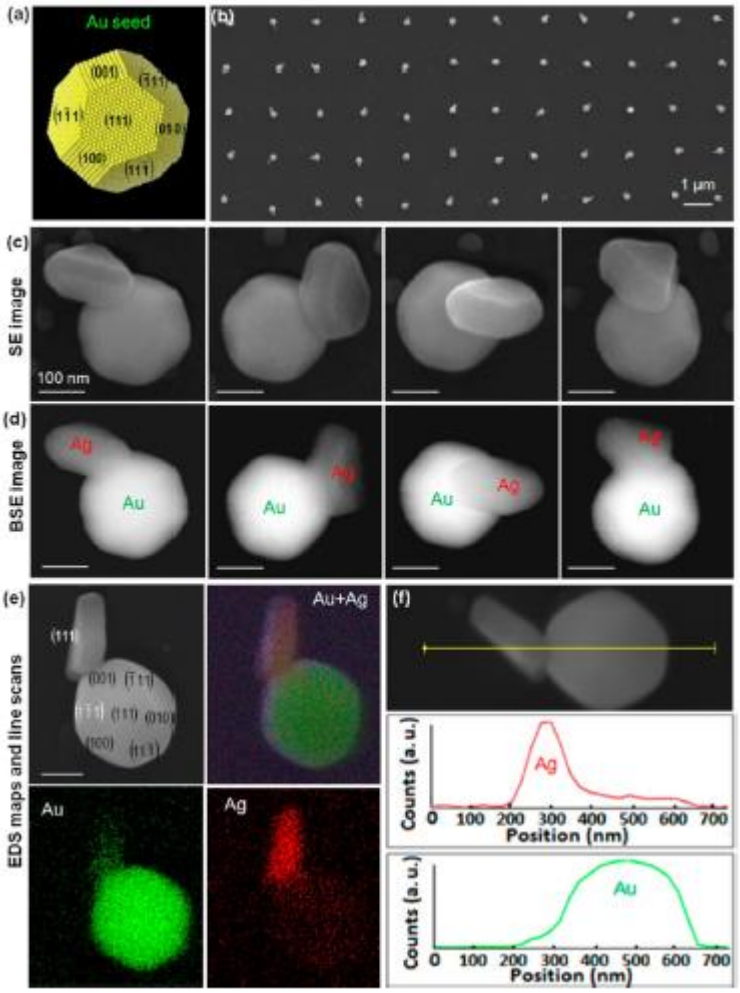

Figure 7.1 Morphological and elemental characterization of Au−Ag heterodimer structures formed in the regime of slow kinetics. (a) Schematic depicting the expected topography for a [111]-oriented Au seed with facets defined by the geometry of a truncated octahedron. (b) SEM image of a periodic array of Au−Ag dimer structures. High magnification SEM images of individual structures taken in (c) secondary electron (SE) and (d) backscattered electron (BSE) mode. (e) Elemental maps and (f) line scans showing the distribution of Au and Ag within the dimer structure. Figure taken from 184. Copyright 2014 American Chemical Society.

7.3 Bimetallic Structures Synthesized in the Regime of Moderate Kinetics

In the regime of moderate kinetics, Ag deposition initially occurs on the {100} Au facets of the truncated octahedron. The deposition occurs in a manner which replaces the exposed {100} Au facets with Ag pyramidal structures bound by {111} facets. The overall

structure, therefore, trends toward an octahedral geometry. **Figure 7.2** shows a schematic of the expected geometry and the corresponding SEM images, elemental maps, and line scans for bimetallic structures formed using [111]-, [110]-, and [100]-oriented Au seeds (note that the structures referred to as [100]-oriented are somewhat tilted off of the true [100] axes).

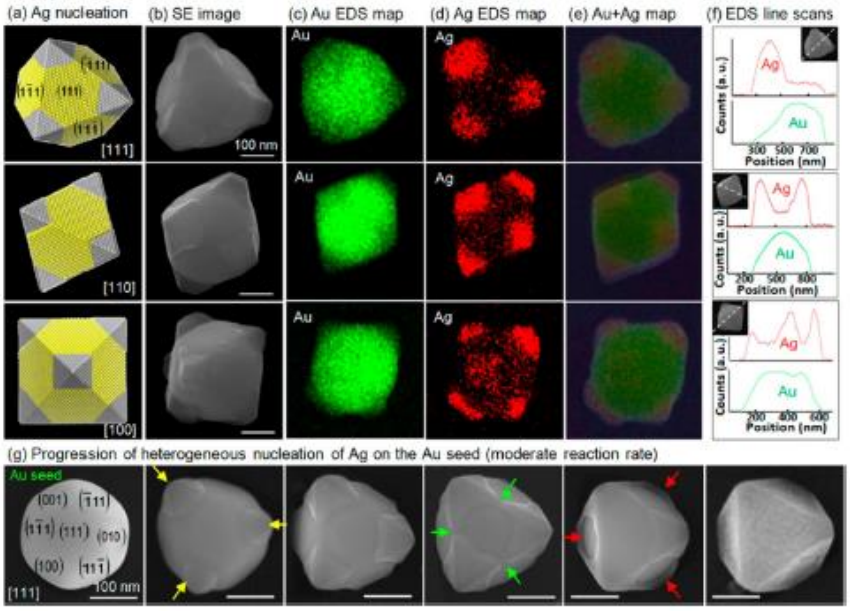

Figure 7.2 Early stage morphological and elemental characterization of bimetallic Au−Ag structures formed in the regime of moderate kinetics. (a) Schematic depictions of the topography expected for bimetallic structures formed after the deposition of Ag on the {100} facets of [111]-, [110]-, and [100]-oriented Au seeds. (b) SEM images of the structures formed in the early stages of the reaction and their corresponding (c) Au, (d) Ag, and (e) Au+Ag elemental maps and (f) line scans. (g) SEM images showing the early to late stage progression in morphology which reveals a Au seed being overgrown with Ag to the point of encapsulation. Figure taken from 184. Copyright 2014 American Chemical Society.

While the structures in this regime show nearly identical Ag growth on all {100} Au facets (**Figure 7.2b**), it is noted that slightly slower reaction rates yield pyramidal structures with sharp corners, but where some of {100} facets are left unreacted. Slightly greater rates lead to structures with a mixture of sharp and blunt corners. The elemental maps and line scans

for all three orientations (**Figure 7.2c−f**) show preferential Ag deposition on the {100} facets of the Au seed, with little deposition elsewhere. If, however, the reaction is allowed to proceed for longer times, the seed becomes completely overgrown with Ag. **Figure 7.2g** shows the progression observed as more and more Ag is deposited onto a [111]-oriented Au seed. After an initial stage, which sees the formation of Ag pyramids on the {100} Au facets (denoted by yellow arrows), Ag begins to deposit along the edges of the Au truncated octahedron where the {111} Au facets meet (denoted by green arrows), a process which eventually leaves the {111} Au facets partially exposed and encircled by Ag (denoted by red arrows). Continued deposition results in the complete overgrowth of the exposed facets, forming an octahedron with Au@Ag geometry. Such structures are formed for all seed orientations.

Figure 7.3a,b shows schematic representations of the [111]-, [110]-, and [100]-oriented Au seeds and the core−shell geometries expected after Ag overgrowth. SEM imagestaken in secondary electron mode show that these geometries are experimentally realized (**Figure 7.3c**). Backscatter mode images show the Z-contrast expected for Au@Ag structures (**Figure 7.3d**), a geometry which is confirmed by the Au and Ag elemental maps (**Figure 7.3e,f**).

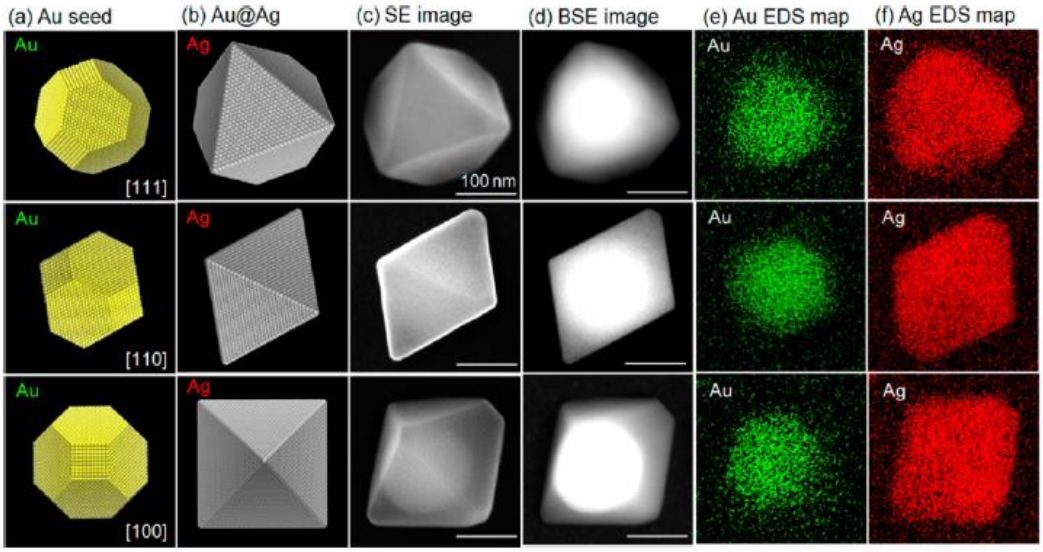

Figure 7.3 Late stage morphological and elemental characterization of bimetallic Au@Ag structures formed in the regime of moderate kinetics. Schematics of (a) [111]-, [110]-, and [100]-oriented Au seeds followed by (b) depictions of the Au@Ag structures formed in the late stages of the reaction. SEM images of the observed structures taken in (c) secondary electron and (d) backscatter modes and their corresponding (e) Au and (f) Ag elemental maps. Figure taken from 184. Copyright 2014 American Chemical Society.

7.4 Bimetallic Structures Synthesized in the Regime of Fast Kinetics

In the regime of fast kinetics, the Au seed becomes encapsulated with a far more uniform layer of Ag in a manner which, to a large extent, preserves the geometry of the initial seed. **Figure 7.4a** shows the progression in morphology which occurs as the Au seed is transformed into a Au@Ag structure. In contrast to the regime of moderate kinetics, early stage Ag deposition on the {100} facets does not lead to the formation of pyramid structures. Instead, the overgrowth is characterized by the simultaneous deposition of a relatively thin layer on the {100} facets (denoted by yellow arrows) and ridges of similar thickness along the edges of the truncated octahedron where the {111} Au facets meet (denoted by green arrows), a process which leaves the {111} Au facets partially exposed and encircled by Ag. Continued deposition results in a contraction of the exposed {111} facet area as a growth front advances to the point of complete seed encapsulation (denoted

by red arrows). The final Au@Ag structure shows a geometry similar to that of the truncated octahedron. **Figure 7.4b−g** shows schematic representations, secondary electron and backscatter SEM images, elemental mapping, and line scans for the so formed structures. The backscatter images confirm the core− shell morphology. Both the elemental mapping and line scans show that, while the overgrowth of Ag onto the Au seed is far more uniform than for the case of moderate kinetics, the lowest rate of deposition still occurs on the {111} Au facets. The Ag line scan for the [100] structure is particularly revealing in this regard as it passes through both the (1−11) and (010) facets but only shows a prominent peak for the (010) facet. Preferential deposition of Ag on the ridges where {111} Au facets meet is apparent from the line scan made over the [110]- oriented structure which shows a peak at each of the three positions corresponding to this feature.

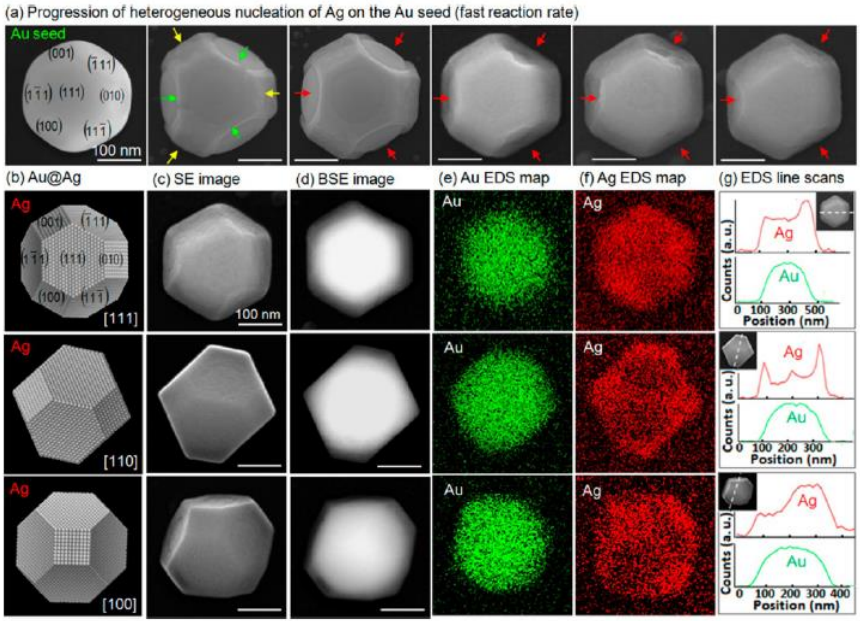

Figure 7.4 (a) SEM images showing the observed progression in morphology where a Au seed is overgrown on its {100} facets followed by the overgrowth of its {111} facets to the point of encapsulation. (b) Schematic depictions of the topography expected for a [111]-, [110]-, and [100]-oriented structure derived from a growth mode which is dominated by the near uniform overgrowth of the {100} Au facets with Ag. SEM images of the observed structures taken in (c) secondary electron and (d) backscatter modes and their corresponding (e) Au and (f) Ag elemental maps and (g) line scans. Figure from 184. Copyright 2014 American Chemical Society.

7.5 Mechanistic Framework

The current study demonstrates that the site-selective heterogeneous nucleation and growth of Ag on Au seeds occurs even if the synthesis is surfactant-free. The slow regime, characterized by a single nucleation event, is quite revealing in that a layer-by-layer growth mode is inhibited off of the (100) Au facet where the nucleation occurs. Instead, an anisotropic Ag growth front propagates away from the seed into the adjacent solution. Also apparent is that the initial nucleation event is not one of low probability as all of the seeds are able to nucleate a single structure of approximately the same size. The nucleation of a second structure onto the same seed is, however, an extremely low probability event, a result whose implication is that the first nucleation event somehow inhibits subsequent nucleation events on the same Au seed. Similar behavior observed in the slow kinetic regime for other systems has been attributed to diffusion of atoms to the single nucleation site or the collision patterns between the seed and atoms in the liquid. These explanations, however, seem implausible for the much larger Ag structures produced in our syntheses (**Figure 7.1c**). Such structures, on average, require the addition of approximately 200,000 Ag atoms/s over the course of the 10 min synthesis. For surface diffusion to occur at these levels without other nucleation events occurring seems unlikely. Thermodynamic arguments also favor a surface diffusion which drives the system toward a geometry with a lower overall surface energy. This, however, is not the case because the final structure significantly increases the overall surface area, and Ag, because of its lower surface energy, should tend to wet Au rather than agglomerate on its surface. In an effort to further rule out surface diffusion as the predominant mass transport mechanism, Ag-topped Au pedestals (diameter 1.2 μm, 10 nm Ag, 50 nm Au) were deposited through a shadow mask and then

exposed to 100 °C aqueous $AgNO_3$ for 10 min. If Ag diffusion on Au is significant and amenable to agglomeration under the reaction conditions, then significant Ag agglomeration should also occur on these pedestals. There is, however, no appreciable agglomeration observed. Collision patterns also seem an unlikely candidate since liquid flow patterns are likely to be similar for adjacent seeds when immobilized in periodic arrays, yet no correlation between the Ag growth front directions for adjacent seeds is observed. We also contend that substrate influences are minimal in establishing this growth mode because sapphire, being an excellent insulator, is unlikely to offer an alternative pathway for electrons involved in the reactions. The fact that the kinetic regimes are similar to those observed when using solution-dispersed templates is supportive of this argument. We cannot, however, completely rule out possible substrate influences derived from its surface-altering liquid flows or through presenting a dielectric medium to the attached seeds. With these explanations seemingly unable to account for the current results, an alternative mechanistic framework (**Figure 7.5**) is required. While the Au seeds used in this study initially exhibit bare metal surfaces, it should be recognized that their placement in a liquid media containing various reactants can dramatically alter this situation. In fact, numerous protocols exist where the synthesized single component metal nanostructures are stabilized against agglomeration, not by surfactants specifically added for this purpose, but by the reducing agents, solvents, or salts used in the synthesis. Such protocols, while referred to as surfactantfree, still result in the formation of a stabilizing layer around each nanoparticle, but where the negative impact of this layer on catalytic properties, photoluminescence, and surface enhanced Raman scattering sensitivities is often significantly less than those of surfactants. On the basis of these supportive studies, we

propose that such an interface layer is crucial in rationalizing the site-selective nature of our observed growth mode. With only two reactants, AA and $AgNO_3$, relatively few possibilities exist when trying to deduce the makeup of such an interface. At the beginning of the synthesis, the Au seeds are inserted into a solution of solvated Ag^+ and NO_3^- ions where both the positive and negative ion content is approximately 50 times greater than the number of Au atoms collectively contained within all the substrate-based seeds. Such a situation is very much analogous to the insertion of a metal electrode at zero potential into an electrolytic solution. The resulting interaction can be described in terms of a simple jellium model which depicts a metal as an electron plasma interacting with positive ions represented by a continuous background. At the metal surface, the positive background falls abruptly to zero while the electron distribution extends slightly past this positive boundary. The exposure of this layer to the electrolytic solution leads to a situation where positive metal ions are attracted to the surface and attach either as a layer deposited at underpotential[185] or as a combination of solvated and specifically absorbed ions.[186] With the overall structure becoming positively charged, negative ions will be attracted to it, resulting in the formation of a space charge region consisting of a double layer of positive and negative ions (**Figure 7.5b**). With various crystalline surfaces expressing different surface energies, the consistency of the space charge region is expected to fluctuate over the surface of the faceted metal seed, a property which can ultimately contribute to site selective deposition. Evidence that such a layer exists for the current synthesis is the Ag detected in EDS measurements for the case where Au seeds are exposed to aqueous $AgNO_3$ and then removed from the solution without exposure to a reducing agent. For reduced Ag atoms to nucleate on a Au seed surrounded by an interfacial double layer, they must first

displace the ions which make up this layer. For the slow regime (**Figure 7.5c**), nucleation occurs on a single {100} Au facet, but where layer by- layer growth on the facet is inhibited. Such behavior is consistent with a double layer which is firmly affixed to the Au seed. With nucleation inhibited on the surface of Au, the growth front instead propagates toward the solution on Ag surfaces which are more amenable to deposition. To account for the fact that a second nucleation event does not occur on equivalent facets of the same Au seed, it must be recognized that the initial nucleation event results in the formation of a junction between neutrally charged Ag and a Au structure which is positively charged due the ions which attached to its surface. Such a scenario is conducive to electron transfer from Ag to Au. The electrons added to Au will, in turn, increase the attractive force which binds the double layer to the Au structure and, hence, inhibit the nucleation of Ag on other {100} facets. Reaction rates in the moderate and fast regime (**Figure 7.5d,e**), facilitated by the fast injection of AA, not only give rise to faster kinetics but also result in a rapid decrease in the pH of the solution (compared to the slow decrease resulting from a dropwise injection). Faster kinetics can lead to the near simultaneous nucleation of Ag at multiple

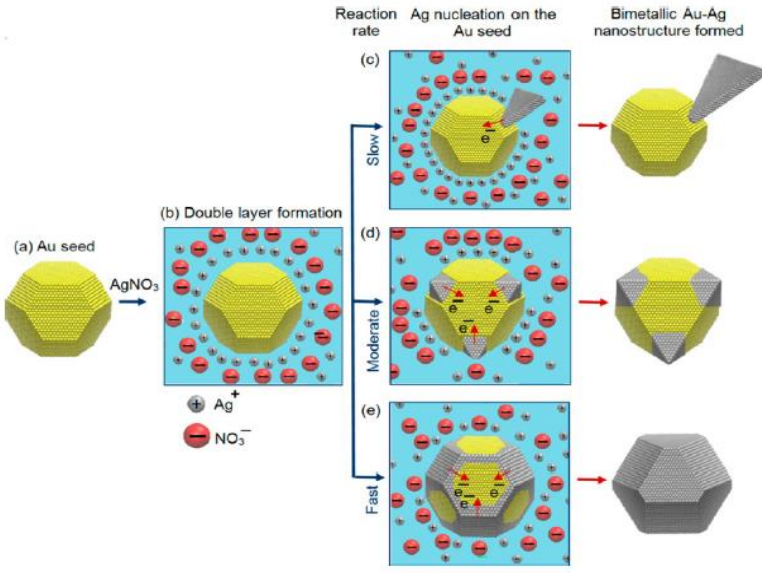

Figure 7.5 Schematic illustration of the mechanistic framework responsible for the heterogeneous nucleation of Ag on surfactant-free Au seeds. It shows (a) the initial seed, (b) the seed after double-layer formation and the progression of the reaction once the reducing agent is added in the (c) slow, (d) moderate, and (e) fast regimes. Figure taken from 184. Copyright 2014 American Chemical Society.

sites on the structures while the increase in pH can fundamentally alter the nature of the double layer surrounding each of the Au structures. If, under these circumstances, the ions forming the double layer are more readily displaced by Ag^{o}, it would account for the layer-by-layer growth observed on each of the {111} Au facets and the eventual overgrowth of the entire seed with Ag.

7.6 Conclusions

In summary, we have demonstrated the heterogeneous nucleation of Ag on substrate-based Au seeds in a surfactant free aqueous medium. Despite the fact that the synthesis is unperturbed by surfactants, the deposition remains anisotropic and strongly dependent on whether the reaction is carried out in a regime of slow, moderate, or fast kinetics. Slow kinetics give rise to a Au−Ag bimetallic heterodimer obtained through epitaxial deposition on just a small portion of a single {100} Au facet followed by the propagation of a rapid growth front away from the seed into the liquid medium. Moderate kinetics result in a Au@Ag structure with an octahedron geometry realized through layer-by-layer deposition of Ag on all {100} equivalent seed facets followed by the overgrowth of all remaining facets. Fast kinetics also result in a core−shell morphology, where the overgrowth more closely follows the topography of the underlying seed. Our understanding of various regimes requires the formation of a facet-dependent space charge region around the seed which is responsive to the injection of electrons from the deposited Ag layer as well as the concentration of ascorbic acid within the solution. Taken together, the work demonstrates that even the simplest of seed-mediated protocols involving heterogeneous nucleation gives rise to unexpectedly rich phenomenology.

CHAPTER 8

VAPOR PHASE NUCLEATION OF AG ONTO AU

8.1 Introduction and Motivation

Photonic surfaces comprised of substrate-immobilized noble metal nanostructures provide the means to advance numerous catalytic,[187,188] photovoltaic[189] and sensing applications.[190] Nanostructures with shape anisotropies, such as nanorods and triangular nanoprisms, are particularly attractive to such applications due to the high tunability of the plasmon resonance.

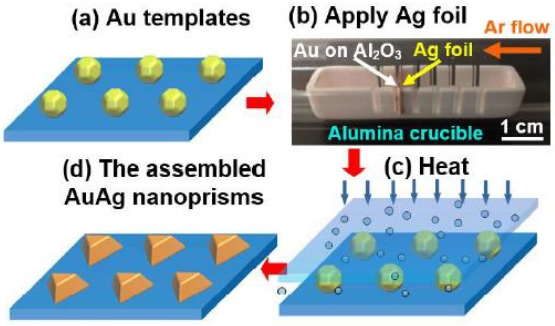

Figure 8.1 Schematic of the devised templated assembly process which transforms substrate-immobilized Au templates into triangular AuAg nanoprisms through the high temperature exposure of Au templates to a Ag flux derived from an adjacent foil. The image shows the experimental configuration utilized. Figure taken from 206.

Nanoprisms are further valued for the intense plasmonic near-fields formed at the triangle tips,[191] a response which can be further amplified by placing two such structures in close proximity in a bow tie configuration.[192] There is also growing interest in the use of these structures as templates capable of defining more intricate nanostructure geometries.[193] Mirkin and co-workers, using a solution-based photochemical synthesis, were the first to synthesize triangular nanoprisms in high yield.[194] The discovery spurred on considerable interest and activity which has recently given rise to the emergence of seed mediated protocols offering higher yields, greater monodispersity, an increased size range and synthetic simplicity.[195] Even though solution-based routes have proven extremely successful in the synthesis of noble metal nanoprisms, many of the aforementioned

applications require that such structures be placed on substrate surfaces. While the dispersal of these nanoprisms onto planar substrates is relatively straightforward, it results in structures which are positioned randomly on the surface[196] or which form an uncontrolled self-assembled pattern.[193] Lithographic techniques have been used to define nanoprisms at site-specific locations,[197] but these approaches can have limitations associated with long processing times, high cost and the low quality factors associated with the LSPR of polycrystalline structures.[198] Recognizing the benefits of placing single crystal nanoprisms onto a substrate surface in an organized manner, Zhou et al. lithographically defined triangular trenches into a substrate which were able to accept nanoprisms dispersed in an evaporating droplet.[199] While impressive, the surfaces of these structures remain coated with capping agents which can negatively impact nanostructure properties.[200,201] Fabricating periodic arrays of noble metal nanoprisms which are surfactant-free, substrate-immobilized, and single crystalline is, therefore, a synthetic challenge which has not previously been met. Physical vapor deposition (PVD) or assembly routes based on solid state dewetting, when carried out on substrates which support an epitaxial relationship, all allow for island growth modes yielding single crystalline nanostructures.[202] While forming [111] oriented noble metal nanostructures is relatively straightforward using these techniques, the structures formed do not typically take on the nanoprism geometry. This is a consequence of the fact that island formation is reliant on high temperature solid state diffusion processes which support the formation of nanostructure geometries with low surface energies realized through a combination of minimizing the surface-to-volume ratio and forming low surface energy facets. Taking these factors into account for elements with face centered cubic (fcc) crystal structures (e.g. Au, Ag) leads to the equilibrium Wulff

shape which is a truncated octahedron with eight hexagonal {111} facets and six square {100} facets.[203] While the exact nature of the epitaxial relationship between the forming nanostructure and the substrate can result in deviations from the Wulff geometry,[202] a substrate capable of promoting Au or Ag nanoprism formation in high yield has not yet been discovered. Previously, we demonstrated the utility of using substrate immobilized Au nanostructures as templates capable of directing high temperature assembly.[204] In these processes, Au nanostructures are confined between an oxide substrate and a second material from which adatoms can be sourced through sublimation. At the assembly temperature these adatoms are unable to spontaneously form stable clusters on the substrate surface. When they encounter a Au template, however, they are readily incorporated to form a new nanostructure with its own unique properties. This strategy has been demonstrated for scenarios where Au is transformed into an alloy,[205] where it forms a eutectic liquid which upon cooling phase separates into a heterodimer structure and where the Au template is sacrificed and replaced with a Wulff shaped Pd nanostructure. Here, we demonstrate that an analogous strategy can be used to transform Wulff-shaped Au nanostructures into triangular AuAg nanoprisms.[206] The transformation is explained in terms of anisotropic kinetic processes which continuously drive the structure towards a nonequilibrium geometry until the assembly process is terminated through cooling. The optical properties of the nanostructures and the hydrogen sensing capabilities of Pd covered nanoprisms are also reported.

8.2 The Fabrication of AuAg Nanoprims

In **Figure 8.1**, a schematic of the procedure used to transform substrate-immobilized Au templates into AuAg nanoprisms is shown. The templates were prepared on (0001)-

oriented sapphire substrates as both periodic arrays with a narrow size distribution and as randomly positioned structures with a broad size distribution. The template-decorated substrate and a rectangular Ag foil of approximately the same dimensions were then inserted into slots cut into an alumina crucible (**Figure 8.1b**). This configuration maintained a small well-defined distance (0.5 mm) between the two surfaces while preventing contact. The crucible was placed in a tube furnace with flowing Ar and heated to 775 °C, a temperature sufficient to drive a flux of Ag from the sublimating foil onto the adjacent substrate. Exposure of the Au templates to this flux resulted in the heterogeneous nucleation of Ag which leads to (i) a morphological transformation from the Wulff shape to a triangular nanoprism and (ii) a compositional transformation from pure Au to a AuAg alloy.

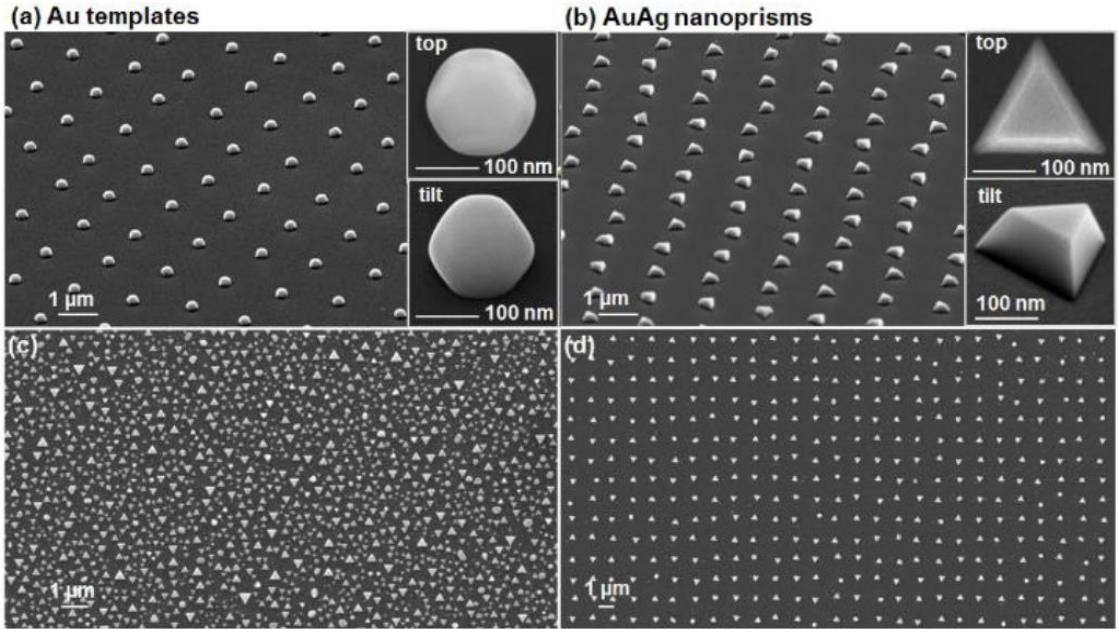

Figure 8.2 Tilted-view SEM images of a periodic array of (a) Au templates and (b) the AuAg nanoprisms derived from them. The insets show top- and 65° tilt-view images of the individual structures. Top-view images of the AuAg nanoprisms assembled using Au templates formed through the (c) solid state dewetting of an ultrathin Au film and (d) dynamic templating. Figure taken from 206.

8.3 Random and Periodic Arrays

Above, **Figure 8.2** shows an SEM image of a periodic array of Au templates as well as top- and tilted-view images of the individual structures. The templates appear rounded, but where weak faceting is observed. The faceting is consistent with the equilibrium Wulff shape. Upon exposure to the Ag flux at elevated temperatures the array undergoes the transformation shown in **Figure 8.2b**.

The individual structures now appear as triangular nanoprisms with the geometry expected for a structure enclosed by {111} facets. A close inspection of these structures, however, reveals that many of them exhibit a slight truncation of the prism corners by {100} facets. The nanoprisms form with two in-plane orientations differing by 180°, a common occurrence for [111]-oriented fcc metals[207] which originates from the fact that neither the ABCABC… nor the reverse ACBACB…. stacking order is favored through epitaxy. In addition to the nanoprisms there are a small number of other structures which show geometries consistent with non-[111]-oriented structures. Noteworthy, is that these structures also show pronounced {111} faceting. When the same synthetic procedure is carried out on similarly shaped templates derived from the solid state dewetting of ultrathin Au films it yields a surface coated with triangular nanoprisms (**Figure 8.2c**) where the randomness in the size and spacing of the initial Au templates is transcribed to the nanoprisms. For this scenario, there is a higher occurrence of structures which differ from the nanoprism geometry in that they are rounded, show substantial truncations and/or deviate from the preferred [111]-orientation. Nevertheless, significance is derived from the fact that a high yield of substrate-immobilized nanoprisms is obtained from templates which are easily fabricated over large areas.

8.4 Time Monitored Morphological Evolution

Figure 8.3 maps out the time-dependent evolution of the nanostructure morphology and composition which occurs as the Au template is transformed into a AuAg nanoprism. All of the structures shown experienced the identical processing conditions except for the exposure time to the Ag vapor at 775 °C which was varied from 30 to 600 min. At the beginning of the process the template is quite rounded, but where {100} and {111} faceting is apparent. The initial exposure of the templates to the Ag flux leads to the preferential growth on the {100} template facets (red arrows) and a sharpening of all edges where facets meet. The favored growth on {100} facets ultimately leads to their annihilation. This occurs because each of these facets is bounded by four inward sloping {111} planes which reduce

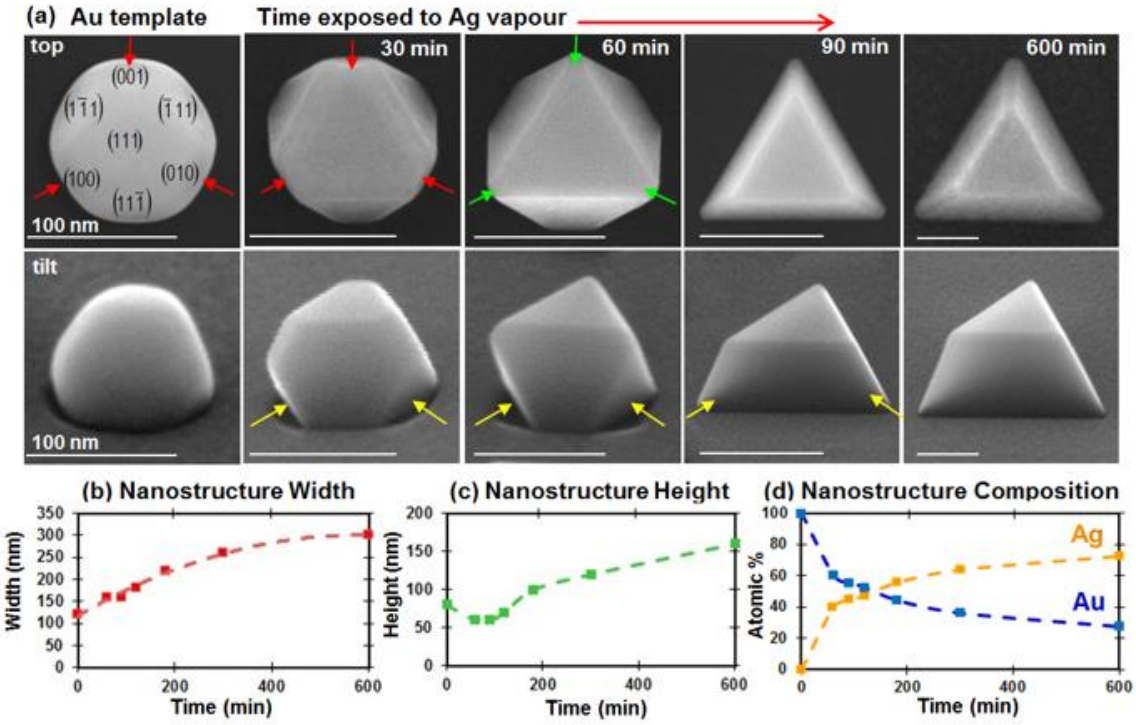

Figure 8.3 (a) Top- and tilted-view SEM images showing a Au template with labelled facets and identical templates as they undergo a shape transformation resulting from their exposure to Ag vapor for time intervals extending from 30 to 600 min. Plots showing the temporal evolution of the nanostructure (b) width, (c) height and (d) composition. Figure taken from 206.

the area of a (100) facet with the addition of each successive layer until finally the facet is extinguished by the pyramidal structure formed (green arrows). At this stage, which occurs after a 60 min exposure to the Ag flux, the emerging structure is bounded by eight {111} facets where seven of them are exposed and the eighth forms an interface with the substrate. Continued deposition on the remaining {111} facets leads to the annihilation of the three facets facing downwards towards the substrate as indicated by the yellow arrows. At this stage (90 min), nanoprism formation is complete. Longer deposition times lead to an increased height and edge length (600 min). **Figure 8.3b-c** shows the time dependence of the nanostructure width and height, where the width plotted is the diameter for rounded particles and the edge length for nanoprisms. The width steadily increases, trending toward a constant value for long time intervals. The height of the structure first declines and then rises steadily. With the areal extent of the top facet diminishing due to three inward sloping {111} facets and the edge length of the overall structure trending toward a constant value, the rise in height is unsustainable. Instead, a steady-state configuration is expected whereby the amount of Ag arriving to the structure is equal to that which is desorbing from its surface. Consistent with this expectation is the evolution in nanostructure composition (**Figure 8.3d**) obtained using EDS which initially shows rapid Ag alloying of the Au template followed by a more gradual increase in the Ag content which appears to be saturating at long time intervals. This data, combined with estimates of the nanoparticle volume, indicate that the Au content within each structure remains approximately constant throughout the nanoprism assembly process.

8.5 Optical Properties and Hydrogen Detection

A single lithographically defined triangular nanoprism placed in close proximity to a nanoscale Pd disc has been demonstrated by Liu *et al.*[208] as an optical hydrogen sensor. The sensing mode is dependent on disruptions to the nanoprism's dielectric environment caused by the uptake of hydrogen by the palladium disc. Motivated by these findings we tested the hydrogen sensing capabilities of an ensemble of substrate-supported triangular nanoprisms coated with a 1 nm thick layer of Pd using a test apparatus and sensing strategy which we describe in detail in Section 4.4 of this proposal. Briefly, the Pd coated AuAg nanoprisms (denoted as AuAg@Pd) are exposed to a broadband incoherent excitation (550 - 650 nm) resonant with the LSPR (i.e. the blue curve in **Figure 8.4a**). The amount of transmitted light is then monitored as the sample is exposed to alternating on/off flows of 10% H_2 90% N_2 gas. The transformation of the palladium to a metal hydride is expected to alter the dielectric environment of the plasmon in a manner which decreases the extinction and red-shifts the LSPR.[209] **Figure 8.4d-e** shows the detection of hydrogen and a schematic illustrating the sensing mechanism. The observed cyclic behavior is characterized by a rapid ~0.13% rise in the integrated transmittance (476 - 731 nm) upon exposure to hydrogen followed by a gradual decline when the hydrogen flow is terminated. The rapid rise and gradual fall is a response characteristic of many metal hydride sensing modes where the hydrogen intake is more rapid than its loss.[210] Important is that neither the AuAg nanoprisms nor a standalone 1 nm thick Pd film yielded a comparable result, a clear indication that detection results from the coupled response originating from a metal hydride in intimate contact with a plasmonic nanoprism. By themselves the AuAg templates

showed no well-defined response while the Pd film initially showed a small detectable response, but which, after several cycles, significantly degraded.

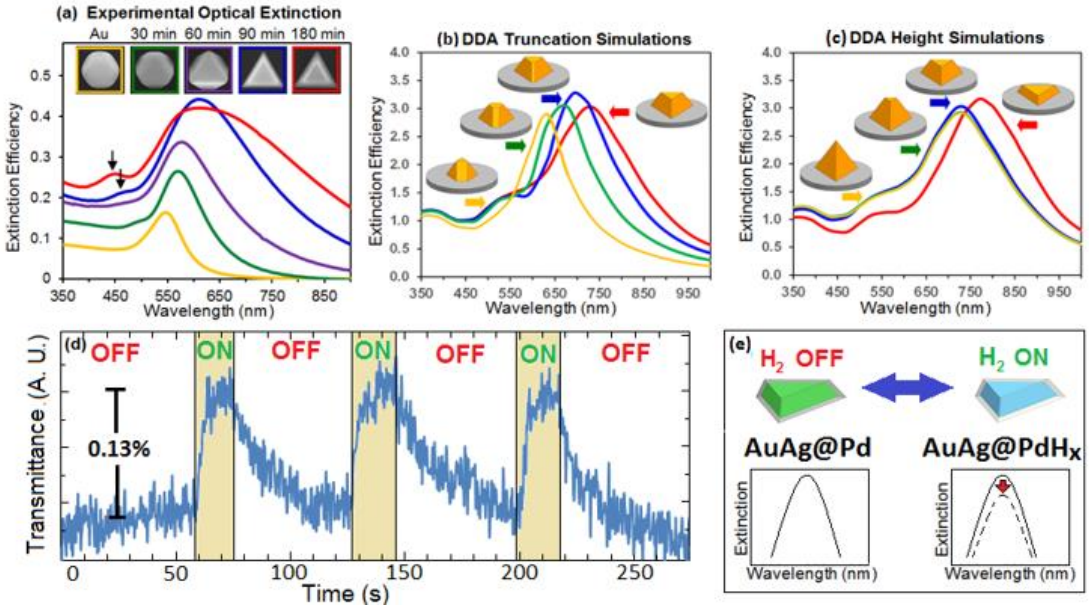

Figure 8.4 (a) Optical extinction spectra for nanostructures which evolve from Au templates to triangular AuAg nanoprisms. DDA simulations of the extinction spectra where (b) the nanoprism corners are subjected to an increasing degree of truncation and (c) the height is systematically increased to the point where a tetrahedron is formed. (d) The integrated transmittance (476-731 nm) through an ensemble of Pd-coated AuAg nanoprisms exposed to on/off cycling of H_2 gas and (e) a schematic of the sensing mode responsible for H_2 detection. Figure taken from 206.

8.6 Proposed Atomic Growth Mode

The experiments carried out demonstrate that the mere exposure of substrate-immobilized Au nanostructures to Ag adatoms at elevated temperatures results in their transformation to alloyed structures with altered geometries, but where the original heteroepitaxial relationship of the Au structure is preserved. Crucial to the assembly process is that the temperature is maintained in a regime where Ag adatoms are unable to cluster in sufficient numbers to nucleate a stable Ag nanostructure before desorbing from the substrate surface. Consequently, Ag adatoms are only able to remain on the substrate

surface for extended periods of time if a suitable heterogeneous nucleation site is encountered. With a hierarchy of bond dissociation energies of Au-Au: 2.34 eV, Au-Ag: 2.10 eV, Ag-Ag: 1.68 eV,[211] the formation of Au-Ag bonds have the potential to significantly extend the adatom lifetime when compared to the Ag-Ag bonds needed to form pure Ag clusters on the substrate. The miscibility of the Au-Ag system then permits Ag vacancy diffusion into bulk Au where Ag atoms are completely stabilized against desorption until they randomly diffuse to the surface. Over time the structure increases in volume as more Ag adatoms are incorporated, but where this additive process is increasingly offset by the Ag desorption. Desorption rates are expected to increase due to the growing: (i) surface area of the alloyed structure, (ii) likelihood that bulk Ag will diffuse to the surface and (iii) reliance on the weaker Ag-Ag bonds within the structure. Eventually, the structure reaches a steady state configuration characterized by an equal number of Ag atoms arriving to and leaving the structure.

While the transformation of the Au nanostructures to a Au-Ag alloy is readily understood, the accompanying shape-transformation is far more subtle. Revealing is the fact that the dewetting process, when carried out using ultrathin AuAg films, gives rise to rounded structures with many showing faceting consistent with the Wulff shape. The result suggests that the Wulff shape remains the equilibrium configuration for the AuAg alloy. We, therefore, assert that nanoprism formation is driven, not by the energy minimization of the overall structure, but by kinetic processes which favor the establishment of {111} facets. Strongly supportive of our assertion are the molecular dynamic (MD) simulations of Baletto *et al.*[212] which show that kinetic regimes exist where the arrival and attachment

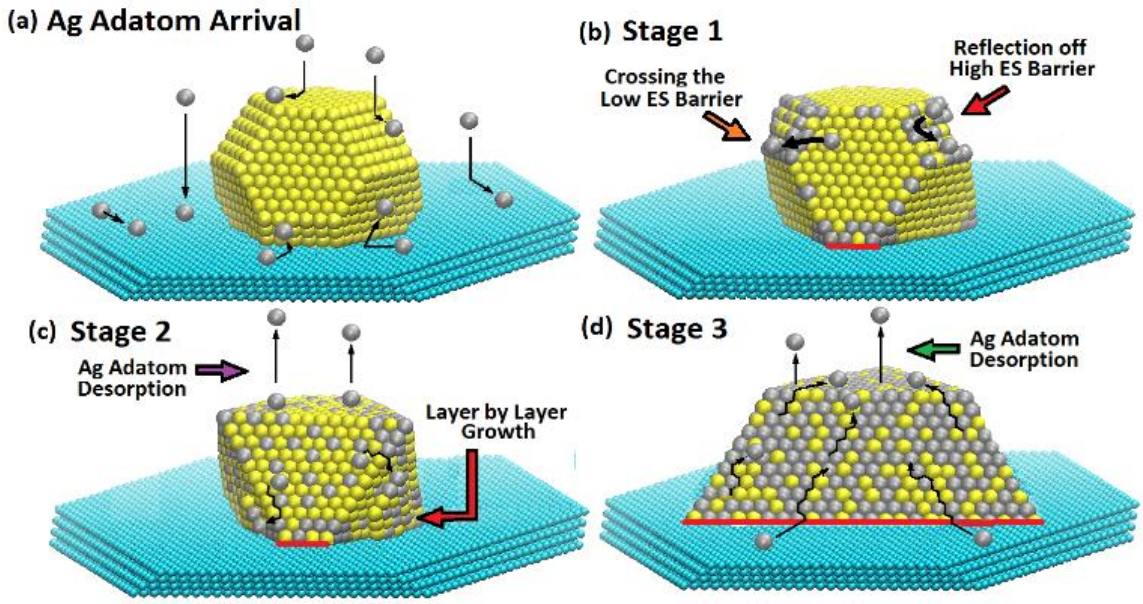

Figure 8.5 Schematic representation of the key elements which drive each of the three stages of the kinetically driven transformation of Wulff-shaped Au into triangular AuAg nanoprisms resulting from (a) the arrival of Ag adatoms to the template through direct impingement and surface diffusion. (b) Stage 1 processes where adatoms preferentially collect and deposit on {100} facets due to the varying Ehrlich-Schwoebel (ES) barriers. (c) Stage 2 processes where layer-by-layer growth is nucleated at the sites provided by the substrate-nanostructure interface where downward facing facets form and where Ag is increasingly desorbed from the top facet. (d) Stage 3 processes where adatoms arriving to the structure *via* substrate surface diffusion diffuse up the sidewalls to the nucleate growth on the top facet. Figure taken from 206.

of Au or Ag adatoms to their respective Wulff configurations drive the geometry towards a {111} faceted octahedron. While their simulations pertain to homogeneous nucleation, many of their theoretical arguments can be extended to the heterogeneous case.

For the Au nanostructure to maintain its equilibrium Wulff shape, it would require the isotropic attachment of Ag adatoms to the various facets. Anisotropies are, however, inherent to our assembly process. Ag atoms which sublimate from the foil can arrive to the Au nucleation site through direct impingement or by landing on the substrate and diffusing to its base. The latter process can lead to the preferential arrival of adatoms to those facets which intersect the substrate. Nanowire growth modes, for example, are often dominated

by the arrival of adatoms at the nanowire base from what is termed as the collection area.[213] Further anisotropies originate from the unique bonding environment which the (100) and (111) facets present to a Ag adatom. Adatoms on the (100) surfaces are bonded to four nearest neighbor Au atoms while those on the close-packed (111) surface are bonded to only three. As a result of the higher coordination and stronger bonding, adatom surface diffusion on the (100) facets is slower[214] and desorption is less probable. Adatom diffusion between the various facets is also subject to kinetic disruptions. For such a transfer to occur, the adatom must first relinquish bonds on one facet and then reform them on another. Such a process inevitably leads to an energy barrier, the so-called Ehrlich-Schwoebel barrier,[213,214] with a barrier height dependent on the particular facets involved. Because these barriers tend to reflect adatoms,[215] they present obstacles of varying degrees to the surface diffusion of adatoms between various facets. Significant reductions to the barrier height can, however, occur through exchange processes whereby an adatom assumes the position of a surface atom located at the facet edge in a manner which causes this surface atom to be displaced and promoted to the adjacent facet. When such a process is repeated over and over it can result in a directional diffusion of adatoms from one facet type to another. Significant is the fact that MD simulations of these various processes by Baletto *et al.*[212] for the case of homogeneous nucleation reveal that it is relatively easy for adatoms to cross from a (111) to a (100) facet, but not *vice versa*. The result, therefore, provides the mechanism by which adatoms become preferentially trapped on {100} facets. With this understanding of the kinetic anisotropies inherent to the assembly process, we propose a mechanistic framework by which the transformation from a Au Wulff shape to a AuAg

triangular nanoprism could occur. It is presented as a three stage process (**Figure 8.5**), but where it should be understood that there is a significant overlap between the stages.

In the first stage, Ag, which has arrived to the Au nucleation site, preferentially deposits on the high surface energy nucleation sites provided by the rounded regions and {100} facets (**Figure 8.5**). The rounded regions, which are characterized by step-terrace morphologies on atomic length-scales, sharpen because they present excellent nucleation sites for growth since adatoms can simultaneously form bonds to both the step and terrace. There is then preferential surface diffusion from the {111} to {100} facets which leads to the accumulation of Ag atoms in sufficient number to induce layer-by-layer growth on all {100} facets (**Figure 8.5**). Such processes proceed at relatively high rates until growth on {100} results in the formation of faceted pyramids enclosed by {111} facets (**Figure 8.5 c**). Concurrent with these processes is the bulk intermixing of Au and Ag *via* vacancy diffusion.

The second stage is dominated by slow layer-by-layer growth on the downward facing {111} facets and an overall reduction in the height of the structure. With only {111} facets remaining, preferential growth on downward facing facets is facilitated by the higher flux of Ag adatoms arriving from the adjacent collection area. It is also possible that the high contact angle formed between these three facets and the substrate provides a nucleation site from which layer-by layer growth is initiated. For the overall structure to lose height the top facet must be losing layers through the desorption of Ag at a rate greater than it is being replaced. At the end of this stage, the downward facing facets are filled in to complete the nanoprism geometry (**Figure 8.5 c**).

In the third stage, the nanoprism slowly gains height through layer-by-layer deposition on the top facet while the three side-facets grow, but at a much slower rate. This reversal from a gradual height loss to a gain is readily understood if the material required for this growth is being sourced from the collection area *via* the three remaining facets which are in contact with the substrate. At the beginning of the second stage the contact between these facets and the substrate is minimal (red line in **Figure 8.5 c**) and, as a result, they could not source enough material from the collection area to counterbalance the loss of Ag through desorption. It is noted that diffusion to the top facet *via* the downward facing facets is far less probable since these facets do not share an edge with the top facet and, as a result, surface diffusion from these facets to the top facet requires the adatom to cross a minimum of two Ehrlich-Schwoebel barriers.

By the end of second stage, however, the line of contact between the remaining facets and the substrate has more than tripled (red line in **Figure 8.5 d**), and in doing so, provides the ability to source many more adatoms from the substrate. With all three of these side facets now supplying adatoms to the top facets it is able to grow in a layer-by-layer manner (**Figure 8.5 d**). This growth, however, if offset by increasing Ag desorption as the structure increases in surface area and volume. The structure, therefore, trends toward a steady-state configuration where the number of Ag atoms arriving to the structure is balanced by number exiting. Thus far, the proposed mechanistic framework, as well as the MD simulations of Baletto *et al.*,[212] does not preclude the possibility of transforming homogeneous nucleation sites of Ag into Ag nanoprisms. Attempts to achieve this outcome were only partially successful since Ag nanoprisms formed in low yield and many of the nucleation sites experienced a net volume loss. All of the nucleation sites able to support

growth did, however, show a substantial sharpening of their facets. These results, hence, emphasize the important role which the far less volatile Au atoms play in stabilizing the nanoprism geometry.

8.7 Conclusions

We have demonstrated a method for transforming Au nanoparticles shaped as truncated octahedrons into AuAg triangular nanoprisms which are substrate-immobilized, single-crystalline, epitaxially aligned and surfactant-free. In the devised route, Au nanoparticles serve as heterogeneous nucleation sites for Ag adatoms sourced from a sublimating foil. The observed transformation was unexpected because the nanoprism geometry does not represent the low surface energy configuration which typically transpires in high temperature assembly processes reliant on solid state diffusion. This deviation from the norm is attributed to the anisotropies in kinetic processes associated with (i) adatoms arriving preferentially to the base of nucleation site from an adjacent collection area, (ii) higher adatom diffusion rates on {111} facets than on {100} facets, and (iii) the various Ehrlich–Schwoebel barriers which inhibit adatom motion between facets. These anisotropies combined with the constant arrival, desorption and interdiffusion of Ag into Au at the nucleation site leads to the non-equilibrium steady state nanoprism geometry which, upon cooling, maintains this ‘frozen-in’ configuration. Obtained in high yield from a relatively simple procedure, the so formed nanoprisms present the opportunity to form photonic surfaces for catalytic, sensing and photovoltaic applications. The optical properties of the nanostructures and the hydrogen sensing capabilities of Pd covered nanoprisms were also reported.

CHAPTER 9

HETEROGENEOUS CATALYSIS

***Preface**: This chapter discusses a series of unpublished investigations pertaining to the development of novel catalysts for the reduction of 4 – nitrophenol to 4 – aminophenol with sodium borohydride. The goal of this chapter is to provide an introduction to heterogeneous catalysis and brief overview of various catalytic modalities.*

9.1 Introduction

There is an extensive literature pertaining to the reduction of 4-nitrophenol (4-NP) to 4-aminophenol (4-NP) with sodium borohydride ($NaBH_4$) and metal nanoparticle catalysts. The widespread interest stems from the fact that this reaction stands with great technological relevance[216-218] while also serving as a model reaction for accessing a given catalytic platform.[219] A majority of the literature pertains to the development of colloidal nanoparticles (either supported or colloidal) whose morphology and/or composition are optimized[220] for catalytic activity, recoverability, recyclable, efficiency and/or economy.[221]

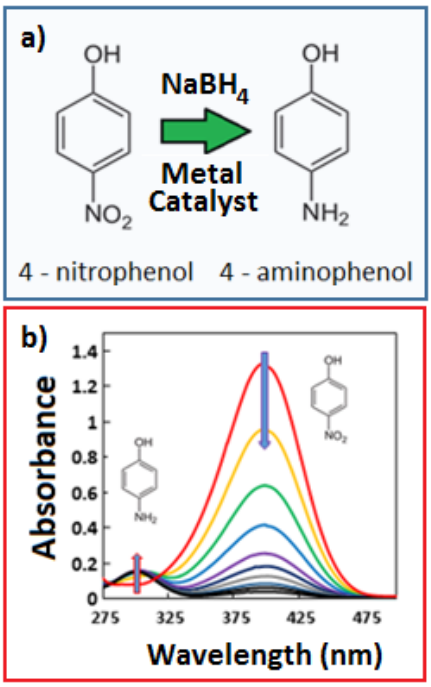

Figure 9.1 a) The reduction of 4-NP to 4-AP with $NaBH_4$ and metal catalyst. b) The change in the absorbance spectrum over time after addition of metal catalyst.

Herein presented is a series of novel catalytic platforms based on (i) substrate-based nanoparticles, (ii) mechanically induced nanotexturing of bulk copper foils, (iii) ultra-small AuPd surfactant-free colloidal nanoparticles synthesized via pulse laser, (iv) substrate-based AuCu nanoprisms and (v) the Wulff in a Cage Morphology. The catalytic activity is monitored through the reduction of 4 - NP to 4 - AP with $NaBH_4$.

9.2 The Model Catalytic Reaction

The reduction of 4 – NP to 4 – AP by $NaBH_4$ with a metal catalyst is considered a model reaction. Below is a list, generated by the Herve´s *et al.*, for what defines a ***model reaction***[219]:

(i) Only upon addition of the metal catalyst should the reaction start and transform chemical species A to B without side reactions or by-products.
(ii) The reaction rate should be determined as a function of temperature for a detailed understanding of the reaction mechanism.
(iii) The reaction should proceed under mild conditions, preferably at around room temperature and in mild solvents like water. No degradation or transformation of the nanomaterials should occur during the reaction.

9.3 The Reduction of 4 - Nitrophenol to 4 – Aminophenol

To reiterate, the reduction of 4 – NP to 4 – AP is shown in **Figure 9.1a**, where the nitrogroup is reduced to an amino group with $NaBH_4$ and a metal catalyst. In all experiments carried out herein; the reactions are carried out inside a quartz cuvette mounted inside a UV/Vis spectrometer. A 2 mL aqueous solution of 70 µM 4-NP and 7 mM $NaBH_4$ contained within a standard 1 cm path-length quartz cuvette. The reaction is monitored prior to the addition of catalyst to reveal a constant absorbance spectrum over time. The reaction is then initiated by the insertion/injection of the catalyst (i.e. colloidal nanoparticles, dip-catalyst, foil, etc.), the strong absorbance at 400 nm (representing the 4 – NP ions) begins to decrease and a peak emerges at 300 nm (representing the 4 – AP). Directly after adding the catalyst, an induction time may be observed, as shown in **Figure 9.2a,b** (orange dashed circle). The origin of the induction time is still under investigation but evidence points to surface reconstructions.[219] Directly after this induction time, the reaction ensues as a pseudo-first order reaction yielding 4-AP, a species which rapidly desorbs from the surface and is, hence, inconsequential to the reaction kinetics. The rate

limiting step is, therefore, the reaction occurring between the adsorbed hydrogen species and 4-NP on the metal catalyst. By tracking the absorbance at 400 nm (**Figure 9.2a**), the change in 4-NP may be monitored over time. Catalysts are typically described in terms of an apparent reaction rate, k_{app}, equal to the linear slope of the $\ln(A/A_0)$ *vs* t (*details discussed in 9.4 below*).

9.4 Determining the Apparent Reaction Rate

To determine the apparent rate of reaction, the absorbance at 400 nm is measured as a function of time (**Figure 9.2a**). The reaction behavior is governed by the pseudo first-order reaction where $d[A]/dt = k_{app}[A]$, where the [A] is the concentration of 4 - NP at a given time *t*. Since the concentration of $NaBH_4$ is 100-times greater than the 4-NP, this term is relatively constant and can be excluded from the rate equation. To obtain the constant k_{app}, the slope should be extracted from the plot of $\ln(A/A_o)$ vs. time, where t_o is after the induction period.[219]

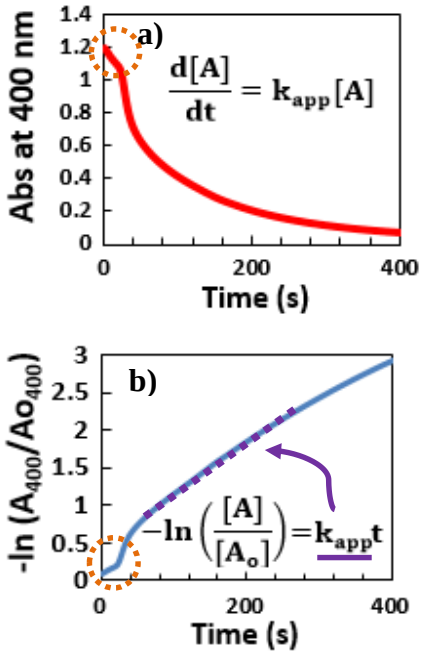

Figure 9.2 a) The absorbance of 4-NP at 400 nm as a function of time. b) A plot of $-\ln(A/A_o)$ vs. t where the purple dash line is used to determine the slope which is equal to k_{app}. The orange circle in a) and b) represents the induction time.

9.5 Catalytic Modalities

Introduced are five novel catalytic platforms which are still under investigation:

1. **Nanotrenches Induced by Shear Deformation** (Section 9.5.1)
2. **The Volmer-Weber Dip-Catalyst** (Section 9.5.2)
3. **AuCu Nanoprism Dip-Catalyst** (Section 9.5.3)
4. **Femtosecond laser pulses for Synthesis of AuPd Nanoparticles** (Section 9.5.4)
5. **The Wulff in a Cage** (Section 9.5.5)

9.5.1 Nanotrenches Induced by Shear Deformation

Bulk foils are generally considered to be inert and non-catalytic. Despite this well accepted paradigm, shown is the unprecedented activation of bulk copper foil directly after shear deformation. To understand how and why shear deformation results in this remarkable increase in activity, the surface morphology was investigated with SEM and AFM (**Figure 9.3a,b**). The surface of the annealed film is smooth (**Figure 9.3a**) and catalytic rate low, but, upon shearing, the edge regions form nanotrenches (**Figure 9.3b**). A remarkable (**10^2 - 10^3**) improvement in the catalytic rate is measured after shearing. The rate is shown to increase linearly with the number of cuts (**Figure 9.3c**), yet, perhaps the most remarkable aspect of this platform is the recyclability (**Figure 9.3d**). This remarkable dip-catalyst not only has one of the highest reported reaction rates but also has a remarkable recyclability and continues to work after 5 weeks. While extensive work is still required to pinpoint the mechanism, all clues point to enhancements attributed to the generation of nanotrenches or (nanoscaled concavity) which serve as an ideal environment for this reduction reaction.

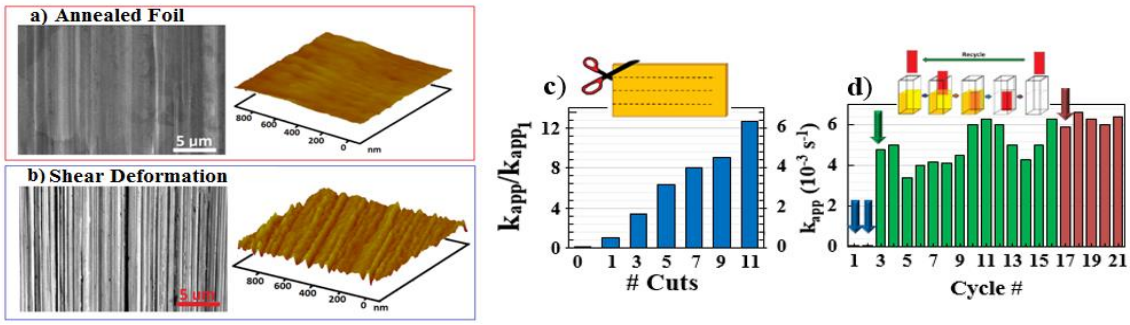

Figure 9.3 a) Shown is an SEM micrograph and a 3D – topographic AFM image of an annealed copper foil with a smooth surface. b) Upon shear deformation, micro- and nanoscaled trenches are observed with both SEM and AFM. c) Catalytic measurements were carried out as a function of the number of cuts made into the foil to reveal a linear dependence with the rate constant. d) The recyclability was also tested where the blue arrows show the rate of uncut foil (null) and the green bars are measurements from the shear deformed foil for week 1, and red bars for week 2.

9.5.2 The Volmer-Weber Dip-Catalyst

The Volmer-Weber Dip-Catalyst (VMDC) is a catalytic platform which has a metal (i.e. Au, Cu and Pd) sputter deposited onto SiO_2 substrates with varying thicknesses. The catalytic rate of each of these materials is studied as a function of deposition thickness. As an example of the growth process, Cu deposition is shown in **Figure 9.4 a – d,** where 1, 3, 5 and 10 nm are deposited and catalytically assessed at each stage of the growth. Adopted was a dip catalyst approach,[222-225] whereby the reaction is initiated by inserting the supported metal catalyst into a quartz cuvette containing the reactants. **Figure 9.4 e-g** shows the reaction rates obtained for the three metal catalysts as a function of their nominal thickness. The thickness at which the thin film comes together is marked for each material by a colored vertical line. Au and Pd show a dependency which indicates substantial catalytic activity for discrete nanoscale islands which diminishes rapidly in this range where nanoscale islands give way to a continuous film. Contrary to intuition (which sees

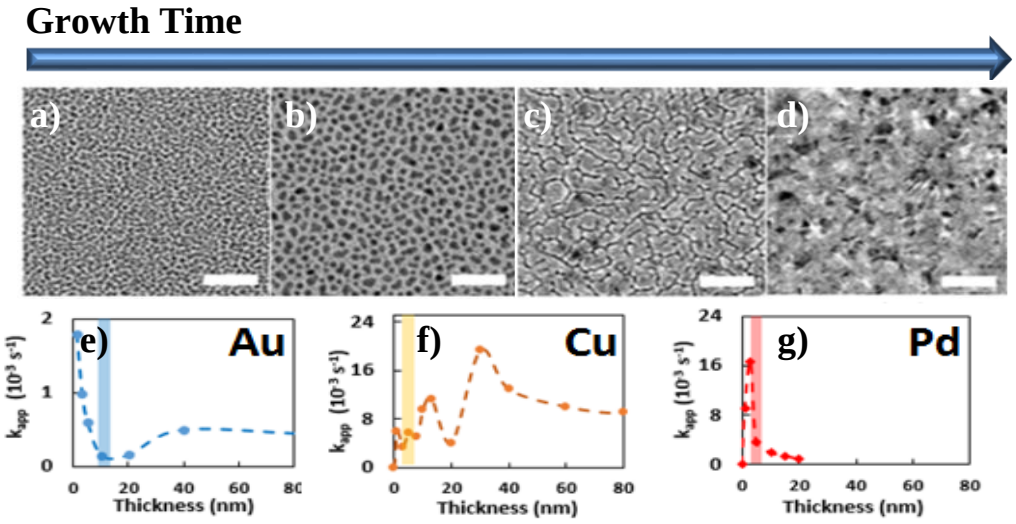

Figure 9.4 As a demonstration of the Volmer-Weber growth mode, shown are TEM micrographs of Cu with nominal thicknesses of 1, 3, 5 and 10 nm (a - d). The three plots below show the catalytic rates of e) Au, f) Cu and g) Pd as a function of thickness. The vertical blue, orange and red lines denote the thickness for where the film merges.

k_{app} decrease as the film goes toward bulk), Cu showed an oscillatory rate with film thickness. These observations, while exciting, need additional work and analysis.

9.5.3 AuCu Nanoprisms Dip-Catalyst

Here, assessed is the catalytic and photocatalytic properties of highly faceted, substrate-immobilized AuCu triangular nanoprisms (**Figure 9.5a**) synthesized using a vapor phase templated-assembly. The synthetic procedure is identical to what was discussed in **Chapter 8** but where a Cu-foil was used instead of a Ag-foil. The so-formed structures have a bimetallic composition which is well-recognized for its catalytic capabilities[226] as well as a strong localized surface plasmon resonance in the visible spectrum (**Figure 9.5b**). Using a dip catalyst modality (**Figure 9.5c**), the structures are demonstrated as heterogeneous photocatalysts with a 32-fold enhancement to the reaction rate when resonantly excited with 10 mW/cm^2 632.8 nm laser light, and smaller 4-fold enhancement with off resonant excitation at 532 nm. The study demonstrates the potential of such structures as photocatalysts and validates the reduction of 4-nitrophenol as a reaction useful in assessing the photocatalytic capabilities of plasmonic nanostructures. This work has been submitted for publication.[227]

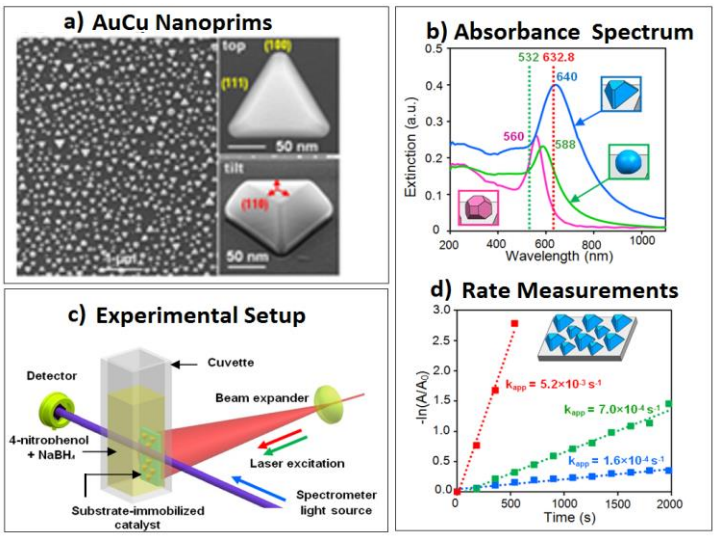

Figure 9.5 SEM images of (a) AuCu nanoprisms along with insets showing high resolution images of top- and side-views. (b) The optical absorbance spectra for Au templates (pink), AuCu triangular nanoprisms (blue) and near-hemispherical AuCu nanostructures (green). (c) Schematic representation of the experimental configuration used for photocatalysis measurements which sees the probe beam and the laser excitation source pass through the cuvette at right angles to each other. d) The time dependence of -ln(A/A$_0$) for AuCu nanoprisms where the dashed red and green lines denote the laser excitation wavelengths used for photocatalysis but where blue is measured in the dark.

9.5.4 Femtosecond Laser Pulses for Synthesis of AuPd Nanoparticles

It can be shown that the reduction rate of 4-nitrophenol (4NP) can be predicted purely based off of the binding energy between 4NP and the metal catalyst.[228] This prediction suggests that the ideal catalyst is one which is neither too reactive nor too noble but rather, "just right".[229] One of hallmarks of bimetallic nanoparticles is that the resulting properties are nearly a linear combination of the two pure metals.[229] Therefore, explored is the surfactant-free synthesis of Au-Pd bimetallic colloidal nanoparticles, with diameters of 2.4 ± 0.9 nm, through the use intense femtosecond laser pulses for the co-reduction of aqueous solutions of $[AuCl_4]^-$ and $[PdCl_4]^{2-}$ with varying ratios. A high resolution transmission electron microscope (TEM) image is shown in **Figure 9.6a.** Energy dispersive X-ray spectroscopy (EDX) mapping in **Figure 9.6a** indicates that the nanostructures consist of homogeneous mixture Au and Pd. The catalytic activity of the various precursor ratios were measured and plotted in 3D, **Figure 9.6b**. This work is currently being prepared for publication.

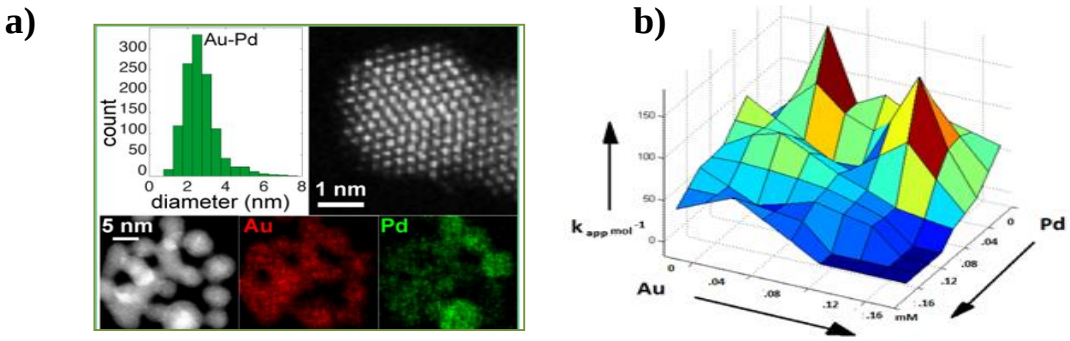

Figure 9.6 a) Shown is a histogram of the diameter-distribution of AuPd nanoparticles synthesized from the ultrashort laser pulse for a given Au-Pd precursor ratio. The high resolution TEM micrograph shows the single crystal nature of the derived nanoparticle. Directly beneath shows a series of particles with associated EDS maps to show individually elemental Au and Pd. b) A 3D plot showing the reduction rate of 4NP to 4AP with $NaBH_4$ all as a function of the precursor ratio.

9.5.5 The Wulff in a Cage

Having control over heterogeneous nucleation and galvanic replacement offers the opportunity to derive more intricate nanoparticle geometries such as the, "Wulff in a Cage". This structure is best described as a noble metal nanoparticle (in the low energy Wulff configuration) surrounded by a noble metal nanoframe or nanocage, depicted in **Figure 9.7**. Three cases are presented where (1) low amounts of Ag deposition onto the template results in edge deposition and subsequent galvanic replacement with Au^{3+} leads to the formation of the Wulff in a Frame morphology, (2) depositing a medium amount of Ag onto the template leads to edge and (100) deposition where the addition of Au^{3+} leads to a Wulff in a Cage morphology, and (3) high amounts of Ag deposition leads to complete and uniform coverage and the addition of Au^{3+} leads to a Wulff in a Shell morphology. The motivation for synthesizing such a structure comes from the fact that metal nanostructures, which exhibit ultra-small features (< 2 nm), show enhanced catalytic performance as evident from a recent publication.[230] The feasibility of carrying out such a synthesis has been varied in Figure 9.7 which shows SEM micrographs of Au templates, oriented with

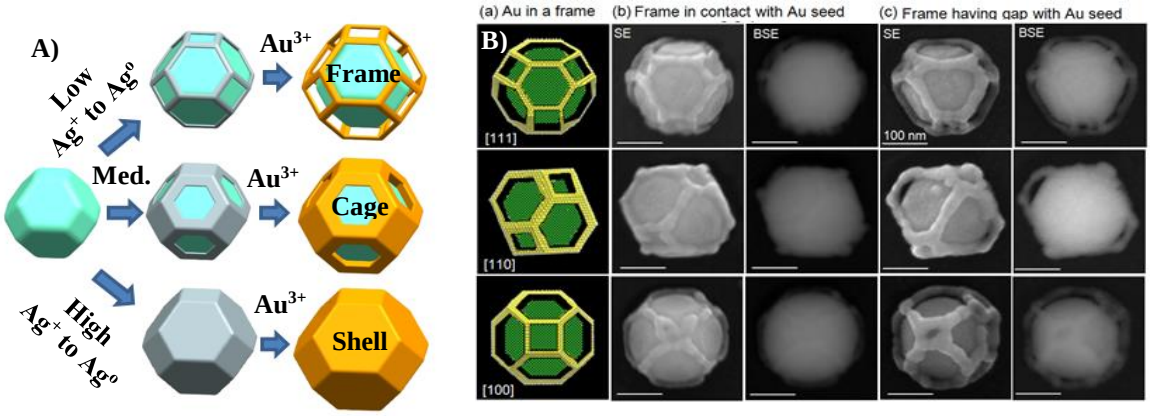

Figure 9.7 A) A schematic showing the reduction of low, medium and high concentrations of Ag^{+} resulting deposition on the edge, edge plus (100)-facet, and complete coverage, respectively. The subsequent galvanic replacement of the deposited Ag with Au^{3+} results in the formation of a frame, cage or shell for the low, medium and high concentrations, respectively. B) SEM micrographs show Au templates, oriented with [111], [110] and [100]-axis up, enveloped by an Au frame; a result from using low Ag^{+}.

[111], [110] and [100]-axis up, enveloped by an Au frame; a result from reducing low amounts of Ag^{+} and then galvanically replacing the Ag with Au^{3+}.

CONCLUDING REMARKS

In essence, this dissertation serves as a foundation for researchers interested in synthesizing highly ordered shape-tunable substrate-based plasmonic nanomaterials. This was accomplished by coupling novel thin-film methods (i.e. thermal dewetting, dynamic templating) with emerging solution-phase chemistry aimed at shape engineering metal nanoparticles. The experimental work discussed herein allows for the establishment of several important generalities regarding the governing mechanisms of shape engineering metallic nanoparticles.

The synthesis of nanoparticles which exhibit far-from-equilibrium morphologies (i.e. nanoshell, nanoprism, etc.), relies on chemical or physical processes which adds/removes atoms to/from a template structure in a manner which satisfies thermodynamic constraints outside from whole-structure free energy considerations. For example, the decrease in free energy occurring during galvanic replacement reactions, between the ions and template, occurs while the surface free energy, associated with the hollowing process, increases. It's important to point out that maintaining this far-from-equilibrium morphology relies on the fact that atoms cannot diffuse over the large length scales necessary to minimize the surface free energy of the overall nanostructure.

A similar generality can be made about heterogeneous nucleation carried out in what is considered *slow* kinetics. In this case, neutral species arrive to the template in the solution-phase but where solution-template barriers prevent uniform deposition. These barriers

create a situation which forces the nucleation and growth to occur at a single site on the template. The continual growth from this single site creates a situation which, as discussed previously, increases the surface free energy of the overall structure. Therefore, in both cases (galvanic replacement and heterogeneous nucleation), atoms deposit in a manner which produces an overall morphology which deviates significantly from the equilibrium shape. Also, in each case, the atoms do not possess the necessary energy to reorganize into the equilibrium shape.

Therefore, the morphology of kinetically controlled products can be tuned by establishing predefined energy barriers which can include (i) solution-template barriers (*transition from solution-phase species to adatom*) by the presence of electrical double layers or ligands, or (ii) an anisotropic surface-energy landscape (i.e. defects, edges, facets, surfactants/ligands). Therefore, both the initial shape of the template and preadsorbed chemical species can be used to drive growth toward a desired morphology.

On the other hand, the synthesis of a nanoparticles with an equilibrium morphology is generally straightforward. This can be established simply by providing the nanostructure the necessary time and energy for unstable atoms to overcome kinetic barriers (probe the potential field) and settle into positions which minimizes the particle's overall surface energy. The intrinsic surface energy anisotropy of the FCC crystals causes the resultant shape to evolve toward the Wulff configuration. However, this surface energy anisotropy may be modulated through the addition of surface agents or ligands which can bind to specific facets to lower their surface energy, hence modulating the low energy configuration.

The growing body of literature related to the synthesis of metal nanostructures has come a long way since the early work provided by Faraday and Turkevich. Despite the many advancements to synthetic protocols and characterization techniques, our understanding of the atomic scale mechanisms involved is far from complete. The ability to understand how these materials behave at the atomic level will ultimately allow us to exploit this knowledge in order to design and engineer idealized nanostructures for a given application.

In summary, the powerful combination of solution-phase chemistry and thermal self-assembly along with the understanding of the roles played by kinetics and thermodynamics, has resulted in series of substrate-based nanomaterials including (i) Au - Ag – nanohuts, nanocages and nanoshells, (ii) Pt nanoshells derived from Ni, Co, Pb, Ag and Cu template materials, (iii) alloying/interdiffusion regulated by template induced strain, (iv) Au@Ag, Au – Ag heterostructures and Au – Ag dimer structures and (v) Au-Ag and Au-Cu nanoprisms. Devised routes have resulted in a number of mechanistic discoveries including (i) passivation-layer induced tunneling during galvanic replacement reactions, (ii) insights into how atoms exit during galvanic replacement carried out on passivated templates, (iii) crystal growth modes kinetically controlled via precursor concentration and injection rate, (iv) the formation of nanotrenches via shear deformation and (v) the remarkable catalytic rates for the reduction of 4-nitrophenol to 4-aminophenol with $NaBH_4$ with Cu nanotrenches.

PUBLICATIONS OF KDG

1. **Gilroy, K. D.**; Hughes, R. A.; Neretina, S. The Volmer Weber Growth Dip Catalyst, **2015**, ***In Prep***.
2. **Gilroy, K. D.**; Hughes, R. A.; Neretina, S. Enhanced Catalytic Properties of Bulk Cu after Nanotexturing via Shear Deformation, **2015,** ***In Prep***.
3. **Gilroy, K .D.**; Hughes, R. A. Neretina, S., Synthesis and Applications of Wulff in a Cage Nanoparticle, **2015,** ***In Prep***.
4. Hajfathalien, M.; **Gilroy, K. D.**; Hughes, R. A. Neretina, S., Synthesis of Substrate-based Au – Ag Nanoprisms through Heterogenenous Nucleation, **2015,** ***In Prep***.
5. Sil, D.; Tibbetts, K. M.; Odhner, J. H.; **Gilroy, K. D.**; Neretina, S.; Levis, R. J.; Borguet, E. Ultrashort Laser Pulses Generate Narrowly Distributed Sub-5 nm Surfactant-Free Au-Pd Nanoparticles, **2015**, ***In Prep***.
6. Hajfathalian, M; **Gilroy, K. D.**; Yaghoubzade, A.; Sundar, A.; Teng, T.; Hughes, R. A. Neretina, S. Photocatalytic Enhancements to the Reduction of 4-Nitrophenol by Resonantly Excited Triangular Gold-Copper Nanoprisms, **2015**, ***Submitted***.
7. **Gilroy, K. D.**; Sundar, A.; Hajfathalian, M, A.; Yaghoubzade, A.; Tan, T.; Sil, D.; Borguet, E.; Hughes, R. A.; Neretina, S. Transformation of Truncated Gold Octahedrons into Triangular Nanoprisms through the Heterogeneous Nucleation of Silver, *Nanoscale* **2015**, 7 (15), 6827-6835.
8. **Gilroy, K. D.**; Hughes, R. A.; Neretina, S. Kinetically Controlled Nucleation of Silver on Surfactant-Free Gold Seeds, *Journal of the American Chemical Society* **2014,** 136 (43), 15337–15345.
9. Sil, D.; **Gilroy, K. D.**; Boulesbaa, A.; Neretina, S.; Borguet, E. Seeing is believing: Hot Electron based Gold Nanoplasmonic Optical Hydrogen Sensor, *ACS Nano* **2014**, 8, 7755–7762.
10. Senel Ayaz, H. G.; Perets, A.; Ayaz, H.; **Gilroy, K. D.**; Govindaraj, M.; Brookstein, D.; Lelkes, P. Textile-templated Electrospun Anisotropic Scaffolds for Regenerative Cardiac Tissue Engineering, *Biomaterials* **2014**, 35, 8540-8552.
11. **Gilroy, K. D.**; Farzinpour, P.; Sundar, A.; Hughes, R. A.; Neretina, S. Sacrificial Templates for Galvanic Replacement Reactions: Design Criteria for the Synthesis of Pure Pt Nanoshells with a Smooth Surface Morphology, *Chemistry of Materials* **2014**, 26, 3340-3347.
12. Sundar, A.; Farzinpour, P.; **Gilroy, K. D.**; Teng T.; Hughes, R. A.; Neretina, S. Eutectic Combinations as a Pathway to the Formation of Substrate-Based Au-Ge Heterodimers and Hollowed Au Nanocrescents with Tunable Optical Properties, *Small* **2014**, 10, 3379-3388.
13. **Gilroy, K. D.**; Neretina, S.; Sanders, R. W. Bioaccumulation of Gold Nanoparticles in an Experimental Algal-zooplankton Food Chain, *Journal of Nanoparticle Research* **2014**, 16, 1-8.
14. **Gilroy, K. D.**; Farzinpour, P., Sundar, A., Tan, T.; Hughes, R. A.; Neretina, S, Mechanistic Study of Substrate-based Galvanic Replacement Reactions, *Nano Research* **2014**, 7, 365-379.
15. Sundar, A.; Farzinpour, P.; **Gilroy, K. D.**; Tan, T.; Hughes, R. A.; Neretina, S, Organized Surfaces of Highly Faceted Single-crystal Palladium Structures Seeded by Sacrificial Templates, *Crystal Growth Design* **2013**, 13, 3847-3851.
16. **Gilroy, K. D.**; Farzinpour, P.; Sundar, A.; Tan, T.; Hughes, R. A.; Neretina, S. Substrate-based Galvanic Replacement Reactions Carried out on Heteroepitaxially formed Silver Templates, *Nano Research* **2013**, 6, 418-428.
17. Farzinpour, P.; Sundar, A.; **Gilroy, K. D.**; Hughes, R. A.; Neretina, S. Dynamic templating: A Large Area Processing Route for the Assembly of Periodic Arrays of Sub-micrometer and Nanoscale Structures, *Nanoscale* **2013**, 5, 1929-1938.
18. Farzinpour, P.; Sundar, A., **Gilroy, K. D.**; Eskin, Z. E.; Hughes, R. A., Neretina, S, Altering the Dewetting Characteristics of Ultrathin Gold and Silver Films using a Sacrificial Antimony Layer, *Nanotechnology* **2012**, 23, *495604*.
19. Sundar, A.; Hughes, R. A., Farzinpour, P.; **Gilroy, K. D.**; Devenyi, G. A.; Preston, J. S.; Neretina, S. Manipulating the Size Distribution of Supported Gold Nanostructures, *Applied Physics Letters* **2012**, 100, 013111.

REFERENCES CITED

[1] Astruc, D. Nanoparticles and Catalysis, *Wiley-VCH*, **2008,** 1.

[2] Faraday, M. On The Color of Colloidal Gold, Phil. *Trans. R. Soc. Lond.*, **1857**, 145.

[3] Beischer, D.; Krause, F. Das Elektronenmikroskop als Hillsmittel der Kolloidfors, *Naturwissenschaften* **1937**, 25, 825.

[4] Turkevich, J.; Stevenson, P. C.; Hillier, A Study of the Nucleation and Growth Processes in the Synthesis of Colloidal Gold, J. *Discuss. Faraday Soc.* **1951**, 11, 55.

[5] Turkevich, J.; Garton, G.; Stevenson, P. C. The Color of Colloidal Gold, *J. Colloid Sci.* **1954**, 26.

[6] Tao, A. R.; Habas, S.; Yang P. Shape Control of Colloidal Metal Nanocrystals, *Small* **2008**, 4, 310.

[7] Daniel, M.C.; Astruc, D. Gold Nanoparticles: Assembly, Supramolecular Chemistry, Quantum-Size-Related Properties, and Applications toward Biology, Catalysis, and Nanotechnology, *Chem. Rev.* **2004**, 104, 293.

[8] Xiong, Y.; Lu, X. Metallic Nanostructures: From Controlled Synthesis to Applications, *Springer*, **2015**.

[9] Abbaschian, R.; Abbaschian, L.; Reed-Hill, R. E. Physical Metallurgy Principles, 4th Edition, *Cengage Learning*, **2008**.

[10] Neouze, M-. A.; Schubert, U. Surface Modification and Functionalization of Metal and Metal Oxide Nanoparticles by Organic Ligands, *Monatsh. Chem.* **2008**, 139, 183.

[11] Derjaguin, B.V.; Landau, E.M. Theory of the Stability of Strongly Charged Lyophobic Sols and of the Adhesion Of Strongly Charged Particles in Solution Of

Electrolytes, *Acta Physicochim., URSS*. **1941**, 14, 633.

[12] Venvey, E.J.W.; Overbeek, J.Th.G. Theory of the Stability of Lyophobic Colloids, Elsevier, **1948**.

[13] Sun, Y.; Xia, Y. Shape-Controlled Synthesis of Gold and Silver Nanoparticles, *Science* **2002**, 298, 2176.

[14] Jin, R.; Cao, Y. C.; Hao, E.; Métraux, G. S.; Schatz, G. C.; Mirkin, C. A. Controlling Anisotropic Nanoparticle Growth Through Plasmon Excitation, *Nature* **2003**, 425, 487.

[15] Grzelczak, M.; Liz-Marzan, L. M. The Relevance of Light in the Formation of Colloidal Metal Nanoparticles, *Chem. Soc. Rev.* **2014**, 43, 2089.

[16] Lim, B.; Kobayashi, H.; Yu, T.; Wang, J.; Kim, M. J.; Li, Z.-Y.; Rycenga, M.; Xia, Y. Synthesis of Pd-Au Bimetallic Nanocrystals via Controlled Overgrowth, *J. Am. Chem. Soc.* **2010**, 132, 2506.

[17] De Mongeot, F. B.; Valbusa, U. Surface Nanopatterns Induced by Ion-beam Sputtering, *J. Phys. Condens. Matter*. **2009**, 21, 220301.

[18] Ashkarran, A. A. Metal and Metal Oxide Nanostructures Prepared by Electrical Arc Discharge Method in Liquids, *J. Cluster Sci*. **2011**, 22, 233.

[19] Semaltianos, N. G. Nanoparticles by Laser Abalation, *Crit. Rev. Solid State Mater. Sci.* **2010**, 35, 105.

[20] Dai, Z. R.; Pan, Z. W.; Wang, Z. L. Novel Nanostructures of Functional Oxides Synthesized by Thermal Evaporation, *Adv. Funct. Mater*. **2003**, 13, 9.

[21] Botman, A.; Mulders, J. J. L.; Hagen, C. W. Creating Pure Nanostructures From

Electron-Beam-Induced Deposition Using Purification Techniques: A Technology Perspective, *Nanotechnology* **2009**, 20, 372001.

[22] Seipenbusch, M.; Binder, A. Structural Stabilization of Metal Nanoparticles by Chemical Vapor Deposition-Applied Silica Coatings, *J. Phys. Chem. C* **2009**, 113, 20606.

[23] George, S. M. Atomic Layer Deposition: An Overview, *Chem. Rev.* **2010**, 110, 111.

[24] Koch, R. Stress in Evaporated and Sputtered Thin Films – A Comparison, *Surf. Coat. Tech.* **2010**, 204, 1973.

[25] Thompson, C. V. Structure Evolution during Processing of Polycrystalline Films, *Annu. Rev. Mater. Sci.* **2000**, 30, 159.

[26] Barth, J. V.; Costantini, G.; Kern, K. Engineering Atomic and Molecular Nanostructures at Surfaces, *Nature* **2005**, 437, 671.

[27] Zhang, Z.; Lagally, M. G. Atomistic Processes in the Early Stages of Thin-Film Growth, *Science* **1997**, 276, 377.

[28] Baskaran, A.; Smereka, P. Mechanisms of Stranski-Krastanov Growth, *J. Appl. Phys.* **2012**, 111, 044321.

[29] Farzinpour, P.; Sundar, A.; Gilroy, K. D.; Hughes, R. A.; Neretina, S. Dynamic templating: A Large Area Processing Route for the Assembly of Periodic Arrays of Sub-micrometer and Nanoscale Structures, *Nanoscale* **2013**, 5, 1929.

[30] Zhang, Z.; Li, H.; Zhang, F.; Wu, Y.; Guo, Z.; Zhou, L.; Li, J. Investigation of Halide-Induced Aggregation of Au Nanoparticles into Spongelike Gold, *Langmuir* **2014**, 30, 2648.

[31] Nam, J.; Won, N.; Jin, H.; Chung, H.; Kim, S. pH-Induced Aggregation of Gold Nanoparticles for Photothermal Cancer Therapy, *J. Am. Chem. Soc.* **2009**, 131, 13639.

[32] Hamner, K. L.; Maye, M. M. Thermal Aggregation Properties of Nanoparticles Modified with Temperature Sensitive Copolymers, *Langmuir* **2013**, 29, 15217.

[33] Yang, D.; Ma, J.; Gao, M.;, Peng, M.; Luo, Y.; Hui, W.; Chen, C.; Wang, Z.; Cui, Y. Suppression of Composite Nanoparticle Aggregation Through Steric Stabilization and Ligand Exchange for Colorimetric Protein Detection, *RSC Adv.* **2013**, 3, 9681.

[34] Lee, J- W.; Klajn, R. Dual-Responsive Nanoparticles That Aggregate Under the Simultaneous Action of Light and CO_2, *Chem. Commun.* **2015**, 51, 2036.

[35] Li, D.; Wang, C.; Tripkovic, D.; Sun, S.; Markovic, N. M.; Stamenkovic, V. R. Surfactant Removal for Colloidal Nanoparticles from Solution Synthesis: The Effect on Catalytic Performance, *ACS Catal*. **2012**, 2, 1358.

[36] Aruda, K. O.; Tagliazucchi, M.; Sweeney, C. M.; Hannah, D. C.; Schatz, G. C.; Weiss, E. A. Identification Of Parameters Through which Surface Chemistry Determines the Lifetimes Of Hot Electrons in Small Au Nanoparticles, *PNAS* **2013**, 110, 4212.

[37] Bamwenda, G. R.; Tsubota, S.; Nakamura, T.; Haruta, M. The Influence of the

Preparation Methods on the Catalytic Activity of Platinum and Gold Supported on TiO_2 for CO Oxidation, *Catal. Lett.* **1997**, 44, 83.

[38] Widmann, D.; Behm, R. J. Activation of Molecular Oxygen and the Nature of the Active Oxygen Species for CO Oxidation on Oxide Supported Au Catalysts, *Accounts Chem. Res.* **2014**, 47, 740.

[39] Xu, H.; Cui, L. L.; Tong, N. H.; Gu, H. C. Development of High Magnetization Fe_3O_4/polystyrene/silica Nanospheres via Combined Miniemulsion/emulsion Polymerization, *J. Am. Chem. Soc.* **2006**, 128, 15582.

[40] Hariprasad, E.; Radhakrishnan, T. P. A Highly Efficient and Extensively Reusable "Dip Catalyst" Based on a Silver-Nanoparticle-Embedded Polymer Thin Film, *Chem. Eur. J.* **2010**, 16, 14378.

[41] Zheng, G.; Polavarapu, L.; Liz-Marzan, L. M.; Pastoriza-Santos, I.; Perez-Juste, J. Gold Nanoparticle-Loaded Filter Paper: A Recyclable Dip-Catalyst For Real-Time Reaction Monitoring By Surface Enhanced Raman Scattering, *Chem. Commun.* **2015**, 51, 4572.

[42] Vernon, K. C.; Funston, A. M.; Novo, C.; Gomez, D. E.; Mulvaney, P.; Davis, T. J. Influence of Particle-Substrate Interaction on Localized Plasmon Resonances, *Nano Lett.* **2010**, 10, 2080.

[43] Novo, C.; Funston, A. M.; Gooding, A. K.; Mulvaney, P. Electrochemical Charging of Single Gold Nanorods, *J. Am. Chem. Soc.* **2009**, 131, 14664.

[44] Sil, D.; Gilroy, K. D.; Boulesbaa, A.; Neretina, S.; Borguet, E. Seeing is Believing: Hot Electron based Gold Nanoplasmonic Optical Hydrogen Sensor, *ACS Nano* **2014**, 8, 7755.

[45] Christopher, P.; Xin, H.; Linic, S. Visible-Light-Enhanced Catalytic Oxidation Reactions on Plasmonic Silver Nanostructures, *Nat. Chem.* **2011**, 3, 467.

[46] Sun, M.; Xu, H. A Novel Application of Plasmonics: Plasmon-Driven Surface-Catalyzed Reactions, *Small* **2012**, 8, 2777.

[47] Mubeen, S.; Lee, J.; Singh, N.; Kramer, S.; Stucky, G. D.; Moskovits, M. An Autonomous Photosynthetic Device in which all Charge Carriers Derive from Surface Plasmons, *Nature Nanotech.* **2013**, 8, 247.

[48] Anker, J. N.; Hall, W. P.; Lyandres, O.; Shah, N. C.; Zhao, J.; Van Duyne, R. P. Biosensing with Plasmonic Nanosensors, *Nature Mater.* **2008**, 7, 442.

[49] Jain, P. K.; El-Sayed, I. H.; El-Sayed, M. A. Au Nanoparticles Target Cancer, *Nanotoday* **2007**, 1, 18.

[50] Nie, S.; Emory. S. R.; Probing Single Molecules and Single Nanoparticles by Surface-Enhanced Raman Scattering, *Science* **1997**, 21, 1102.

[51] El-Sayed, M. A.; Nikoobakht, B. Preparation and Growth Mechanism of Gold Nanorods (NRs) Using Seed-Mediated Growth Method, *Chem. Mater*. **2003**, 15, 1957.

[52] Reineck, P.; Lee, G. P.; Brick, D.; Karg, M.; Mulvaney, P.; Bach, U. A Solid-State Plasmonic Solar Cell via Metal Nanoparticle Self-Assembly, *Adv. Mater*. **2012**, 24, 4750.

[53] Roduner, E. Size Matters: Why Nanomaterials are Different, *Chem. Soc. Rev.* **2006**, 35, 583.

[54] Zhang, H.; Jin, M.; Xiong, Y.; Lim, B.; Xia, Y. Shape-Controlled Synthesis of Pd Nanocrystals and Their Catalytic Applications, *Acc. Chem. Res.* **2012**, 46, 1783.

[55] Sinfelt, J. H. Supported Bimetallic-cluster Catalysts, *J. Catal.* **1973**, 29, 308.

[56] Gschneidner, K.; Russell, A.; Pecharsky, A; Morris, J.; Zhang, Z. H.; Lograsso, T.; Hsu, D.; Lo, C. H. C.; Ye, Y. Y.; Slager, A.; Kesse, D. A Family of Ductile Intermetallic Compounds, *Nature Mater.* **2003**, 2, 587.

[57] Krenke, T.; Duman, E.; Acet, M.; Wassermann, E. F.; Moya, X.; Manosa, L.; Planes, A. Inverse Magnetocaloric Effect In Ferromagnetic Ni–Mn–Sn Alloys, *Nature Mater.* **2005**, 4, 450.

[58] Hao, R.; Xing, R.; Xu, Z.; Hou, Y.; Gao, S.; Sun, S. Synthesis, Functionalization, and Biomedical Applications of Multifunctional Magnetic Nanoparticles, *Adv. Mater.* **2010**, 22, 2729.

[59] Sealy, C. The problem with platinum, *Materialstoday* **2008**, 37 65.

[60] Vitos, L.; Ruban, A. V.; Skriver, H. L.; Kollar, J. The Surface Energy of Metals, *Surf. Sci.* **1998**, 411, 186.

[61] Gibbs, J. W. The Collected Works of Gibbs, Yale University Press, **1957**.

[62] Thompson, C. V. Solid-State Dewetting of Thin Films, *Annu. Rev. Mater. Res.* **2012**, 42, 399.

[63] Titolo, W. D. A Short History of Electrochemistry, *Galvanotechtnik* **2005**, 96, 1820.

[64] Zoski, C. G. Handbook of Electrochemistry, *Elsevier* **2007**.

[65] Harris, D. C. Quantitative Chemical Analysis, 7th, W. H. Freeman and Co. New York, **2006**, AP20.

[66] Xia, X.; Wang, Y.; Ruditskiy, A.; Xia, Y. 25th Anniversary Article: Galvanic Replacement: A Simple and Versatile Route to Hollow Nanostructures with Tunable and Well-Controlled Properties, *Adv. Mater.* **2013**, 25, 6313.

[67] Burda, C.; Chen, X. B.; Narayanan, R.; El-Sayed, M. A. Chemistry and Properties of Nanocrystals of Different Shapes, *Chem. Rev.* **2005**, 105, 1025.

[68] Xia, Y.; Xiong, Y. J.; Lim, B.; Skrabalak, S. E. Shape-Controlled Synthesis of Metal Nanocrystals: Simple Chemistry Meets Complex Physics, *Angew. Chem. Int. Edit.* **2009**, 48, 60.

[69] Jiang, X. C.; Yu, A. B. Low Dimensional Synthesis, Growth Mechanism, Properties and Applications, *J. Nanosci. Nanotechno.* **2010**, 10, 7829.

[70] Meng, X. K.; Tang, S. C.; Vongehr, S. A Review on Diverse Silver Nanostructures, *J. Mater. Sci. Tech.* **2010**, *26*, 487.

[71] Rycenga, M.; Cobley, C. M.; Zeng, J.; Li, W. Y.; Moran, C. H.; Zhang, Q.; Qin, D.; Xia, Y. Controlling the Synthesis and Assembly of Silver Nanostructures for Plasmonic Applications, *Chem. Rev.* **2011**, 111, 3669.

[72] Dement'eva, O. V.; Rudoy, V. M. Colloidal Synthesis of New Silver-Based Nanostructures with Tailored Localized Surface Plasmon Resonance, *Colloid J.* **2011**, 73, 726.

[73] Cobley, C. M.; Xia, Y. Engineering the Properties of Metal Nanostructures *via* Galvanic Replacement Reactions, *Mater. Sci. Eng. R* **2010**, 70, 44.

[74] Skrabalak, S. E.; Au, L.; Li, X.; Xia, Y. Facile Synthesis of Ag Nanocubes and Au Nanocages, *Nature Protoc.* **2007**, 2, 2182.

[75] Sun, Y.; Mayers, B.; Xia, Y. Template-Engaged Replacement Reaction: A One-Step Approach to the Large-Scale Synthesis of Metal Nanostructures with Hollow Interiors, *Nano Lett.* **2002**, 2, 481.

[76] Yin, Y; Erdonmez C; Aloni, S; Alivisatos, A. P. Faceting of Nanocrystals during

Chemical Transformation: From Solid Silver Spheres to Hollow Gold Octahedral, *J. Am. Chem. Soc*. **2006**, 128, 12671.

[77] Zhang, Q.; Xie, J. P.; Lee, J. Y.; Zhang, J.; Boothroyd, C. Synthesis of Ag@AgAu Metal Core/alloy Shell Bimetallic Nanoparticles with Tunable Shell Compositions by a Galvanic Replacement Reaction, *Small* **2008**, 4, 1067.

[78] Lu, X.; Tuan, H.-Y.; Chen, J.; Li, Z.-Y; Korgel, B. A.; Xia, Y. Mechanistic Studies on the Galvanic Replacement between Multiply Twinned Particles of Ag and $HAuCl_4$ in an Organic Medium, *J. Amer. Chem. Soc*. **2007**, 129, 1733.

[79] Camargo, P. H. C.; Xiong, Y.; Ji, L.; Zuo, J. M.; Xia, Y. Facile Synthesis of Tadpole-Like Nanostructures Consisting of Au Heads and Pd Tails, *J. Am. Chem. Soc.* **2007**, 129, 15452.

[80] Seo, D.; Song, H. Asymmetric Hollow Nanorod Formation through a Partial Galvanic Replacement Reaction, *J. Am Chem. Soc.* **2009**, 131, 18210.

[81] Yu, Y.; Zhang, Q.; Xie, J.; Lee, J. Y. Engineering the Architectural Diversity of Heterogeneous Metallic Nanocrystals, *Nat. Commun.* **2013**, 4, 1454.

[82] Personick, M. L.; Langille, M. R.; Zhang J.; Mirkin, C. A. Shape Control of Gold Nanoparticles by Silver Underpotential Deposition, *Nano Lett.* **2011**, 11, 3394.

[83] Linic, S.; Aslam, U.; Boerigter, C.; Morabito, M. Photochemical Transformations on Plasmonic Metal Nanoparticles, *Nat. Mater.* **2015**, 14, 567.

[84] Sanz, J. M.; Ortiz, D.; Alcaraz de la Osa, R.; Saiz, J. M.; Gonzalez, F.; Brown, A. S.; Losurdo, M.; Everitt, H. O.; Moreno, F. UV Plasmonic Behavior of Various Metal Nanoparticles in the Near and Far-Field Regimes: Geometry and Substrate Effects, *J. Phys. Chem. C* **2013**, 117, 19606.

[85] Willets, K. A.; Van Duyne, R. P. Localized Surface Plasmon Resonance Spectroscopy and Sensing, *Annu. Rev. Phys. Chem.* **2007**, 58, 267.

[86] Cortie, M. B.; McDonagh, A. M. Synthesis and Optical Properties of Hybrid and Alloy Plasmonic Nanoparticles, *Chem. Rev.* **2011**, 111, 3713.

[87] Kreibig, U.; Fragstein, C. The Limitation of Electron Mean Free Path in Small Silver Particles, *Z. Physik* **1969**, 224, 307.

[88] Kreibig, U.; Vollmer, M. Optical Properties of Metal Clusters, *Springer* **1995**.

[89] Dang, T. M. D.; Le, T. T. T.; Fribourg-Blanc, E.; Dang, M. C. Synthesis and Optical Properties of Copper Nanoparticles Prepared By a Chemical Reduction Method, *Adv. Nat. Sci. Nanosci. Nanotechnol.* **2011**, 2, 015009.

[90] Link, S.; Wang, Z. L.; El-Sayed, M. A. Alloy Formation of Gold-Silver Nanoparticles and the Dependence of the Plasmon Absorption on Their Composition, *J. Phys. Chem. B* **1999**, 103, 3529.

[91] Rakić, A. D.; Djurišic, A. B.; Elazar, J. M.; Majewski, M. L. Optical properties of Metallic Films for Vertical-Cavity Optoelectronic Devices, *Appl. Opt*. **1998**, 37, 5271.

[92] Kelly, K. L.; Coronado, E.; Zhao, L. L.; Schatz, G. C. The Optical Properties of Metal Nanoparticles: The Influence of Size, Shape, and Dielectric Environment, *J. Phys. Chem. B* **2003**, 107, 668.

[93] Noguez, C. Surface Plasmons on Metal Nanoparticles: The Influence of Shape and Physical Environment, *J. Phys. Chem. C* **2007**, 111, 3806.

[94] Talapin, D. V.; Shevchenko, E. V. Dipole−Dipole Interactions in Nanoparticle Superlattices, *Nano Lett.*, **2007**, 7, 1213.

[95] Taflove, A; Hagness, S. C. Computational Electrodynamics: The Finite Difference time Domain Method, Boston, MA: Artech House, **2005**, 3rd Ed.

[96] Lorentz, H. A. Theory of Electrons, Teubner, Leipzig, **1909**.

[97] DeVoe, H. Optical Properties of Molecular Aggregates. I. Classical Model of Electronic Absorption and Refraction, *J. Chem. Phys.* **1964**, 41, 393.

[98] Purcell, E. M.; Pennypacker, C. R. Scattering and Absorption of Light by Nonspherical Dielectric Grains, *Astrophysical Journal* **1973**, 186, 705.

[99] Draine, B. T.; Flatau, P.J. Discrete Dipole Approximation for Scattering Calculations, *J. Opt. Soc. Am. A* **1994**, 11, 1491.

[100] Hao, E.; Schatz, G. C.; Hupp, J. T. Synthesis and Optical Properties of Anisotropic Metal Nanoparticles, *J. Fluoresc.* **2004**, 14, 331.

[101] Haugstad, G. Atomic Force Microscopy: Understanding Basic Modes and Advanced Applications, *John Wiley & Sons*, **2012**.

[102] Abbe, E. Beiträge zur Theorie des Mikroskops und der Mikroskopischen Wahrnehmung, *Arch. Mikrosk. Anat*. **1873**, 9, 413.

[103] Lipson, A.; Lipson, S. G.; Tannhauser, D. S. *Optical Physics*. United Kingdom: Cambridge. **1998**, 340.

[104] Hecht, E. Optics, 4th Edition, *Pearson*, **2008**.

[105] William, D. B.; Carter, C. B. Transmission Electron Microscopy, 2nd Edition, *Springer* **2009**.

[106] Goodhew, P. J.; Humphreys, J.; Beanland, R. Electron Microscopy and Analysis, *Taylor and Francis*, London, **2001**.

[107] Burghardt, R. C.; Droleskey, R. Transmission Electron Microscopy, *Curr. Protoc.*

Microbiol, Unit 2B.1, **2006**.

[108] Wheeler, D. Precision Measurements of the Lattice Constants of Twelve Common Metals, *Phys. Rev.* **1925**, 25, 753.

[109] Jans, H.; Huo, Q. Gold Nanoparticle-Enabled Biological and Chemical Detection and Analysis, *Chem. Soc. Rev.* **2012**, 41, 2849.

[110] Atwater, H. A.; Polman, A. Plasmonics for Improved Photovoltaic Devices, *Nat. Mater.* **2010**, 9, 205.

[111] Ozbay, E. Plasmonics: Merging Photonics and Electronics at Nanoscale Dimensions, *Science* **2006**, 311, 189.

[112] Ma, Z.; Dai, S. Development of Novel Supported Gold Catalysts: A Materials Perspective, *Nano Res.* **2011**, 4, 3.

[113] Xia, Y.; Xiong, Y.; Lim, B.; Skrabalak, S. E. Shape Controlled Synthesis of Metal Nanocrystals: Simple Chemistry Meets Complex Physics?, *Angew. Chem. Int. Ed.* **2009**, 48, 60.

[114] Sastry, M.; Swami, A.; Mandal, S.; Selvakannan, P. R. New Approaches to the Synthesis of Anisotropic, Core–Shell and Hollow Metal Nanostructures, *J. Mater. Chem.* **2005**, 15, 3161.

[115] Skrabalak, S. E.; Au, L.; Li, X.; Xia, Y. Facile Synthesis of Ag Nanocubes and Au Nanocages, *Nat Protoc.* **2007**, 2, 2182.

[116] Sun, Y.; Xia, Y. Increased Sensitivity of Surface Plasmon Resonance of Gold Nanoshells Compared to that of Gold Solid Colloids in Response to Environmental Changes, *Anal. Chem*. **2002**, 74, 5297.

[117] Hu, M.; Chen, J.; Li, Z. Y.; Au, L.; Hartland, G. V.; Li, X.; Marquez, M.; Xia, Y.

Gold Nanostructures: Engineering their Plasmonic Properties for Biomedical Applications, *Chem. Soc. Rev.* **2006**, 35, 1084.

[118] Xia, Y.; Halas, N. J. Shape-Controlled Synthesis and Surface Plasmonic Properties of Metallic Nanostructures, *MRS Bull.* **2005**, 30, 338.

[119] Kim, S. W.; Kim, M.; Lee, W. Y.; Hyeon, T. Fabrication of Hollow Palladium Spheres and their Successful Application to the Recyclable Heterogeneous Catalyst for Suzuki Coupling Reactions, *J. Am. Chem. Soc*. **2002**, 124, 7642.

[120] Sabri, Y. M.; Ippolito, S. J.; Atanacio, A. J.; Bansal, V.; Bhargava, S. K. Mercury Vapor Sensor Enhancement by Nanostructured Gold Deposited on Nickel Surfaces using Galvanic Replacement Reactions, *J. Mater. Chem.* **2012**, 22, 21395.

[121] Bansal, V.; Jani, H.; Du Plessis, J.; Coloe, P. J.; Bhargava, S. K. Galvanic Replacement Reaction on Metal Films: A One-Step Approach to Create Nanoporous Surfaces for Catalysis, *Adv. Mater.* **2008**, 20, 717.

[122] Song, C.; Abell, J. L.; He, Y.; Murph, S. H.; Cui, Y.; Zhao, Y. Gold-Modified Silver Nanorod Arrays: Growth Dynamics and Improved SERS Properties, *J. Mater. Chem.* **2012**, 22, 1150.

[123] Najdovski, I.; O'Mullane, A. P.; Bhargava, S. K. Electrochemical Properties of Galvanically Replaced Iron Nanocubes with Gold and Palladium, *Electrochem. Commun*. **2010**, 12, 1535.

[124] Viyannalage, L. T.; Vasilic, R.; Dimitrov, N. Epitaxital Growth of Cu on Au(111) and Ag(111) by Surface Limited Redox Replacement—An Electrochemical and STM Study, *J. Phys. Chem. C* **2007**, 111, 4036.

[125] Gilroy, K. D.; Farzinpour, P.; Sundar, A.; T. Tan; Hughes, R. A.; Neretina, S. Substrate-based Galvanic Replacement Reactions Carried out on Heteroepitaxially formed Silver Templates, *Nano Research* **2013**, 6, 418.

[126] Draine, B. T.; Flatau, P. J. Discrete-dipole Approximation for Scattering Calculations, *J. Opt. Soc. Am. A* **1994**, 11, 1491.

[127] Mirin, N. A.; Ali, T. A.; Nordlander, P.; Halas, N. J. Perforated Semishells: Far-field Directional Control and Optical Frequency Magnetic Response, *ACS Nano* **2010**, 4, 2701.

[128] Gilroy, K. D.; Farzinpour, P.; Sundar, A.; Tan, T.; Hughes, R. A.; Neretina, S. Mechanistic Study of Substrate-based Galvanic Replacement Reactions, *Nano Research* **2014**, 7, 365.

[129] Sun, Y.; Mayers, B.; Xia, Y. Metal Nanostructures with Hollow Interiors, *Adv. Mater.* **2003**, 15, 641.

[130] Xia, X. H.; Wang, Y.; Ruditskiy, A.; Xia, Y. Galvanic Replacement: A Simple and Versatile Route to Hollow Nanostructures with Tunable and Well-Controlled Properties, *Adv. Mater.* **2013**, 25, 6313.

[131] Barth, S.; Boland, J. J.; Holmes, J. D. Defect Transfer from Nanoparticles to Nanowires, *Nano Lett.* **2011**, 11, 1550.

[132] Wang, J. G.; Tian, M. L.; Mallouk, T. E.; Chan, M. H. W. Microtwinning in Template-Synthesized Single-Crystal Metal Nanowires, *J. Phys. Chem. B* **2004**, 108, 841.

[133] Merz, M. D.; Dahlgren, S. D. Tensile Strength and Work Hardening of Ultrafine-Grained High-Purity Copper, *J. Appl. Phys.* **1975**, 46, 3235.

[134] Cheong, S.; Watt, J. D.; Tilley, R. D. Shape Control of Platinum and Palladium Nanoparticles for Catalysis, *Nanoscale* **2010**, 2, 2045.

[135] Chen, H. M.; Liu, R.-S.; Lo, M.-Y.; Chang, S.-C.; Tsai, L.-D.; Peng, Y.-M.; Lee, J.-F. Hollow Platinum Spheres with Nano-Channels: Synthesis and Enhanced Catalysis for Oxygen Reduction, *J. Phys. Chem. C* **2008**, 112, 7522.

[136] Pasricha, R.; Bala, T.; Biradar, A. V.; Umbarkar, S. Synthesis of Catalytically Active Platinum Nanoparticles by Transmetallation Reaction and Proposition of the Mechanism, *Small* **2009**, 5, 1467.

[137] Kim, M. R.; Lee, D. K.; Jang, D.-J. Facile Fabrication of Hollow Pt/Ag Nanocomposites having Enhanced Catalytic Properties, *Appl. Catal. B-Environ.* **2011**, 103, 253.

[138] Bansal, V.; O'Mullane, A. P.; Bhargava, S. K. Galvanic Replacement Mediated Synthesis of Hollow Pt Nanocatalysts: Significance of Residual Ag for the H_2 Evolution Reaction, *Electrochem. Commun.* **2009**, 11, 1639.

[139] Wu, R; Kong, Q.-C.; Fu, C.; Lai, S.-Q.; Ye, C.; Liu, J.-Y.; Chen, Y.; Hu, J.-Q. One-Pot Synthesis and Enhanced Catalytic Performance of Pd and Pt Nanocages via Galvanic Replacement Reactions, *RSC Adv.* **2013**, 3, 12577.

[140] Chen, J.; Wiley, B.; McLellan, J.; Xiong, Y.; Li Z.-Y.; Xia, Y. Optical Properties of Pd-Ag and Pt-Ag Nanoboxes Synthesized via Galvanic Replacement Reactions, *Nano Lett.* **2005**, 2058.

[141] Mahmoud, M. A.; El-Sayed, M. A. Metallic Double Shell Hollow Nanocages: The Challenges of their Synthetic Techniques, *Langmuir* **2012**, 28, 4051.

[142] Tan, Y.-N.; Yang, J.; Lee, J. Y.; Wang, D. I. C. Mechanistic Study on the Bis(*p*-

sulfonatophenyl)phenylphosphine Synthesis of Monometallic Pt Hollow Nanoboxes Using Ag*-Pt Core-Shell Nanocubes as Sacrificial Templates, *J. Phys. Chem. C* **2007**, 111, 14084.

[143] Zhang, H.; Jin, M.; Wang, J.; Li, W.; Camargo, P. H. C.; Kim, M. J.; Yang, D.; Xie, Z; Xia, Y. Synthesis of Pd-Pt Bimetallic Nanocrystals with a Concave Structure through a Bromide-Induced Galvanic Replacement Reaction, *J. Am. Chem. Soc.* **2011**, 133, 6078.

[144] Zhang, W.; Yang, J.; Lu, X. Tailoring Galvanic Replacement Reaction for the Preparation of Pt/Ag Bimetallic Hollow Nanostructures with Controlled Number of Voids, *ACS Nano* **2012**, 6, 7397.

[145] Lee, C.-L.; Tseng, C.-M. Ag-Pt Nanoplates: Galvanic Displacement Preparation and their Applications as Electrocatalysts, *J. Phys. Chem. C* **2008**, 112, 13342.

[146] Seo, D.; Song, H. Asymmetric Hollow Nanorod Formation through a Partial Galvanic Replacement Reaction, *J. Am. Chem. Soc.* **2009**, 131, 18210.

[147] Bi, Y.; Ye, J. Heteroepitaxial Growth of Platinum Nanocrystals on AgCl Nanotubes via Galvanic Replacement Reaction, *Chem. Commun.* **2010**, 46, 1532.

[148] Shen, Y.-L.; Chen, S.-Y.; Song, J.-M.; Chen, I.-G. Kinetic Study of Pt Nanocrystal Deposition on Ag Nanowires with Clean Surfaces via Galvanic Replacement, *Nanoscale Res. Lett.* **2012**, 7, 245.

[149] Hunyadi, S. E.; Murphy, C. J. Synthesis and Characterization of Silver–Platinum Bimetallic Nanowires and Platinum Nanotubes, *J Clust. Sci.* **2009**, 20, 319.

[150] Sławiński, G. W.; Zamborini, F. P. Synthesis and Alignment of Silver Nanorods and

Nanowires and the Formation of Pt, Pd, and Core/Shell Structures by Galvanic Exchange Directly on Surfaces, *Langmuir* **2007**, 23, 10357.

[151] Bi, Y.; Lu, G. Facile Synthesis of Platinum Nanofiber/Nanotube Junction Structures at Room Temperature, *Chem. Mater.* **2008**, 20, 1224.

[152] Du, C.; Chen, M.; Wang, W.; Tan, Q., Xiong, K.; Yin, G. Platinum-based Intermetallic Nanotubes with Core-Shell Structure as Highly Active and Durable Catalyst for Fuel Cell Applications, *J. Power Sources* **2013**, 240, 630.

[153] Liang, H.-P.; Zhang, H.-M.; Hu, J.-S.; Guo, Y.-G.; Wan, L.-J.; Bai, C.-L. Pt Hollow Nanospheres: Facile Synthesis and Enhanced Electrocatalysts, *Angew. Chem. Int. Ed*. **2004**, 43, 1540.

[154] Vasquez, Y.; Sra, A. K.; Schaak, R. E. One-Pot Synthesis of Hollow Superparamagnetic CoPt Nanospheres, *J. Am. Chem. Soc.* **2005**, 127, 12504.

[155] Pasricha, R.; Bala, T.; Biradar, A. V.; Umbarkar, S. Synthesis of Catalytically Active Platinum Nanoparticles by Transmetallation Reaction and Proposition of the Mechanism, *Small* **2009**, 5, 1467.

[156] Mohl, M.; Kumar, A.; Reddy, A. L. M.; Kukovecz, A.; Konya, Z.; Kiricsi, I.; Vajtai, R.; Ajayan, P. M. Synthesis of Catalytic Porous Metallic Nanorods by Galvanic Exchange Reaction, *J. Phys. Chem. C* **2010**, 114, 389.

[157] Li, Q.; Xu, P.; Zhang, B.; Wu, G.; Zhao, H.; Fu, E.; Wang, H.-L. Self-Supported Pt Nanoclusters via Galvanic Replacement from Cu_2O Nanocubes as Efficient Electrocatalysts, *Nanoscale* **2013**, 5, 7395.

[158] Park, D.-Y.; Jung, H. S.; Rheem, Y.; Hangarter, C. M.; Lee, Y.-I.; Ko, J. M.; Choa,

Y.-H.; Myung, N.V. Morphology Controlled 1D Pt Nanostructures Synthesized by Galvanic Displacement of Cu nanowires in Chloroplatinic Acid, *Electrochim. Acta* **2010**, 55, 4212.

[159] Liang, H.-W.; Liu, S.; Gong, J.-Y.; Wang, S.-B.; Wang, L.; Yu, S.-H. Ultrathin Te Nanowires: An Excellent Platform for Controlled Synthesis of Ultrathin Platinum and Palladium Nanowires/Nanotubes with Very High Aspect Ratio, *Adv. Mater.* **2009**, 21, 1850.

[160] Bi Y.; Ye, J. Heteroepitaxial Growth of Platinum Nanocrystals on AgCl Nanotubes via Galvanic Replacement Reaction, *Chem. Commun.* **2010**, 46, 1532.

[161] Zhang, W.; Yang, J.; Lu, X. Tailoring Galvanic Replacement Reaction for the Preparation of Pt/Ag Bimetallic Hollow Nanostructures with Controlled Number of Voids, *ACS Nano* **2012**, 6, 7397.

[162] Liu, L.; Yoo, S.-H.; Park, S. Synthesis of Vertically Aligned Hollow Platinum Nanotubes with Single Crystalline Nanoflakes, *Chem. Mater.* **2010**, 22, 2681.

[163] Li, D. G.; Wang, C.; Tripkovic D.; Sun, S. H.; Markovic, N. M.; Stamenkovic, V. R. Surfactant Removal for Colloidal Nanoparticles from Solution Synthesis: The Effect on Catalytic Performance, *ACS Catal.* **2012**, 2, 1358.

[164] Lee, H.; Habas, S. E.; Kweskin, S.; Butcher, D.; Somorjal, G. A.; Yang, P. D. Morphological Control of Catalytically Active Platinum Nanocrystals, *Angew. Chem., Int. Ed.* **2006**, 45, 7824.

[165] Gilroy, K. D.; Farzinpour, P.; Sundar, A.; Hughes, R. A.; Neretina, S. Sacrificial Templates for Galvanic Replacement Reactions: Design Criteria for the Synthesis of Pure Pt Nanoshells with a Smooth Surface Morphology, *Chem. Mater.* **2014**, 26,

3340.

[166] Wiley, B.; Sun, Y.; Chen, J.; Cang, H.; Li, Z.-Y.; Li, X.; Xia, Y. Shape-Controlled Synthesis of Silver and Gold Nanostructures, *MRS Bull.* **2005**, 30, 356.

[167] Carbone, L.; Cozzoli, P. D. Colloidal Heterostructured Nanocrystals: Synthesis and Growth Mechanisms, *Nano Today* **2010**, 5, 449.

[168] Lim, B.; Jiang, M.; Camargo, P. H. C.; Cho, E. C.; Tao, J.; Lu, X.; Zhu, Y.; Xia, Y. Pd-Pt Bimetallic Nanodendrites with High Activity for Oxygen Reduction, *Science* **2009**, 324, 1302.

[169] Kelly, K. L.; Coronado, E.; Zhao, L. L.; Schatz, G. C. The Optical Properties of Metal Nanoparticles: The Influence of Size, Shape, and Dielectric Environment, *J. Phys. Chem. B* **2003**, 107, 668.

[170] Huang, J.; Zhu, Y.; Lin, M.; Wang, Q.; Zhao, L.; Yang, Y.; Yao, K. X.; Han, Y. Site-Specific Growth of Au–Pd Alloy Horns on Au Nanorods: A Platform for Highly Sensitive Monitoring of Catalytic Reactions by Surface Enhancement Raman Spectroscopy, *J. Am. Chem. Soc.* **2013**, 135, 8552.

[171] Hao, R.; Xing, R.; Xu, Z.; Hou, Y.; Gao, S.; Sun, S. Synthesis, Functionalization, and Biomedical Applications of Multifunctional Magnetic Nanoparticles, *Adv. Mater.* **2010**, 22, 2729.

[172] Griffith Freeman, R.; Hommer, M. B.; Grabar, K. C.; Jackson, M. A.; Natan, M. J. Ag-Clad Au Nanoparticles: Novel Aggregation, Optical, and Surface-Enhanced Raman Scattering Properties, *J. Phys. Chem*. **1996**, 100, 718.

[173] Rivas, L.; Sanchez-Cortes, S.; Garcia-Ramos, J. V.; Morcillo, G. Mixed Silver/Gold Colloids: A Study of Their Formation, Morphology, and Surface-Enhanced Raman Activity, *Langmuir* **2000**, 16, 9722.

[174] Cao, Y. W.; Jin, R.; Mirkin, C. A. DNA-Modified Core-Shell Ag/Au Nanoparticles, *J. Am. Chem. Soc.* **2001**, 123, 7961.

[175] Sanedrin, R. G.; Georganopoulou, D. G.; Park, S.; Mirkin, C. A. Seed-Mediated Growth of Bimetallic Prisms, *Adv. Mater.* **2005**, 17, 1027.

[176] Habas, S. E.; Lee, H.; Radmilovic, V.; Somorjai, G. A.; Yang, P. Shaping Binary Metal Nanocrystals Through Epitaxial Seeded Growth, *Nat. Mater.* **2007**, 6, 692.

[177] Fan, F. R.; Liu, D. Y.; Wu, Y. F.; Duan, S.; Xie, Z. X.; Jiang, Z. Y.; Tian, Z. Q. Epitaxial Growth of Heterogeneous Metal Nanocrystals: From Gold Nano-Octahedra to Palladium and Silver Nanocubes, *J. Am. Chem. Soc.* **2008**, 130, 6949.

[178] Yang, Y.; Zhang, Q.; Fu, Z. W.; Qin, D. Transformation of Ag Nanocubes into Ag-Au hollow Nanostructures with Enriched Ag Contents to Improve SERS Activity and Chemical Stability, *ACS Appl. Mater. Interfaces* **2014**, 6, 3750.

[179] Yang, Y.; Liu, J.; Fu, Z. W.; Qin, D. Galvanic Replacement-Free Deposition of Au on Ag for Core–Shell Nanocubes with Enhanced Chemical Stability and SERS Activity, *J. Am. Chem. Soc*. **2014**, 136, 8153.

[180] Lee, H.; Habas, S. E.; Somorjai, G. A.; Yang, P. Localized Pd Overgrowth on Cubic Pt Nanocrystals for Enhanced Electrocatalytic Oxidation of Formic Acid, *J. Am. Chem. Soc.* **2008**, 130, 5406.

[181] Yang, Y.; Wang, W.; Li, X.; Chen, W.; Fan, N.; Zou, C.; Chen, X.; Xu, X.; Zhang, L.; Huang, S. Controlled Growth of Ag/Au Bimetallic Nanorods through Kinetics Control, *Chem. Mater*. **2013**, 25, 34.

[182] Zhu, C.; Zeng, J.; Tao, J.; Johnson, M.; Schmidt-Krey, I.; Blubaugh, L.; Zhu, Y.; Gu, Z.; Xia, Y. Kinetically Controlled Overgrowth of Ag or Au on Pd Nanocrystal Seeds:

From Hybrid Dimers to Nonconcentric and Concentric Bimetallic Nanocrystals, *J. Am. Chem. Soc.* **2012**, 134, 15822.

[183] Xie, S.; Peng, H.-C.; Lu, N.; Wang, J.; Kim, M. J.; Xie, Z.; Xia, Y. Confining the Nucleation and Overgrowth of Rh to the {111} Facets of Pd Nanocrystal Seeds: The Roles of Capping Agent and Surface Diffusion, *J. Am. Chem. Soc.* **2013**, 135, 16658.

[184] Gilroy, K. D.; Hughes, R. A.; Neretina, S. Kinetically Controlled Nucleation of Silver on Surfactant-Free Gold Seeds, *J. Am. Chem. Soc.* **2014,** 136, 15337.

[185] Herrero, E.; Buller, L. J.; Abruña, H. D. Underpotential Deposition at Single Crystal Surfaces of Au, Pt, Ag and Other Materials, *Chem. Rev.* **2001**, 101, 1897.

[186] Schmickler, W.; Santos, E. Interfacial Electrochemistry, 2nd ed.; Springer: Berlin, **2010**.

[187] Baffou G.; Quidant, R. Nanoplasmonics for Chemistry, *Chem. Soc. Rev.* **2014**, 43, 3898.

[188] Xiao, M.; Jiang, R.; Wang, F.; Fang, C.; Wang, J.; Yu, J. C. Plasmon-Enhanced Chemical Reactions, *J. Mater. Chem. A* **2013**, 1, 5790.

[189] Clavero, C. Plasmon-Induced Hot-Electron Generation at Nanoparticle/Metal-Oxide Interfaces for Photovoltaic and Photocatalytic Devices, *Nat. Photonics* **2014**, 8, 95.

[190] Wadell, C.; Syreova, S.; Langhammer, C. Plasmonic Hydrogen Sensing with Nanostructured Metal Hydrides, *ACS Nano* **2014**, 8, 11925.

[191] Shuford, K. L.; Ratner, M. A.; Schatz, G. C. Multipolar Excitation In Triangular Nanoprisms, *J. Chem. Phys.* **2005**, 123, 114713.

[192] Kim, S.; Jin, J.; Kim, Y.-J.; Park, I.-Y.; Kim, Y.; Kim, S.-W. High-Harmonic Generation by Resonant Plasmon Field Enhancement, *Nature* **2008**, 453, 757.

[193] Shahjamali, M. M.; Bosman, M.; Cao, S.; Huang, X.; Cao, X.; Zhang, H.; Pramana, S. S.; Xue, C. Surfactant-Free Sub-2 nm Ultrathin Triangular Gold Nanoframes, *Small* **2013**, 9, 2880.

[194] Jin, R.; Cao, Y.; Mirkin, C. A.; Kelly, K. L.; Schatz, G. C.; Zheng, J. G. Photoinduced Conversion of Silver Nanospheres to Nanoprisms, *Science* **2001**, 294, 1901.

[195] Scarabelli, L.; Coronado-Puchau, M.; Giner-Casares, J. J.; Langer, J.; Liz-Marzan, L. M. Monodisperse Gold Nanotriangles: Size Control, Large-Scale Self-Assembly, and Performance in Surface-Enhanced Raman Scattering, *ACS Nano* **2014**, 8, 5833.

[196] Xue, C.; Li, Z.; Mirkin, C. A. Large-Scale Assembly of Single-Crystal Silver Nanoprism Monolayers, *Small* **2005**, 1, 513.

[197] Gopinath, A.; Boriskina, S. V.; Reinhard, B. M.; Negro, L. D. Deterministic Aperiodic Arrays of Metal Nanoparticles for Surface-Enhanced Raman Scattering (SERS), *Opt. Express* **2009**, 17, 3741.

[198] Viarbitskaya, S.; Teulle, A.; Marty, R.; Sharma, J.; Girard, C.; Arbouet, A.; Dujardin, E. Tailoring and Imaging the Plasmonic Local Density of States in Crystalline Nanoprisms, *Nat. Mater*. **2013**, 12, 426.

[199] Zhou, Y.; Zhou, X.; Park, D. J.; Torabi, K.; Brown, K. A.; Jones, M. R.; Zhang, C.; Schatz, G. C.; Mirkin, C. A. Shape-Selective Deposition and Assembly of Anisotropic Nanoparticles, *Nano Lett.* **2014**, 14, 2157.

[200] Li, D.; Wang, C.; Tripkovic, D.; Sun, S; Markovic, N. M.; Stamenkovic, V. R., Surfactant Removal for Colloidal Nanoparticles from Solution Synthesis: The Effect on Catalytic Performance, *ACS Catal.* **2012**, 2, 1358.

[201] Niu, Z.; Li, Y. Removal and Utilization of Capping Agents in Nanocatalysis, *Chem. Mater.* **2014**, 26, 72.

[202] Marshall, M. S. J.; Castell, M. R. Scanning Tunnelling Microscopy of Epitaxial Nanostructures, *Chem. Soc. Rev.* **2014**, 43, 2226.

[203] Henry, C. R. Morphology of Supported Nanostructures, *Prog. Surf. Sci.* **2005**, 3-4, 92.

[204] Sundar, A.; Farzinpour, P.; Gilroy, K. D.; Teng T.; Hughes, R. A.; Neretina, S. Eutectic Combinations as a Pathway to the Formation of Substrate-Based Au-Ge Heterodimers and Hollowed Au Nanocrescents with Tunable Optical Properties, *Small* **2014**, 10, 3379.

[205] Sundar, A.; Farzinpour, P.; Gilroy, K. D.; Tan, T.; Hughes, R. A.; Neretina, S, Organized Surfaces of Highly Faceted Single-crystal Palladium Structures Seeded by Sacrificial Templates, *Cryst. Growth Des.* **2013**, 13, 3847.

[206] Gilroy, K. D.; Sundar, A.; Hajfathalian, M, A.; Yaghoubzade, A.; Tan, T.; Sil, D.; Borguet, E.; Hughes, R. A.; Neretina, S. Transformation of Truncated Gold Octahedrons into Triangular Nanoprisms through the Heterogeneous Nucleation of Silver, *Nanoscale* **2015**, 7, 6827.

[207] Bialas, H.; Heneka, K. Epitaxy of fcc Metals on Dielectric Substrates, *Vacuum* **1994**, 45, 79.

[208] Liu, N.; Tang, M. L.; Hentschel, M.; Giessen, H.; Alivisatos, A. P. Nanoantenna-Enhanced Gas Sensing in a Single Tailored Nanofocus, *Nature Mater.* **2011**, 10, 631.

[209] Syrenova, S.; Wadell, C.; Langhammer, C. Shrinking-Hole Colloidal Lithography: Self Aligned Nanofabrication of Complex Plasmonic Nanoantennas, *Nano Lett*. **2014**, 14, 2655.

[210] Wadell C.; Syrenova S.; Langhammer C. Plasmonic Hydrogen Sensing with Nanostructured Metal Hydrides, *ACS Nano* **2014**, 8, 11925.

[211] Luo, Y. R. Comprehensive Handbook of Chemical Bond Energies, CRC Press, Boca Raton, Florida, **2007**, 9.

[212] Baletto, F.; Mottet, C.; Ferrando, R.; Baletto, F.; Mottet, C.; Ferrando, R. Molecular Dynamics Simulations of Surface Diffusion and Growth on Silver and Gold Clusters, *Surf. Sci.* **2000**, 446, 31.

[213] Plante, M. C.; Lapierre, R. R.; Growth Mechanisms of GaAs Nanowires by Gas Source Molecular Beam Epitaxy, *J. Cryst. Growth* **2006**, 286, 394.

[214] de Miguel, J. J.; Miranda, R. Atomic Aspects in the Epitaxial Growth of Metallic Superlattices and Nanostructures, *J. Phys. Condens. Matter.* **2002**, 14, R1063.

[215] Liu, S. J.; Huang, H.; Woo, C. H. Schwoebel-Ehrlich Barrier: From Two to Three Dimensions, *Appl. Phys. Lett.* **2002**, 80, 3295.

[216] Du, Y.; Chen, H.; Chen, R.; Xu, N. Synthesis of p-Aminophenol from p-Nitrophenol over Nano-Sized Nickel Catalysts, *Appl. Catal., A* **2004**, 277, 259.

[217] Corbett, J. F. An Historical Review of the use of Dye Precursors in the Formulation of Commercial Oxidation Hair Dyes, *Dyes Pigm*. **1999**, 41, 127.

[218] Rode, C. V.; Vaidya, M. J.; Chaudhari, R. V. Synthesis of p-Aminophenol by Catalytic Hydrogenation of Nitrobenzene, *Org. Process Res. Dev.* **1999**, 3, 465.

[219] Hervés, P., Pérez-Lorenzo, M., Liz-Marzán, L. M., Dzubiella, J., Lu, Y., Ballauff, M. Catalysis by Metallic Nanoparticles in Aqueous Solution: Model Reactions, *Chem. Soc. Rev.* **2012**, 41, 5577.

[220] Lee, I.; Delbecq, F.; Morales, R.; Albiter, M. A.; Zaera, F. Tuning Selectivity in Catalysis by Controlling Particle Shape, *Nat. Mater.* **2009**, 8, 132.

[221] Zhao, P.; Fenga, X.; Huanga, D.; Yanga, G.; Astruc, D. Basic Concepts and Recent Advances In Nitrophenol Reduction By Gold- and Other Transition Metal Nanoparticles, *Coord. Chem. Rev.* **2015**, 287, 114.

[222] Zheng, G.; Polavarapu, L.; Liz-Marzán, L. M.; Pastoriza-Santos I.; Pérez-Juste, J. Gold Nanoparticle-Loaded Filter Paper: A Recyclable Dip-Catalyst For Real-Time Monitoring By Surface Enhanced Raman Scattering, *Chem. Commun.* **2015**, 51, 4572.

[223] Zheng, G.; Kaefer, K.; Mourdikoudis, S.; Polavarapu, L.; Vaz, B.; Cartmell, S. E.; Bouleghlimat, A.; Buurma, N.; Yate, L.; de Lera, A. R.; Liz-Marzán, L. M.; Pastoriza I.; Pérez-Juste, J. Palladium Nanoparticle-Loaded Cellulose Paper: A Highly Efficient,

Robust, and Recyclable Self-Assembled Composite Catalytic System, *J. Phys. Chem. Lett*. **2015**, 6, 230.

[224] Nishikata, T.; Tsutsumi, H.; Gao, L.; Kojima, K.; Chikama K.; Nagashima, H. Adhesive Catalyst Immobilization Of Palladium Nanoparticles On Cotton And Filter Paper: Application To Reusable Catalysts For Sequential Catalytic Reactions, *Adv. Synth. Catal*. **2014**, 356, 951.

[225] Hariprasad E.; Radhakrishnan, T. P. A Highly Efficient and Extensively Reusable "Dip Catalyst" Based On A Silver-Nanoparticle-Embedded Polymer Thin Film, *Chem. Eur. J*. **2010**, 16, 14378.

[226] He, R.; Wang, Y. C.; Wang, X.; Wang, Z.; Liu, G.; Zhou, W.; Wen, L.; Li, Q.; Wang, X.; Chen, X.; Zeng, J.; Hou, J. G. Facile Synthesis Of Pentacle Gold–Copper Alloy Nanocrystals And Their Plasmonic And Catalytic Properties, *Nat. Commun.* **2014**, 5, 1.

[227] Hajfathalian, M; Gilroy, K. D.; Yaghoubzade, A.; Sundar, A.; Teng, T.; Hughes, R. A. Neretina, S. Photocatalytic Enhancements to the Reduction of 4-Nitrophenol by Resonantly Excited Triangular Gold-Copper Nanoprisms, **2015**, ***Submitted***.

[228] Pozun, Z. D.; Rodenbusch, S. E.; Keller, E.; Tran, K.; Tang, W.; Stevenson, K. J.; Henkelman, G. A Systematic Investigation of p-Nitrophenol Reduction by Bimetallic Dendrimer Encapsulated Nanoparticles, *J. Phys. Chem. C* **2013**, 117, 7598.

[229] Nørskov, J. K.; Bligaard, T.; Hvolbæk, B.; Abild-Pedersen, F.; Chorkendorff, I.; Christensen, C. H. The Nature Of The Active Site In Heterogeneous Metal Catalysis, *Chem. Soc. Rev.*, **2008**, 37, 2163.

[230] Shahjamali, M. M.; Bosman, M, Cao, S.; Huang X.; Cao, X.; Zhang, H.; Pramana, S. S.; Xue C. Surfactant-free sub-2 nm Ultrathin Triangular Gold Nanoframes, *Small* **2013**, 9, 2880.